TECHNISCHE UNIVERSITEIT DELFT

MASTER THESIS

Calibration of a Single element ultrasound transducer using an aberration mask

submitted in partial fulfilment of the requirements for the degree of
MASTER OF SCIENCE
in
ELECTRICAL ENGINEERING
by
Bram Bryan Visser (4332830)

Company supervisor	*Daily supervisor*	*University supervisor*
Pieter Kruizinga	**Pim van der Meulen**	**Geert Leus**
Assistant professor	PhD student	Professor

August 16, 2019

Abstract

Previous work [1] has demonstrated the possibility of high resolution imaging through the use of a single element and a aberration mask. This thesis will expand on the previous work by examining the proposed method for errors in the creation of the model. The analysis is preformed by examining the various aspects of the measurements setup and underlying theoretical model, after which measurements are performed to determine their contribution and correctness with regard to the model. Results demonstrated a systematic error of a non-linear frequency scaling and semi-linear phase shift. The origin of the error lies in the unwanted addition of transfer functions of some of the components. A Tikhonov regularized least squares method is proposed to estimate this transfer function and supply compensation based on all the measurements. The results of application of this method on the uncalibrated model are demonstrated through 1D imaging experiments. The result of which show a significant improvement over the previous uncalibrated results. After which the possibility of calibration due to a singular measurement is explored and a adaptation of the Tikhonov regularized least squares method is proposed for close approximation of the previously found transfer function. Further to obtain an indication of possible remaining hurdles and successes with this method, extensive simulations are preformed to examine the individual impact of various sources of noise and interference.

"Our deepest fear is not that we are inadequate. Our deepest fear is that we are powerful beyond measure. It is our light, not our darkness, that most frightens us. Your playing small does not serve the world. There is nothing enlightened about shrinking so that other people won't feel insecure around you. We are all meant to shine as children do. It's not just in some of us; it is in everyone. And as we let our own lights shine, we unconsciously give other people permission to do the same. As we are liberated from our own fear, our presence automatically liberates others."

-Marianne Williamson

Acknowledgements

It is with heavy hand and a joyous hart that I write this chapter for it marks the end of a 5 year long journey of which the last 9 months were spend creating this thesis. This long and arduous journey would not have ended in success if not for a few remarkable people that I would like to thanks here.

- First my two closes friends, Desmond van Gale and Stephanie van Leeuwen. You where the rock on which I leaned in the darkest hours and you refused to let me fall. I might never be able to repay either of you but know that I am gonna try my hardest.
- Secondly, my family, who raised me to be the man I am today and supported me on this journey in anyway they could. Their endless patience, advice and support have made this journey a reality. Know that every step I take from now on is thanks to you.
- Thirdly, all the people who have joined me in this 5 year journey, my business associates, my study friends, drinking mates, fightclub friends, fenching mates and everyone else that I have met along the way. Know that it would not have been such a wondrous journey without you.

In special I want to thank a few people have have specifically helped me with creating this thesis.

- First, Pim van der Meulen. Your patience is the stuff of legends, teaching my stubborn self cannot have been easy but you never gave up and have taught me so much.
- Secondly, Geert Leus. You saw the potential in me even when I could not see it myself.
- And finally, Pieter Kruizinga for pushing me to improve in every aspect of being a engineer.

Contents

List of Figures

List of Tables

1 Introduction

To supply the best possible care to any patient a physician needs as much information about the patient and its condition as possible. This need combined with the need for affordable treatment and the technological advancements of recent decades has generated a large push into the field of medical electronics.

With Ischaemic heart diseases and strokes being the two leading causes of death in the world [2] it is natural that a large amount of research focuses on the heart and veins. One such area of research pertains to the imaging inside the veins, offering a look within the patient instead of from the outside. Given the small amount of space available and the close proximity to the tissue only ultrasound is currently a viable imaging modality for achieving inter atrial imaging.

Ultrasound consists of acoustic waves which propagate through motion of particles and deformation of volumes above 20 kHz up to several gigahertz. The precise mathematical derivation of how deformation of a volume and the motion of particles lead to acoustic waves can be read at the beginning of chapter 2. These wave travel through the medium until they hit the boundary of another medium where part of the wave continues travelling and the remainder bounces back. How much bounces back and how much travels and in which direction is depend on the angle of arrival of the wave and the acoustic impedance of the material. The acoustic impedance is defined as:

$$Z = \rho c \tag{1}$$

Where ρ is the medium density and c is the speed of sound of the material. The amount reflected and transmitted is given by:

$$R = \frac{Z_2 cos(\theta_i) - Z_1 cos(\theta_t)}{Z_2 cos(\theta_i) + Z_1 cos(\theta_t)} \tag{2}$$

$$T = \frac{2Z_2 cos(\theta_i)}{Z_2 cos(\theta_i) + Z_1 cos(\theta_t)} \tag{3}$$

Where $Z1$ and Z_2 denote the acoustic impedance of material 1 and 2 where the wave starts in material 2, θ_i and θ_t are the angle at which the wave arrives and at which it continues its path in the new material respectively. There reflections are the basis of ultrasound imaging. By measuring the time between transmission of a wave and when we receive the reflection, combined with the speed of sound of the medium, allows us to compute the distance it travelled before it hit the object. The usage of reflections or more commonly named echo's to measure the distance to a object or the presence of a object is called echo imaging.

Echo imaging allows for accurate measurement of the distance to a object but not the location of a object. This is due to the spherical nature of wave, if 2 points are placed equidistant from the source they will reflect back at the same time and therefore its not possible to determine which one of the 2 points reflected back the signal. A visual representation of this is given below:

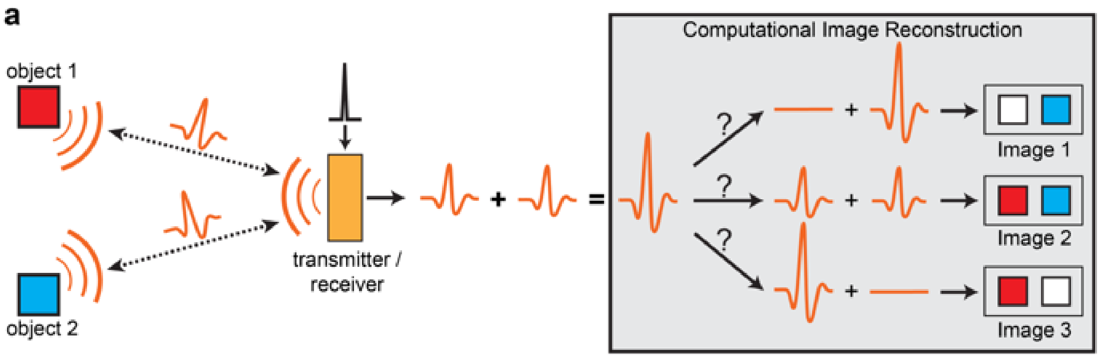

Figure 1: Visualization of the reflection of 2 points[1]

A common way to solve this problem is by beam forming, beam forming consists of sending a signal from multiple elements are different times to generate a wave in a certain direction. A visual representation of this process is shown below:

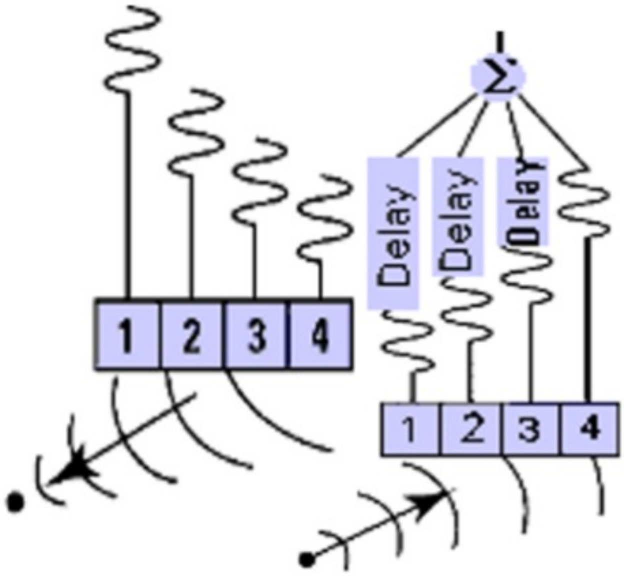

Figure 2: Visualization of beam forming[3]

Currently this method of imaging is used inside of the arteries by placing a array of miniature ultrasound elements at the tip and then forming the beam to highlight certain areas inside the arteries to obtain a image with higher spatial resolution then without. The major downside and limiting factor in the usage of multiple elements to improve the spatial resolution is the fact that every element needs its own wire to transmit the information, cleanly and without generating to much heat in the catheter itself. Given the limited space inside a human artery this imposes a natural limit to the amount of elements that can be placed at the tip of a catheter. Therefore, alternatives are researched that are capable of obtaining high resolution images inside the arteries without the prescribed downsides. On such alternative is was proposed in [1] [4] where good results are obtained in the case of strong reflective phantoms.

1.1 Single element imaging with an aberration mask

The method proposed in [1] was to use an aberration mask to purposefully scatter the wave from a single element to improve spatial resolution. A schematically overview of this idea is shown below:

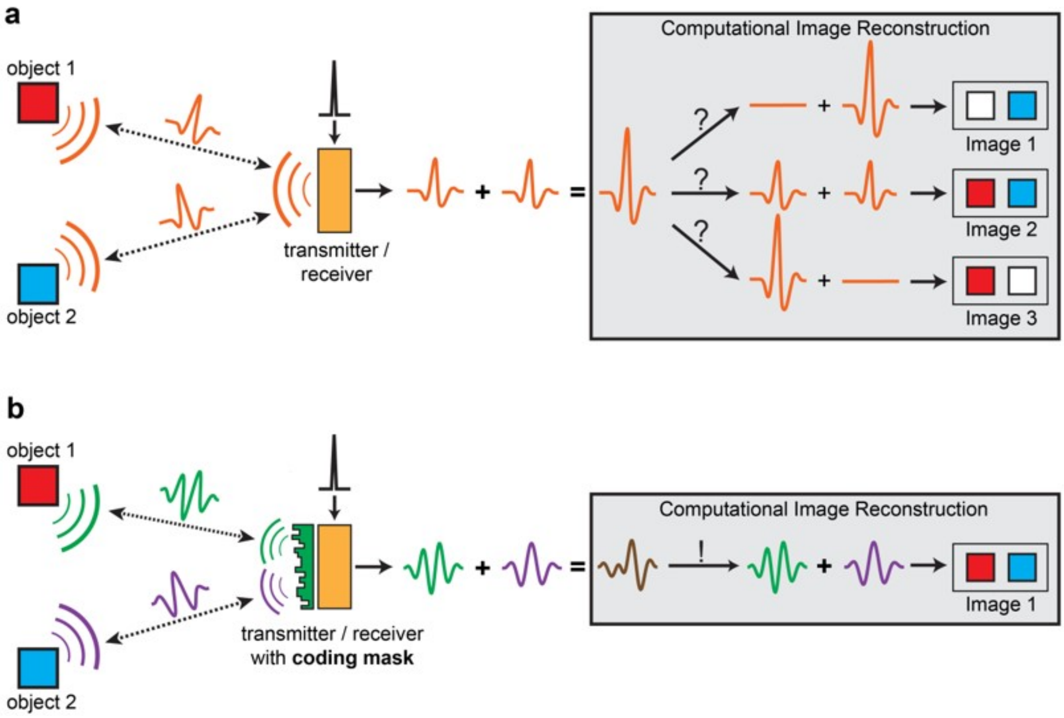

Figure 3: Original idea for improving single element imaging [1]

As shown the idea behind this approach is that by purposely distorting the transmitted signal the reflection from each point in the imaging domain will be unique. This method requires of course to know the reflected wave from each point in space to which the received signal can be compared to determine where it came from. Mathematically this can be described as :

$$\mathbf{y} = \mathbf{A}\mathbf{x} \tag{4}$$

Where **y** contains the received signal, **A** contains all the known reflected waves from each point in space and **x** represents the image itself. A more complete understanding and derivation of this model an be found in chapter 2.
The mask used in [4] was not able to achieve the unique reflection of each point in each domain but was able to reconstruct strong reflective phantoms with success as shown below:

Figure 4: Measurement setup for letter imaging[1]

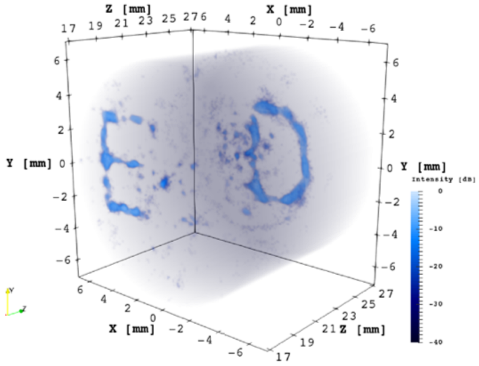

Figure 5: Resulting reconstruction of letters[1]

This method has not been successfully applied to the imaging of biological tissue due to the fact that tissue is a weak reflector compared to the phantoms in [4] and therefore more susceptible to noise, interference and errors. The focus of this thesis will be on examining, analysing and if needed improving upon the proposed method of [4] to enable the use of it for biological tissue. The starting focus will be on the method of obtaining the model **A** of the image domain and how it might differ from the theoretical model on which the method was build.

To that end, the thesis will be organized as follows: In chapter 2 we will give a derivation of the signal model used in [4] and a schematic view of the measurement setup used to obtain the model **A**. In chapter 3 we will introduce a measurement setup to examine the difference that exists, offer a calibration method to compensate for this difference and demonstrate it's effectiveness with point on a line imaging experiments. In chapter 4 the compensation vector is further examined through visualisation and by attempting to construct it using only a single measurement. In chapter 5 an overview of other possible noise and interference sources will be presented, examined through the use of simulations and ultimately used to obtain a expected image based on the current state of single ultrasound imaging to demonstrate its possible viability.

2 Signal model of the imaging modality

This section will derive a theoretical model for the imaging problem that will link the measured signal to the information of interest. Given the high complexity of this model a practical measurement based approach to obtaining the model parameters will be presented to result in the final signal model that will serve as the starting point for this thesis.

2.1 Theoretical Derivation of the Signal model

Starting from the Physical equations that govern Ultrasound a derivation to the Helmholtz's equation for waves is made. From there on the general inverse scattering field problem is obtained which, after discretization, will be the basis of our model.

2.1.1 Physics of Ultrasound

The field of Ultrasound concerns itself with acoustic waves which consist of longitudinal waves that propagate through compression and decompression [5]. This behaviour is described by the deformation equation using Hooke's law ((5)) and the equation of motion using Newton's law ((6)).

$$q(\vec{r},t) - \kappa \frac{\partial p(\vec{r},t)}{\partial t} = \nabla v(\vec{r},t) \tag{5}$$

$$f(\vec{r},t) - \rho \frac{\partial v(\vec{r},t)}{\partial t} = \nabla p(\vec{r},t) \tag{6}$$

Where $f(\vec{r},t)$ is the volume density of volume force, $q(\vec{r},t)$ is the volume density of injection rate , $v(\vec{r},t)$ is the particle velocity, $p(\vec{r},t)$ is the pressure and $\vec{r}$ is the vector representing the spatial dimensions x, y and z. For the remainder of this derivation the dependency of time and space will be omitted for readability.

$$\begin{aligned} &\begin{cases} q - \kappa \frac{\partial p}{\partial t} = \nabla v \\ f - \rho \frac{\partial v}{\partial t} = \nabla p \end{cases} \rightarrow \begin{cases} \frac{\partial q}{\partial t} - \kappa \frac{\partial}{\partial t}(\frac{\partial p}{\partial t}) = \frac{\partial}{\partial t}(\nabla v) \\ \nabla f - \rho \nabla(\frac{\partial v}{\partial t}) = \nabla(\nabla p) \end{cases} \rightarrow \begin{cases} \frac{\partial q}{\partial t} - \kappa \frac{\partial^2 p}{\partial^2 t} = \frac{\partial}{\partial t} \nabla v \\ \nabla(\frac{\partial v}{\partial t}) = \frac{1}{\rho}[\nabla f - \nabla^2 p] \end{cases} \\ &\rightarrow \begin{cases} \frac{\partial}{\partial t} \nabla v = \frac{\partial q}{\partial t} - \kappa \frac{\partial^2 p}{\partial^2 t} \\ \frac{\partial}{\partial t} \nabla v = \frac{1}{\rho}[\nabla f - \nabla^2 p] \end{cases} \rightarrow \frac{\partial q}{\partial t} - \kappa \frac{\partial^2 p}{\partial^2 t} = \frac{1}{\rho}[\nabla f - \nabla^2 p] \end{aligned} \tag{7}$$

Taking the final equation from (7) and swapping the terms around to obtain:

$$\rho \frac{\partial q}{\partial t} - \nabla f = \rho \kappa \frac{\partial^2 p}{\partial^2 t} - \nabla^2 p \tag{8}$$

Using the fact that $c = \frac{1}{\sqrt{\rho \kappa}}$ and moving all the terms that are not related to pressure to the right results in the Helmholtz equation:

$$\nabla^2 p - \frac{1}{c^2} \frac{\partial^2 p}{\partial^2 t} = \nabla f - \rho \frac{\partial q}{\partial t} \tag{9}$$

Generalising this equation to the general wave equation by renaming $p = u$ and identifying that $\nabla - \rho \frac{\partial q}{\partial t}$ are external sources and replace them with $-q$ the following formulation is obtain:

$$\nabla^2 u - \frac{1}{c^2} \frac{\partial^2 u}{\partial^2 t} = -q \tag{10}$$

Performing the temporal Fourier transform on the formulation of (10) results in the Helmholtz equation:

$$\nabla^2 \hat{u} + \hat{\gamma}^2 \hat{u} = -\hat{q} \tag{11}$$

Where $\hat{\gamma} = \frac{j\omega}{c}$ and c is the speed of sound that is material and therefore, location dependant.

2.1.2 Inverse Scattering Problem

The imaging problem consist of finding the material properties within the image domain from the transmitted and received signal. This is called an inverse scattering problem and the proper formulation of this problem can be obtained by exploiting the linearity of the wave and equation (11). The linearity of the wave is given by:

$$\hat{u} = \hat{u}^{inc} + \hat{u}^{sc} \tag{12}$$

Making $\hat{u}$ a linear combination of the incident and scattered field. The next step is defining that inside the image domain the total field is 0 and outside the image domain its equal to the external sources.

$$\nabla^2\hat{u} + \hat{\gamma}^2\hat{u} = 0 \quad \vec{r} \in \mathbb{D}^{obj} \tag{13}$$

$$\nabla^2\hat{u} + \hat{\gamma}_b^2\hat{u} = -\hat{q} \quad \vec{r} \notin \mathbb{D}^{obj} \tag{14}$$

The subscript b in $\hat{\gamma}_b^2$ is used to indicate that the velocity c that is in γ is equal to the velocity of the background medium that is taken to be homogeneous outside the image domain. The same definition can be applied to the incident field:

$$\nabla^2\hat{u}^{inc} + \hat{\gamma}_b^2\hat{u}^{inc} = 0 \quad \vec{r} \in \mathbb{D}^{obj} \tag{15}$$

$$\nabla^2\hat{u}^{inc} + \hat{\gamma}_b^2\hat{u}^{inc} = -\hat{q} \quad \vec{r} \notin \mathbb{D}^{obj} \tag{16}$$

Now to obtain a equation for the scatter field start with rewriting (13) as follows:

$$\begin{gathered}\nabla^2\hat{u} + \hat{\gamma}^2\hat{u} = 0 \rightarrow \nabla^2\hat{u} = -\widehat{\gamma^2}\hat{u} \rightarrow \\ \nabla^2\hat{u} + \widehat{\gamma_b^2}\hat{u} = -\widehat{\gamma^2}\hat{u} + \widehat{\gamma_b^2}\hat{u} \rightarrow \\ \nabla^2\hat{u} + \gamma_b^2\hat{u} = (\widehat{\gamma_b^2} - \widehat{\gamma^2})\hat{u} \quad \vec{r} \in \mathbb{D}^{obj}\end{gathered} \tag{17}$$

Now subtract (15) from (17) to obtain:

$$\nabla^2\hat{u}^{sc} + \gamma_b^2\hat{u}^{sc} = (\widehat{\gamma_b^2} - \widehat{\gamma^2})\hat{u} \quad \vec{r} \in \mathbb{D}^{obj} \tag{18}$$

Now also subtract (16) from (14) to obtain:

$$\nabla^2\hat{u}^{sc} + \hat{\gamma}_b^2\hat{u}^{sc} = 0 \quad \vec{r} \notin \mathbb{D}^{obj} \tag{19}$$

Which eliminates the outside sources and enabling the combination of (18) and (19) to:

$$\nabla^2\hat{u}^{sc} + \hat{\gamma}_b^2\hat{u}^{sc} = \hat{q}^{sc} \tag{20}$$

Where $\hat{q}^{sc}$ is defined as:

$$\hat{q}^{sc}(\vec{r},\omega) = \begin{cases}(\widehat{\gamma_b^2} - \widehat{\gamma^2})\hat{u} & \vec{r} \in \mathbb{D}^{obj} \\ 0 & \vec{r} \notin \mathbb{D}^{obj}\end{cases} \tag{21}$$

Which can be rewritten as :

$$\hat{q}^{sc}(\vec{r},\omega) = \begin{cases}\widehat{\gamma_b^2}\chi(\vec{r})\hat{u} & \vec{r} \in \mathbb{D}^{obj} \\ 0 & \vec{r} \notin \mathbb{D}^{obj}\end{cases} \tag{22}$$

Where $\chi(\vec{r})$ is called the contrast source and given by:

$$\chi(\vec{r}) = \begin{cases}1 - \frac{\widehat{\gamma^2}}{\hat{\gamma}_b^2} \\ 0\end{cases} = \begin{cases}1 - [\frac{c_b}{c(\vec{r})}]^2 & \vec{r} \in \mathbb{D}^{obj} \\ 0 & \vec{r} \notin \mathbb{D}^{obj}\end{cases} \tag{23}$$

To remove the ∇ operator in (20) the spatial Fourier transform is applied. Utilising the following definitions $\nabla \xrightarrow{\mathcal{F}} -j\vec{k}$ [6] and $\vec{k} \cdot \vec{k} = k^2$ generates the following:

$$k^2\tilde{u}^{sc} + \tilde{\gamma}_b^2\tilde{u}^{sc} = \tilde{q}^{sc} \rightarrow \tilde{u}^{sc} = \frac{1}{k^2 + \tilde{\gamma}_b^2}\tilde{q}^{sc} \tag{24}$$

Before returning to the temporal frequency domain a new variable is introduced for readabilities sake.

$$\frac{1}{k^2 + \tilde{\gamma}_b^2} = \tilde{G} \tag{25}$$

Transforming Eq. (24) into:

$$\tilde{u}^{sc}(K_r,\omega) = \tilde{G}\tilde{q}^{sc} \tag{26}$$

Denoting $\hat{G}$ as the temporal frequency counterpart to $\tilde{G}$ and taking in to account that a product in the spatial frequency domain results in a convolution in space:

$$\hat{u}^{sc}(\vec{r},\omega) = \int_{\vec{r'} \in \mathbb{D}^{obj}} \hat{G}(\vec{r} - \vec{r'},\omega)\hat{q}^{sc}(\vec{r'},\omega)dV \tag{27}$$

This representation gives an expression for the scattered field in the temporal frequency domain but cannot be solved due to the fact that $\hat{q}^{sc}$ which contains the contrast source $\hat{\chi}$ and source $\tilde{u}$ is unknown and that the image domain $\mathbb{D}^{obj}$ is also unknown. Starting with the latter problem, we can identify a inversion region that encompasses the entire object domain.

$$\hat{u}^{sc}(\vec{r},\omega) = \hat{\gamma}_b^2 \int_{\vec{r'}\in\mathbb{D}^{inv}} \hat{G}(\vec{r}-\vec{r'},\omega)\chi(\vec{r'})\hat{u}(\vec{r'},\omega)dV \quad \vec{r}\in\mathbb{R}^3 \tag{28}$$

Then we have to fix observation vector $\vec{r}$ to some point or location. The logical choice is the observation domain where our receivers are resulting in:

$$\hat{u}^{sc}(\vec{r},\omega) = \hat{\gamma}_b^2 \int_{\vec{r'}\in\mathbb{D}^{inv}} \hat{G}(\vec{r}-\vec{r'},\omega)\chi(\vec{r'})\hat{u}(\vec{r'},\omega)dV \quad \vec{r}\in\mathbb{D}^{rec} \tag{29}$$

This equation is known as the data equation in integral form and connects the contrast source χ with the receiver domain.

2.1.3 Born approximation

The data equation derived in the previous section cannot be solved due to the fact that the total field in the inversion domain is not known. However given the weak reflections within biological tissue it is assumed that the born approximation can be applied. The born approximation states that we can replace the total field with the incident field if the scattered field is negligible compared to the incident field. Transforming equation (29) in to:

$$\hat{u}^{sc}(\vec{r},\omega) = \hat{\gamma}_b^2 \int_{\vec{r'}\in\mathbb{D}^{inv}} \hat{G}(\vec{r}-\vec{r'},\omega)\chi(\vec{r'})u^{\hat{inc}}(\vec{r'},\omega)dV \quad \vec{r}\in\mathbb{D}^{rec} \tag{30}$$

Where the incident field can be derived using equations (15) and (16) and is left to the curious reader. Resulting in a function that relates the scattered field to the contrast function $\chi(\vec{r})$. Discretizing this function in space allows us to describe it as Riemann sum of the following form:

$$\hat{u}^{sc}(\vec{r},\omega) = \hat{\gamma}_b^2 \sum_{i=1}^{N} \hat{G}(\vec{r}-\vec{r'_i},\omega)\chi(\vec{r'_i})u^{\hat{inc}}(\vec{r'_i},\omega)\Delta\vec{r'_i} \tag{31}$$

Where $\Delta\vec{r'_i}$ is the size of a voxel and N is the number of voxels. Further discretizing the frequency spectrum and recognise the following points: $\Delta\vec{r'_i}$ is a constant value for all iterations of i, the receiver domain contains only 1 element and following that observation that the amount of voxels in $\hat{G}$ are the same as in $u^{\hat{inc}}$ we can write the entire Riemann sum as the following matrix vector product:

$$\begin{bmatrix} \hat{u}^{sc}(\omega_1) \\ \vdots \\ \hat{u}^{sc}(\omega_M) \end{bmatrix} = \hat{\gamma}_b^2 \Delta r \begin{bmatrix} G(\vec{r}-\vec{r'_1},\omega_1) & \dots & G(\vec{r}-\vec{r'_N},\omega_1) \\ \vdots & \ddots & \vdots \\ G(\vec{r}-\vec{r'_1},\omega_M) & \dots & G(\vec{r}-\vec{r'_N},\omega_M) \end{bmatrix} \odot \begin{bmatrix} u^{\hat{inc}}(r_1,\omega_1) & \dots & u^{\hat{inc}}(r_N,\omega_1) \\ \vdots & \ddots & \vdots \\ u^{\hat{inc}}(r_1,\omega_M) & \dots & u^{\hat{inc}}(r_N,\omega_M) \end{bmatrix} \begin{bmatrix} \chi_1 \\ \vdots \\ \chi_N \end{bmatrix} \tag{32}$$

Where $\odot$ is the hadamard or pointwise product and N is the amount of voxels from the spatial discretization and M is the amount of frequency bins from the frequency discretization. Taking the following terms together:

$$\mathbf{A} = \hat{\gamma}_b^2 \Delta r \begin{bmatrix} G(\vec{r}-\vec{r'_1},\omega_1) & \dots & G(\vec{r}-\vec{r'_N},\omega_1) \\ \vdots & \ddots & \vdots \\ G(\vec{r}-\vec{r'_1},\omega_M) & \dots & G(\vec{r}-\vec{r'_N},\omega_M) \end{bmatrix} \odot \begin{bmatrix} u^{\hat{inc}}(r_1,\omega_1) & \dots & u^{\hat{inc}}(r_N,\omega_1) \\ \vdots & \ddots & \vdots \\ u^{\hat{inc}}(r_1,\omega_M) & \dots & u^{\hat{inc}}(r_N,\omega_M) \end{bmatrix}$$
$$\mathbf{y} = \begin{bmatrix} \hat{u}^{sc}(\omega_1) \\ \vdots \\ \hat{u}^{sc}(\omega_M) \end{bmatrix} \quad \mathbf{x} = \begin{bmatrix} \chi_1 \\ \vdots \\ \chi_N \end{bmatrix} \tag{33}$$

gives us our final model:

$$\mathbf{y} = \mathbf{A}\mathbf{x} + \mathbf{n} \tag{34}$$

Where $\mathbf{n}$ is a Mx1 vector that represents the ever present noise in a practical measurement. It is assumed to be zero mean, white complex Gaussian noise with unknown variance.

2.2 The practical signal model

The matrix **A** in the derived model contains the discretized convolution of the Green's function times the incident field which can be seen as the transfer function of the element to each pixel. Computing this model **A** would be complicated, time consuming and only be a approximation of reality due to the nature of the solution. Therefore, it was decided to measure the transfer function of each point in the domain to obtain a model that is as complete as possible.

2.2.1 Obtaining the signal model

Measuring each point within the signal space comes with its own set of challenges therefor certain theorems, assumptions and generalisations where used. Below a complete list of the assumptions, theorems and generalisation is given together with the impact the application has.

- First, just as in the derived model the space will be divided into voxels to create a finite and manageable set of measurement points. A voxel is a 3 dimensional space where the vertices are significantly smaller then the wavelength. In this voxel it is assumed that the field is the same for each possible point that exist in this space. Therefore allowing for N measurements only, where N is the amount of voxels.
- Second, the Nyquist sampling theorem is used to limit the required sample frequency in our measurement setup from infinitely high to only 2 times the highest frequency of interest.
- Third, due to the linear nature of ultrasound we use reciprocity (see Appendix A) to only measure the forward field and then use auto-convolution to obtain the full transfer function. Reciprocity states that we can interchange source and receiver and that the transfer function between the two is unchanged. Therefore, we can logically extrapolate that the transfer function given by the forward field is the same as that of the reflected field and therefore we are allowed to use the auto-convolution to obtain the full field.
- Fourth, to speed up the measurement process only the forward field of each point in a plain is measured at the distance that enables good SNR. Then, using the Angular Spectrum Approach (ASA) this 2D plane can be propagated along the depth axis to obtain slices of the forward field at different depths which, after auto-convolving these slices, allow for the creation of a complete 3D model.
- The final generalisation is the usage of a water bath in which these measurements where done instead of inside the human arteries. The speed of sound in water is between 1450 to 1500 m/s and in blood/human tissue this is in the range of 1540 to 1560. This relative small difference is is negligible and has shown to be of little importance over the years of existing medical ultrasound.

To summarise, the measurements performed to obtain the signal model **A** are the forward field of a set of voxels in a 2D plane that are then auto-convolved to obtain the columns of the model **A**. Mathematically speaking the model **A** is constructed as follows:

$$a_k(t) = f_{xy}(t) * f_{xy}(t) \tag{35}$$

Where $f_{xy}(t)$ is the measured forward field at the (x, y) coordinate in the 2D plane and $a_k(t)$ is the $k$the column of the model matrix **A** which is associated with the pixel (x, y). Visualising this matrix results in:

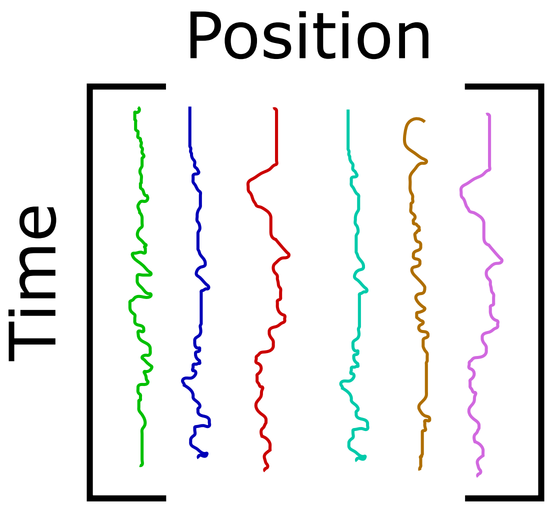

Figure 6: Visual representation of **A**

For the full 3D model, the 2D plane is propagated along the depth through the use of ASA to obtain slices at different depths which extends equation (36) as follows:

$$a_k(t) = f_{xyz}(t) * f_{xyz}(t) \tag{36}$$

Where the number of columns k is now extended to accommodate the increase in the umber of pixels.

2.2.2 The measurement setup

The measurement of the forward field $f_{xy}(t)$ was performed with a measurement setup of which a schematic overview is given below:

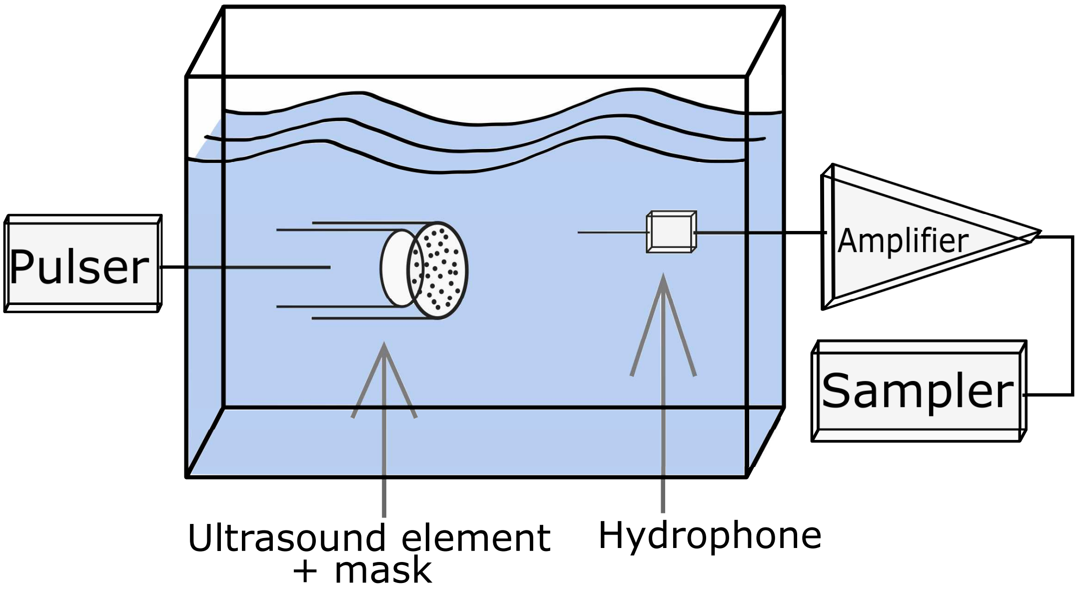

Figure 7: Hydrophone measurement setup

The components used in this setup are the following:

- For the Pulser the PANAMETRICS 5077PR square-wave pulser/receiver was used and set to deliver 100V pulses at 10MHz. The reason for a 10MHz pulse was to ensure that the signal was narrow enough for the transmitted pulse to be regarded as a dirac pulse by the system.
- The element is a unfocused 5MHz ultrasound transducer.
- The mask is made of PCMA and the holes are drilled at random locations.
- The hydrophone is a 0.2mm hydrophone from precision acoustics ltd.

- The amplifier is a matching amplifier designed for the the hydrophone consisting of the PA12044 pre amplifer and the DCPS286 DC Coupler.
- The sampler is the 12-bit Acqiris DP310 digitizer with 4096 discretization levels providing resolution of voltage differences larger than 1.2 mV (in case of 5 V vertical range).

Going forward in this Thesis, the measurement of the forward field after auto convolution will be referred to as Pulse-echo estimate.

3 Calibration

The introduced measurement setup in chapter 2.2.2 to construct the model **A** introduces components that affect the measurement that are not taken into account when deriving the measurement methodology. Their possible effects are potentially magnified due to the auto-convolution of the received signal. In this Chapter it will be examined if the components combined have an impact on the model **A** and how the model can be calibrated to compensate for these effects.

3.1 The measurement setup components

As stated in the introduction of this chapter, the used setup from chapter 2.2.2 contains some extra components that are not included in the signal model.It is assumed that each component is a Linear Time Invariant(LTI) system with it's own transfer function. These transfer functions are listed below:

- $S(t)$ the time signal that is transmitted
- $T_x(t)$ the transfer function of the transmit element
- $M_x^{ask1}y(t)$ the transfer function of the mask on the forward field
- $M_x^{edium1}y(t)$ the transfer function of the medium on the forward field
- $H_{xy}^{ydro}(t)$ the transfer function of the hydrophone
- $A_1^{mp}(t)$ the transfer function of the amplifier

Using the LTI assumption, the total transfer function can be obtained by convolving, with respect to time, the individual transfer functions resulting in the following expression for the forward field:

$$f_{xy}(t) = S * T^x * M_{xy}^{ask1} * M_{xy}^{edium1} * H_{xy}^{ydro} * A_1^{mp} \tag{37}$$

Now to arrive at a function for each column in **A** we make use of equation (36) resulting in:

$$a_{xy}(t) = S * T^x * M_{xy}^{ask1} * M_{xy}^{edium1} * H_{xy}^{ydro} * A_1^{mp} * S * T^x * M_{xy}^{ask1} * M_{xy}^{edium1} * H_{xy}^{ydro} * A_1^{mp} \tag{38}$$

It is clear that there are more components in the final columns of **A** then modelled in the theoretical derivation of the columns. Furthermore, in an actual imaging experiment there are also more components that make up the received signal then theoretically devised. To examine if there exists a error due to the addition of these components in either scenario a second measurement setup was devised.

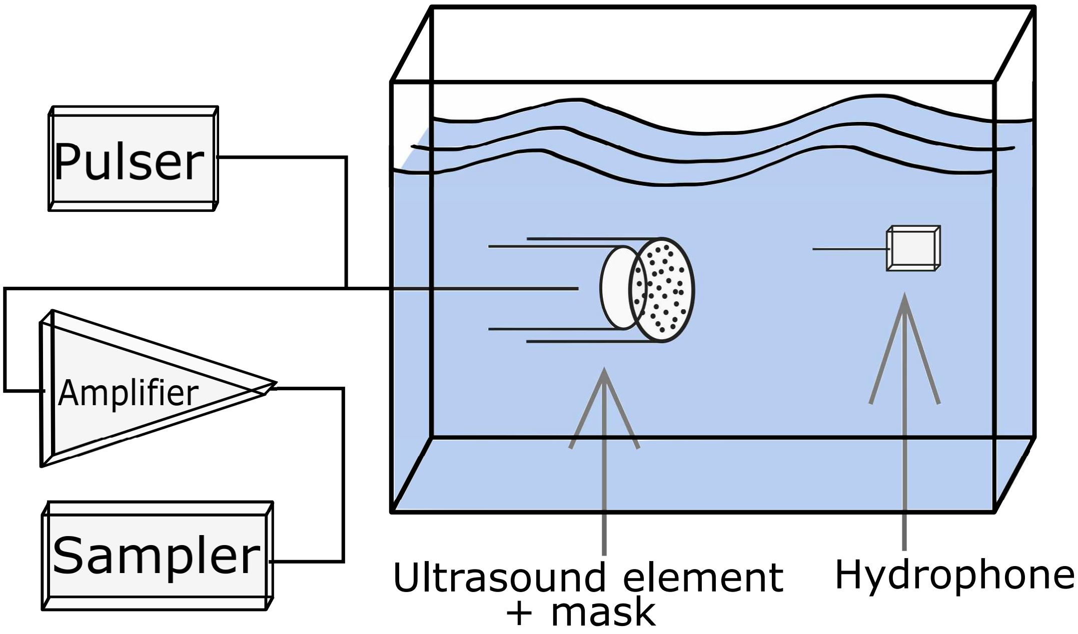

Figure 8: Expected point scatter measurement setup

This second setup performs measurements as would be done when imaging a object. In this case the object is the needle of the hydrophone and the received echo's are assumed to be the correct signals that should make up the columns of **A**. Therefore these measurements are used as a ground truth to compare the pulse-echo estimate measurements against. These measurements will be named Pulse echo measurements or Pulse for the remainder of the thesis.

Just as in the case of hydrophone measurement setup, we can determine the transfer function of the separate components that make up this pulse echo measurement setup and arrive at a function for the measured signal. The identified transfer functions of the components are:

- $S(t)$ the time signal that is transmitted
- $T^x(t)$ the transfer function of the transmit element
- $M_x^{ask1}y(t)$ the transfer function of the mask on the forward field
- $M_x^{edium1}y(t)$ the transfer function of the medium on the forward field
- $R_x^{eflect}y(t)$ the transfer function of reflecting of the contrast
- $M_x^{edium2}y(t)$ the transfer function of the medium on the reflected field
- $M_x^{ask2}y(t)$ the transfer function of the mask on the reflected field
- $R^x(t)$ the transfer function of the receiver element
- $A_2^{mp}(t)$ the transfer function of the amplifier

It should be noted that a different amplifier was used in both setups so that $A_1^{mp} \neq A_2^{mp}$. The associated transfer function of this setup is given by:

$$a_{ij}(t) = S * T^x * M_x^{ask1}y * M_x^{edium1}y * R_{xy}^{eflect} * M_x^{edium2}y * M_x^{ask2}y * R^x * A_2^{mp} \tag{39}$$

Comparing equation (37) and equation (39) and removing the shared components results in:

$$H_{ij}^{ydro} * A_1^{mp} * S * T_x * M_x^{ask1}y * M_x^{edium1}y * H_{ij}^{ydro} * A_1^{mp} = R_{ij}^{eflect} * M_x^{edium2}y * M_x^{ask2}y * R_x * A_2^{mp} \tag{40}$$

Therefore posing the question: are these equal in which case the difference between the measurements and the assumed signal model are not due to these components or is calibration of the model **A** required?

3.2 Comparison measurements

To answer the question posed in the last section a measurement plan was drawn up, executed and the results were analysed to determine if the pulse-echo estimate measurements are equal to the true pulse-echo measurements.

3.2.1 Measurement grid

Before being able to show the measurement plan, a common grid system has to be established to reference the various positions and points that are discussed in this thesis. The grid is defined as follows:

- The location (0,0,0) is located at the center of the transducer on the pressure wave emitting side.
- The positive z direction is away from the transducer
- The positive x direction is on the left side when looking along the positive z direction or on the right hand side when facing the transducer
- The positive y direction is upwards and the negative direction is downwards.

3.2.2 Measurement plan

To obtain an thorough understanding of the possible impact of mismatch between equation (38) and equation (39) the following set of measurements (1,2,3) with permutations (a,b,c,d,e) where preformed:

1. Dense horizontal measurements ranging from 5mm from the left of the center to 5 mm to the right of the center at 2,5mm depth.
   (a) The horizontal line was measured 2 mm above the center
   (b) The horizontal line was measured 1 mm above the center
   (c) The horizontal line was measured at the center
   (d) The horizontal line was measured 1 mm below the center
   (e) The horizontal line was measured 2 mm below the center
2. Dense Vertical measurements ranging from 5mm above the center to 5mm below the center at 2,5mm depth.
   (a) The vertical line was measured 2 mm to the left of the center
   (b) The vertical line was measured 1 mm to the left of the center
   (c) The vertical line was measured at the center
   (d) The vertical line was measured 1 mm to the right of the center
   (e) The vertical line was measured 1 mm to the right of the center
3. Dense depth measurements starting at 2.5mm and moving towards the center and stopping at 0.5mm depth
   (a) The depth line was measured 1 mm to the left of the center
   (b) The depth line was measured 1 mm to the right of the center
   (c) The depth line was measured at the center
   (d) The depth line was measured 1 mm above the center
   (e) The depth line was measured 1 mm below the center

Each combination (for instance, 2.e) constitutes 1 experiment where 101 measurement points are measured with a sampling rate of 20MHz and a frequency resolution of 5KHz.

3.2.3 Measurement results

For brevity's sake, the results shown here are relevant representations of some of the measurements listed in the measurement plan. It can be safely assumed that the results for the other cases are similar.

Before being able to compare the measured time signals in the measurement plan, a few processing steps have to be made. First up is the subtraction of the mean of the signal to center the signal around 0.

$$y(t) = x(t) - \mu_x \tag{41}$$

Where x is the measured signal, μ_x is the mean of the measured signal and y is the resulting signal. This removes the DC component which is assumed to have no consequence on the results or their interpretation given that the frequency on which the transducer operates is orders of magnitude higher. Resulting in:

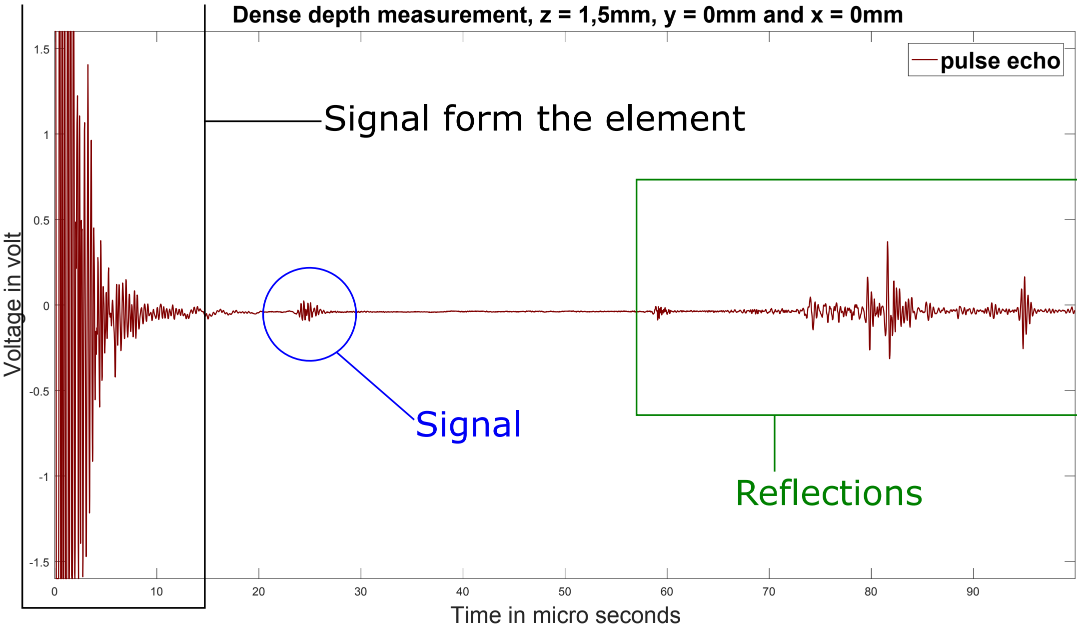

Figure 9: Unprocessed pulse-echo measurement

From the result it is clear that we have a few sources of noise to deal with. Namely the signal that is send is immediately recorded by the ultrasound element plus some noise and the extra reflections of the back and side wall of the tank. This is resolved by isolating the signal by placing a tapered cosine window across the signal.

$$y(t) = (x(t) - \mu_x)w(t) \tag{42}$$

Where w is the tapered cosine function that is placed across the signal at the right time. It should be noted that this is not sufficient in all the measurement scenarios. In the depth measurement scenarios the hydrophone comes so close that the Signal from the element and the reflection from the hydrophone are measured at the same moment. Given the fact that this signal is of the same frequency and due to the fact that the signal can never be perfectly know due to the noise, it cannot be removed. Resulting in depth measurements close to the element to deviate strongly from the remaining measurements. And finally, after mean subtraction and windowing, the remaining signal was normalised by dividing it by the absolute maximum value of that measurement.

$$y(t) = \frac{(x(t) - \mu_x)w(t)}{max(|(x(t) - \mu_x)w(t)|)} \tag{43}$$

The results of the measurement after this processing are shown below:

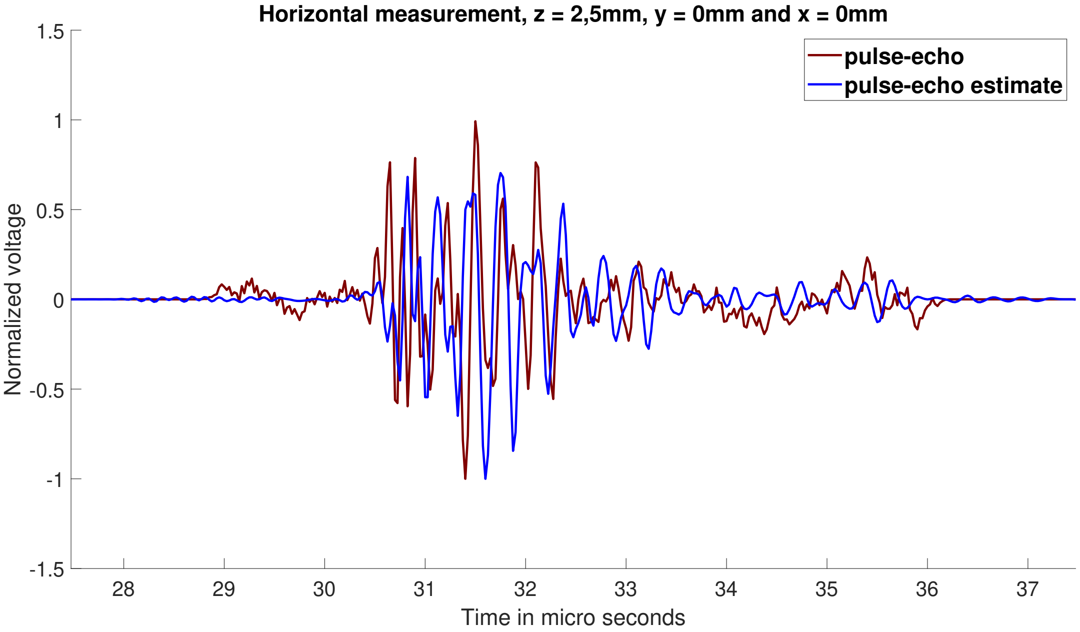

(a)

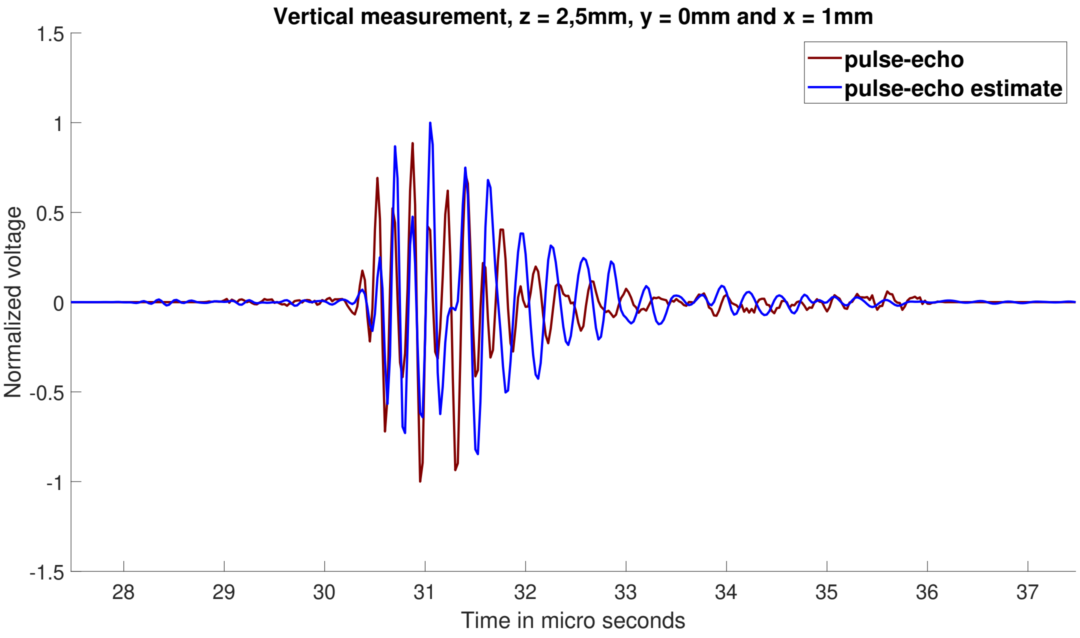

(b)

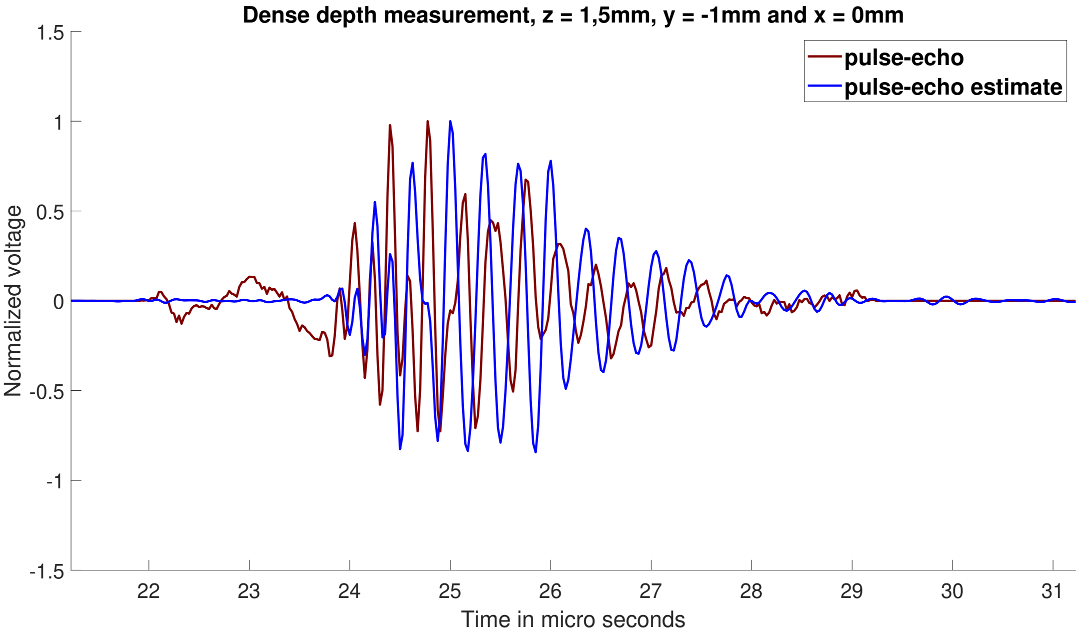

(c)

Figure 10: Measurement results for horizontal (a), vertical (b) and Depth (c) measurements

The measurement results clearly show that there is a marked difference between the assumed signal from the model **A** and the real pulse echo signal.

3.3 Analysis

From the time domain image shown in the previous section it could be concluded that the pulse-echo estimate measurements are inverted and time shifted compared to the pulse-echo measurement. To examine the validity of that conclusion the time signal was inverted.

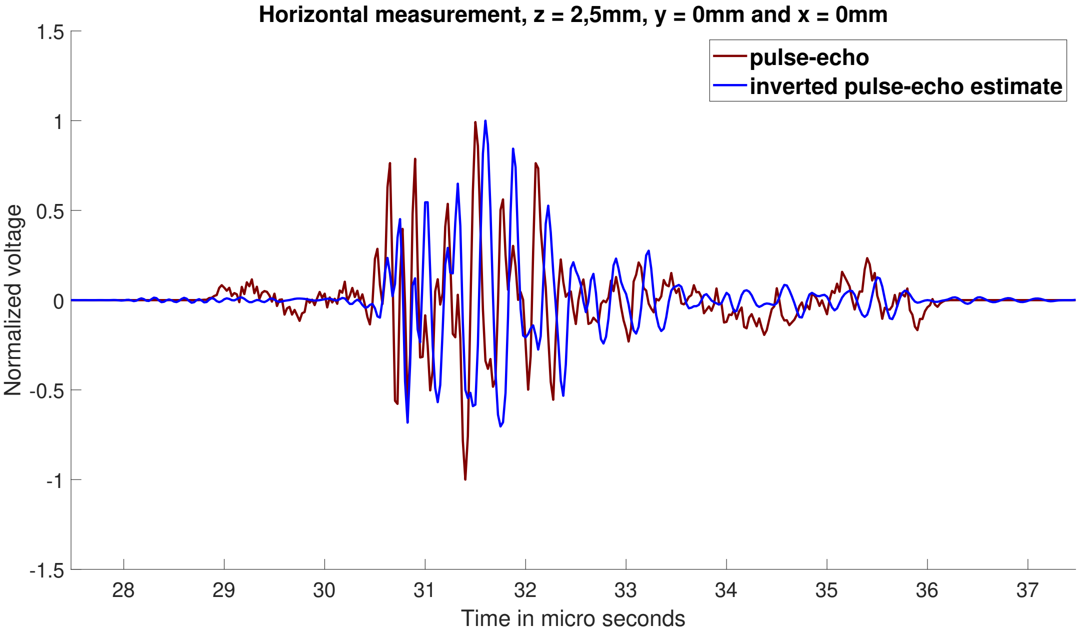
Horizontal measurement, z = 2,5mm, y = 0mm and x = 0mm
pulse-echo
inverted pulse-echo estimate
Normalized voltage
1.5
1
0.5
0
-0.5
-1
-1.5
28
29
30
31
32
33
34
35
36
37
Time in micro seconds

(a)

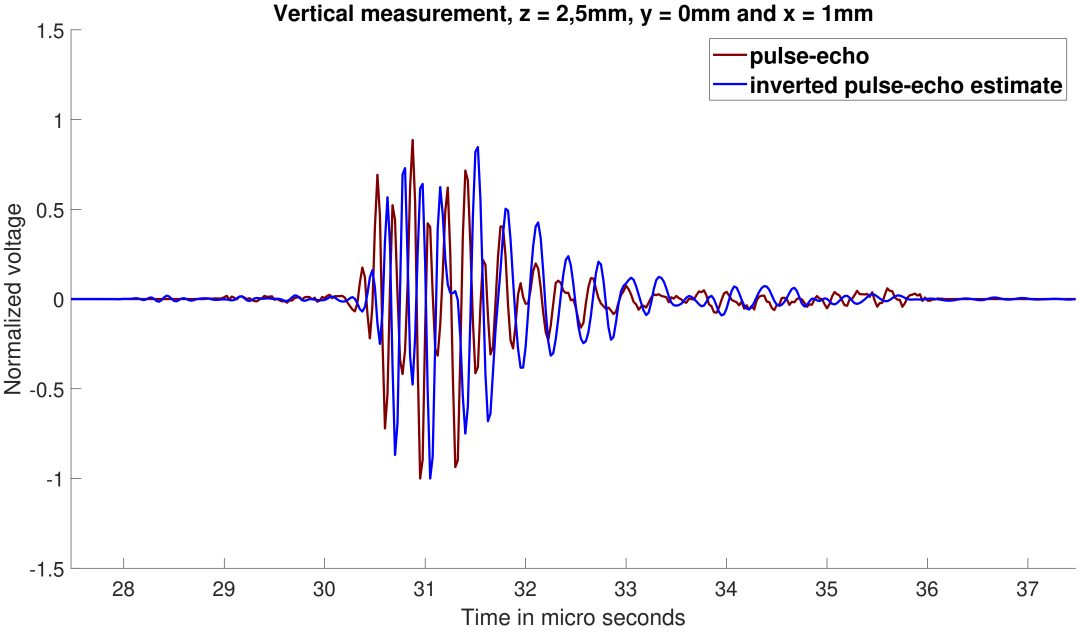
Vertical measurement, z = 2,5mm, y = 0mm and x = 1mm
pulse-echo
inverted pulse-echo estimate
Normalized voltage
1.5
1
0.5
0
-0.5
-1
-1.5
28
29
30
31
32
33
34
35
36
37
Time in micro seconds

(b)

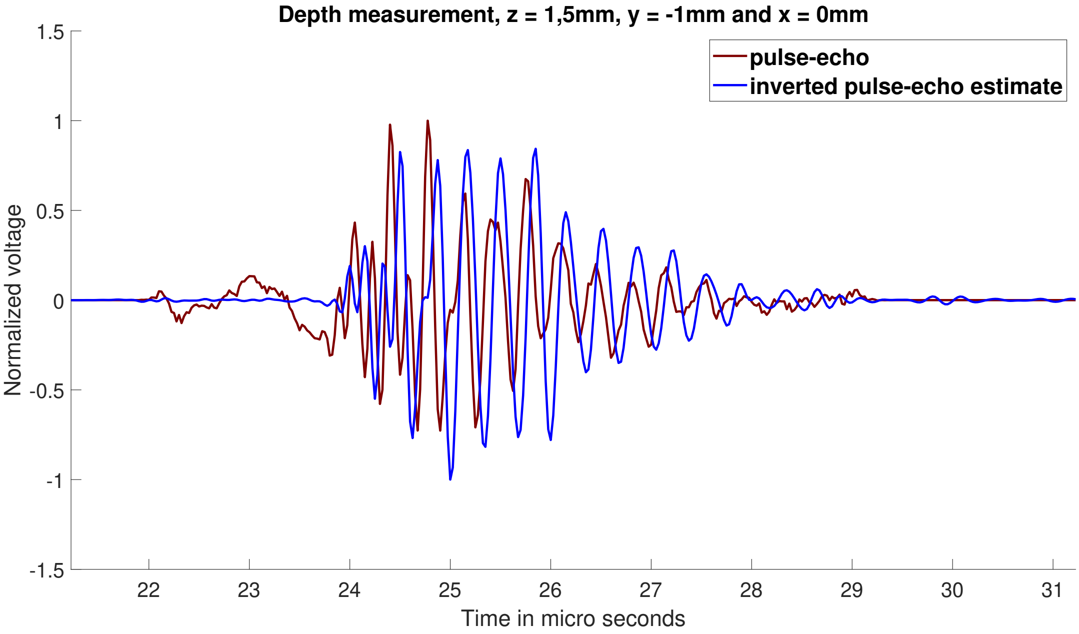

(c)

Figure 11: Measurement results for horizontal (a), vertical (b) and Depth (c) measurements after inversion of pulse-echo estimate measurements

And then to determine the time shift the auto correlation was computed and the maximum value was taken to determine the optimal time shift. The result of that computation is shown in the table below:

	Horizontal	Vertical	Depth
Mode	100ns	100ns	100ns
Mean	97,8ns	173.9ns	97,4ns
Median	100ns	100ns	100ns

Table 1: Table of highest correlated time shift across the measurements

It is clear from this table that the delay is a consistent one across all measurements. Therefore, it seems to be a systemic error instead of an incidental one which means that this time shift can be applied to all signals. The result of applying this time shift on the data is show below:

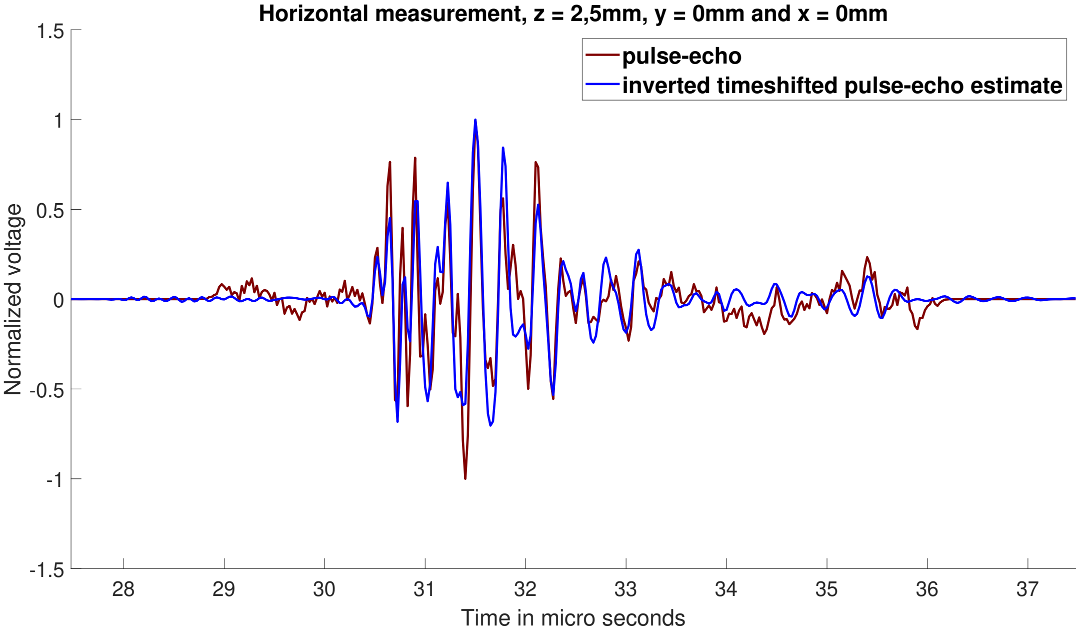

(a)

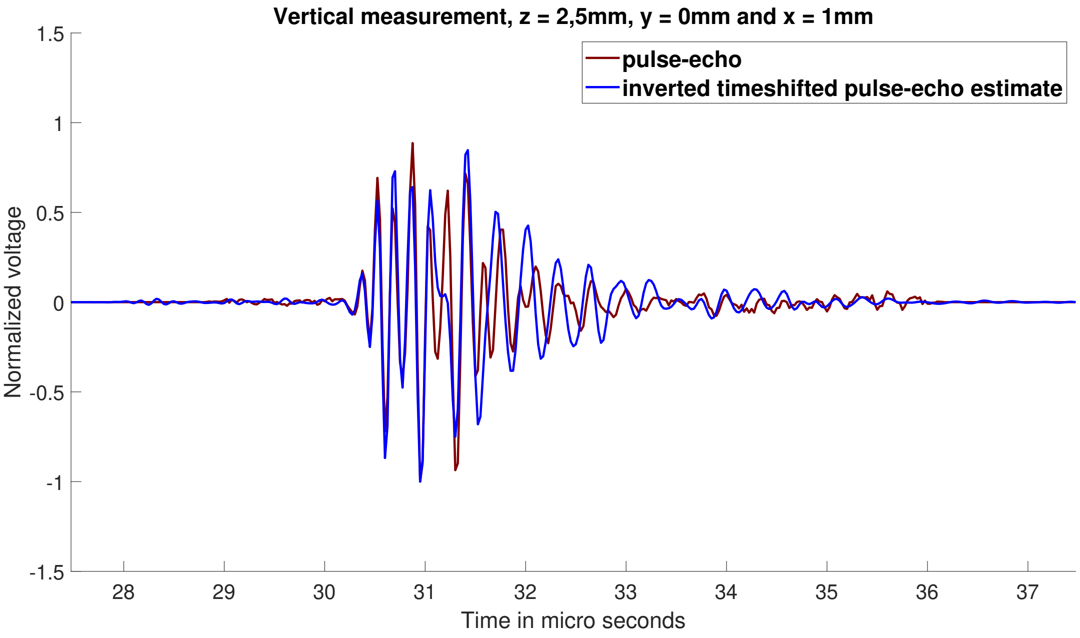

(b)

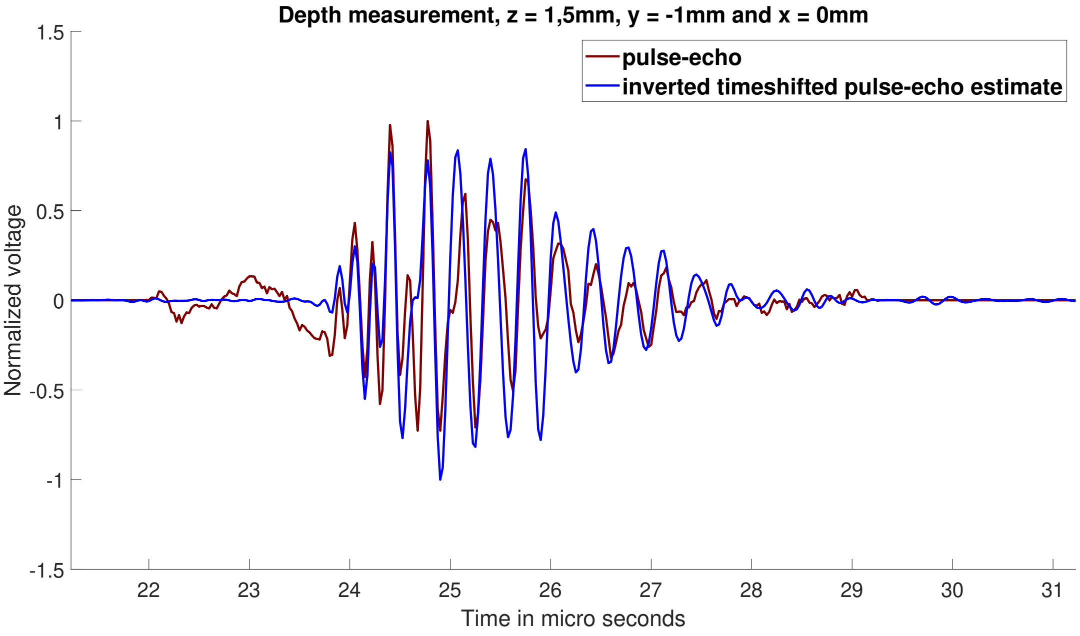

(c)

Figure 12: Measurement results for horizontal (a), vertical (b) and Depth (c) measurements after time shift and inversion of pulse-echo estimate measurements

Its self evident that they align a lot closer together then before, although not perfectly, and there is at least still a margin of error. To quantify the margin of error the following error criterion has been chosen.

$$Error = \left\| \frac{\mathbf{y_i}}{\|\mathbf{y_i}\|_2} - \frac{\mathbf{x_i}}{\|\mathbf{x_i}\|_2} \right\|_2$$

$$\mathbf{y_i} = \begin{bmatrix} \mathbf{y_i}(\omega_1) \\ \mathbf{y_i}(\omega_2) \\ \vdots \\ \mathbf{y_i}(\omega_M) \end{bmatrix} \quad \mathbf{x_i} = \begin{bmatrix} \mathbf{x_i}(\omega_1) \\ \mathbf{x_i}(\omega_2) \\ \vdots \\ \mathbf{x_i}(\omega_M) \end{bmatrix} \tag{44}$$

Where $\mathbf{y_i}$ is the $i$the pulse echo measurement with M frequencies and $\mathbf{x_i}$ is the i pulse-echo estimate measurement or inverted time shifted pulse-echo estimate measurement. The division by the 2 norm is to set the energy of both signals to 1. This enables us to compare the waveforms accurately on a scale from 0 to 2. The effect of the inversion and time shifting on the fit of the wave form is shown below:

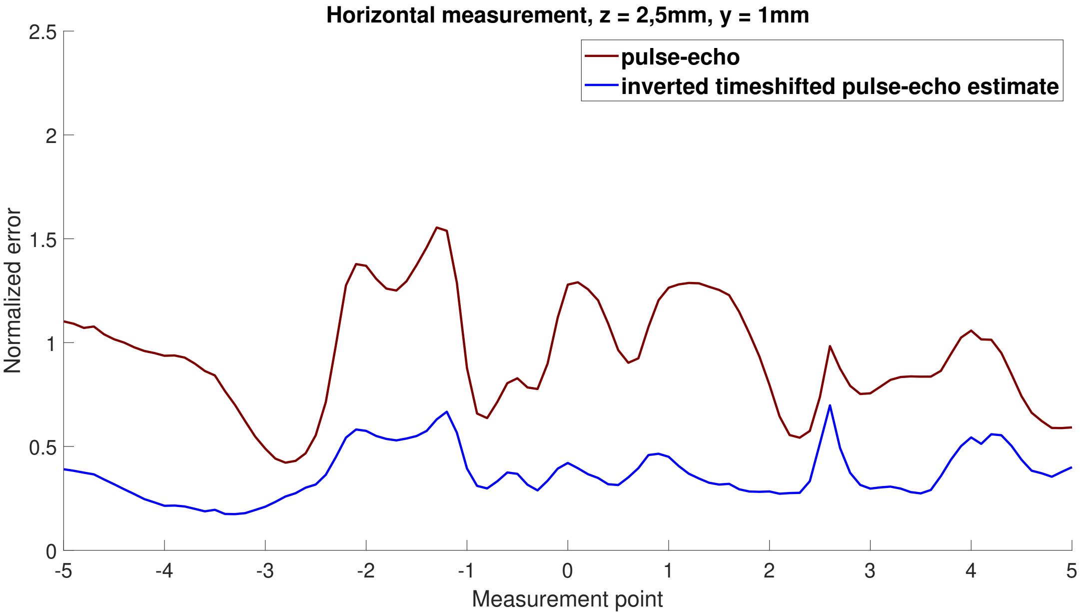

(a)

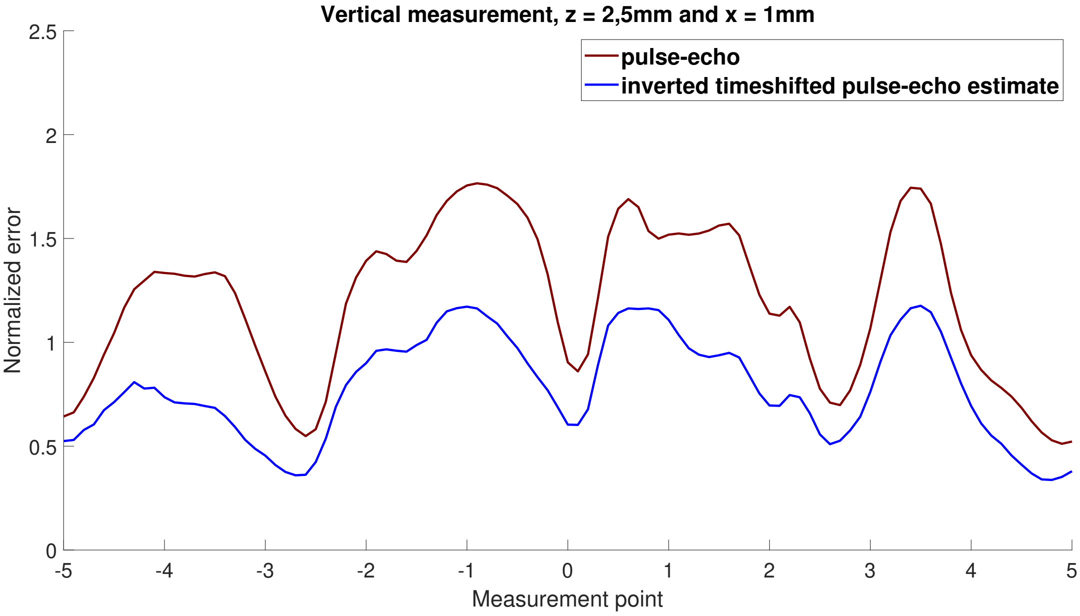

(b)

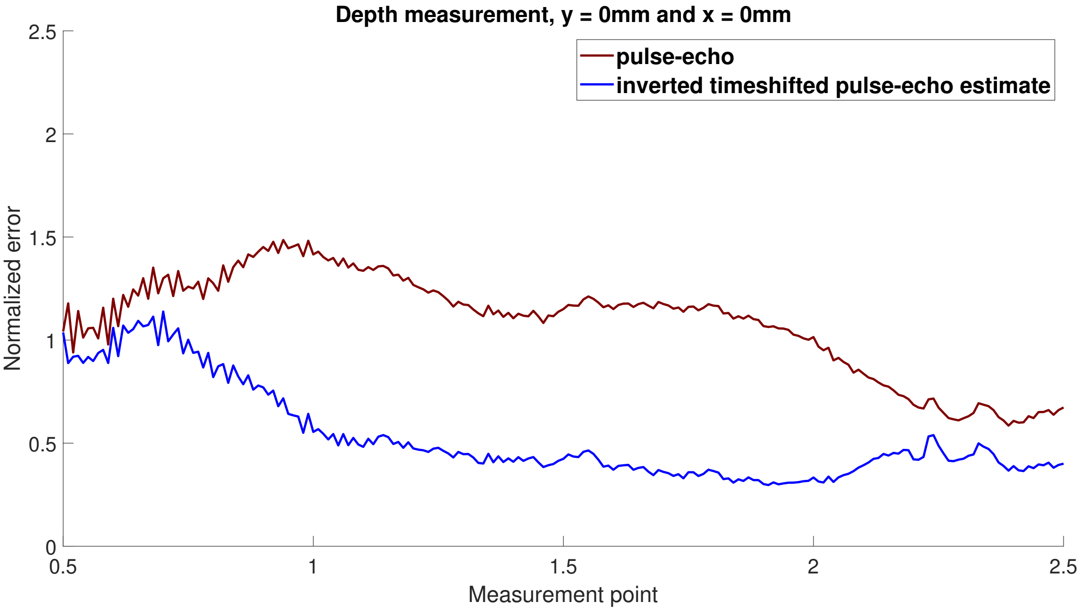

(c)

Figure 13: Waveform error of pulse-echo estimate and inverted time shifted pulse-echo estimate for horizontal (a), vertical (b) and Depth (c) measurements

Validating the results of the visual inspection of the time signal and the error criterion shows that the fit of the waveform has improved. However, the difference is still not zero and the same visual inspection of the time signal reveals that there is room for improvement. To examine where this possible improvement can be had, the Fourier transform of the time signals were taken.

It should at this point be pointed out that the time shift and inversion of the signal have no effect on the frequency spectrum of the signal. The time shift translates to phase shift in the frequency domain and the inversion is a multiplication that is unaffected by the Fourier transform. Given the fact that the spectrum is taken to be the absolute value of the Fourier transform, the effect of multiplying with -1 is invisible in the spectrum.

Below the side by side comparison of time and frequency spectrum is shown:

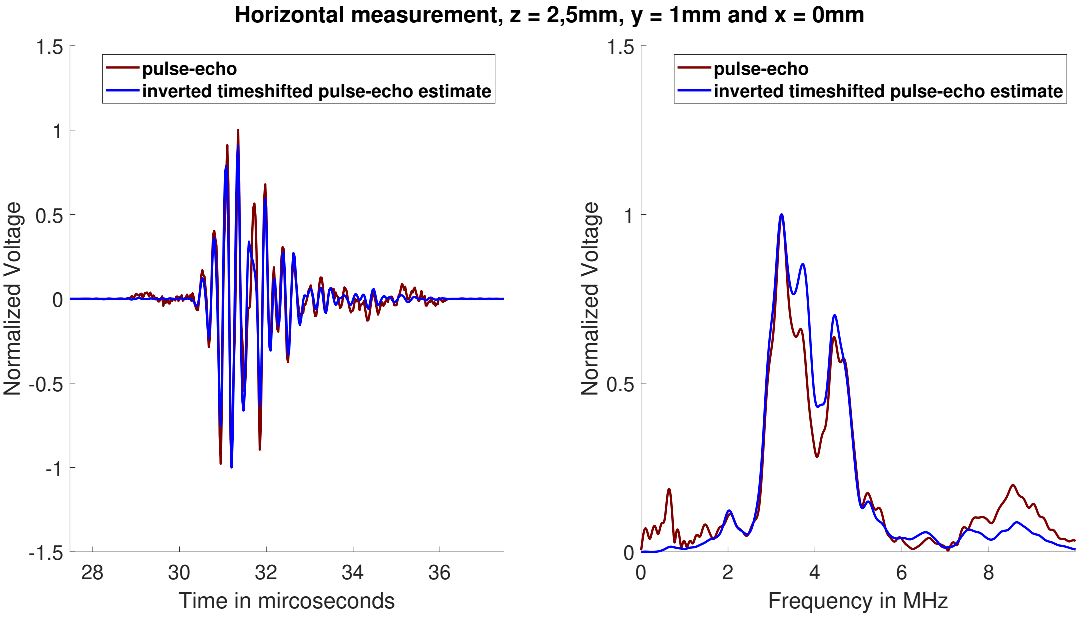

(a)

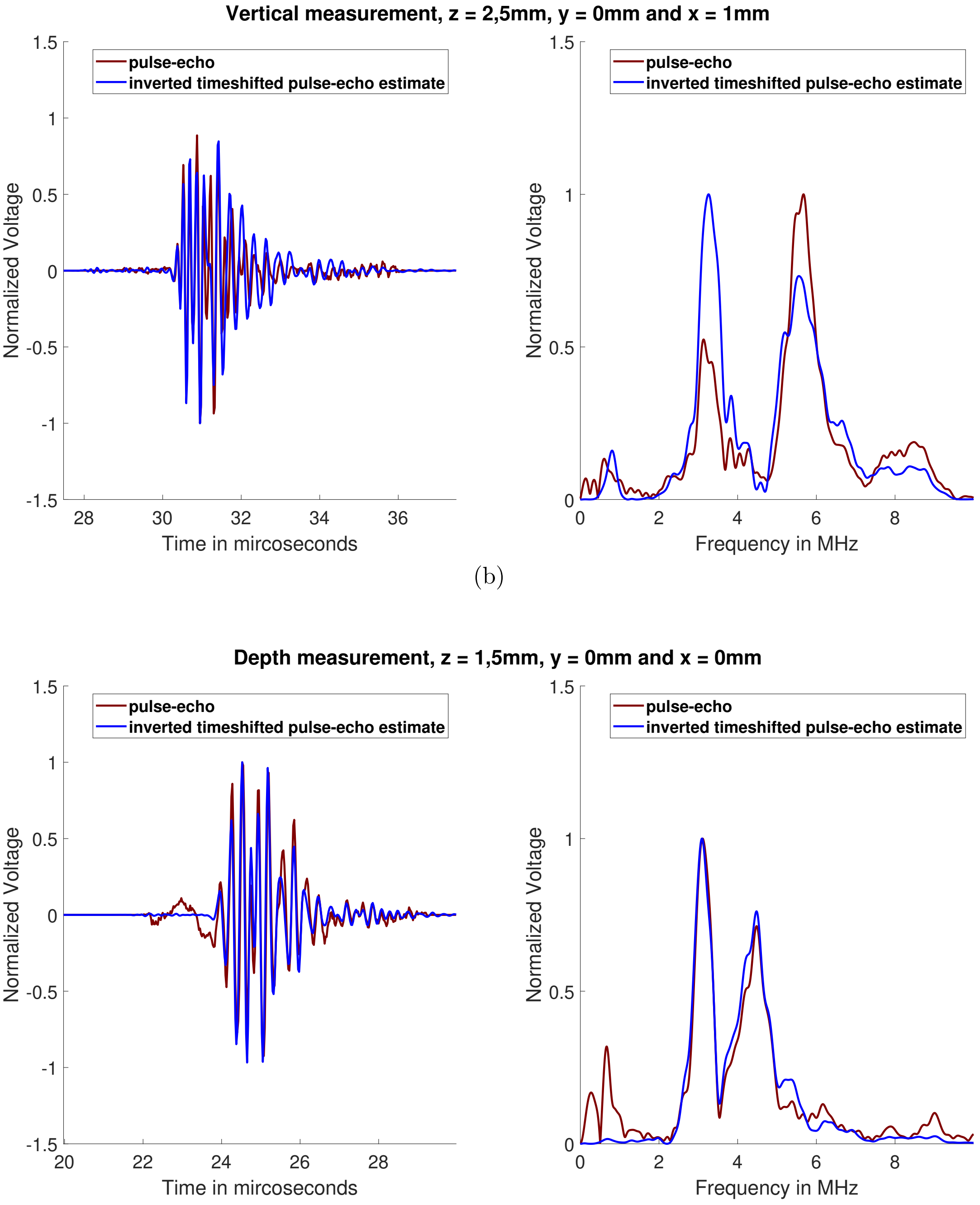

(b)

(c)

Figure 14: Time domain signals and associated FFT spectrums of horizontal (a), vertical (b) and Depth (c) measurements

From these images its clear that part of the signal is being filtered out or suppressed in the pulse-echo estimate measurement that is present within the pulse echo measurement. Having earlier recognised that the previous 2 adjustments have a frequency domain counterpart it seems logical to try and improve the fit in the frequency domain to obtain a more perfect fit between the pulse echo and the pulse-echo estimate measurement.

3.4 The calibration method

Having found a significant set of differences between the pulse-echo estimate measurement and the pulse echo measurement, and having recognised they can be solved in the frequency domain, there are 2 paths forward. The first path is to separately analyse each component of equation (40) and determining their contribution to the total error and the compensate for each individually. The second path is trying to compensate for the found error as a whole instead of its separate components. The latter approach was chosen due to the fact a majority part of the expected reason for the error are position independent and are therefore assumed constant across all measurements. Using this assumption that the error in constant we can try and compute a compensation vector $\mathbf{c}$ that will mitigate or outright cancel out this constant error or in mathematical terms:

$$p_k(t) = h_k(t) * c(t) \tag{45}$$

Where $p_k(t)$ is the $k$the pulse echo measurement, $h_k(t)$ is the corresponding $k$the pulse-echo estimate measurement and $c(t)$ is the compensation vector. Given the more challenging nature of working with convolutions and having shown that part of the improvements must be done in the frequency domain, the FFT is applied to equation (45) resulting in:

$$p_k(\omega) = h_k(\omega)c(\omega) \tag{46}$$

And in vector form this is:

$$\begin{bmatrix} p_k(\omega_1) \\ p_k(\omega_2) \\ \vdots \\ p_k(\omega_M) \end{bmatrix} = \begin{bmatrix} h_k(\omega_1) \\ h_k(\omega_2) \\ \vdots \\ h_k(\omega_M) \end{bmatrix} \odot \begin{bmatrix} c(\omega_1) \\ c(\omega_2) \\ \vdots \\ c(\omega_M) \end{bmatrix} \tag{47}$$

where M is the highest frequency bin index of the signal. Even though we assume the error to be constant for all measurements that does not mean that there is no noise. The surrounding noise and measurement noise due to material imperfection in the various components of the setup will add a measure of noise. In the theoretical derivation we modelled this as white Gaussian noise. To reduce the impact of this noise in our quest to find this constant error we use all the available pulse echo measurements and their corresponding pulse-echo estimate measurements to compute the compensation vector $\mathbf{c}$. First we define the following variables:

$$\mathbf{p_k} = \begin{bmatrix} p_k(\omega_1) \\ \vdots \\ p_k(\omega_M) \end{bmatrix} \quad diag(\mathbf{h_k}) = \begin{bmatrix} h_k(\omega_1) & 0 & \dots & 0 \\ 0 & h_k(\omega_2) & \dots & 0 \\ \vdots & \vdots & \ddots & \vdots \\ 0 & 0 & \dots & h_k(\omega_M) \end{bmatrix} \tag{48}$$

Then we combine them as follows:

$$\begin{bmatrix} \mathbf{p_1} \\ \mathbf{p_2} \\ \vdots \\ \mathbf{p_K} \end{bmatrix} = \begin{bmatrix} diag(\mathbf{h_1}) \\ diag(\mathbf{h_2}) \\ \vdots \\ diag(\mathbf{h_K}) \end{bmatrix} \begin{bmatrix} c(\omega_1) \\ \vdots \\ c(\omega_M) \end{bmatrix} \tag{49}$$

where K is the total number of pulse echo measurements with corresponding pulse-echo estimate measurements. This equation can be rewritten in to the matrix form to obtain a equation for the compensation vector $\mathbf{c}$:

$$\mathbf{p} = \mathbf{Hc} \tag{50}$$

Where $\mathbf{p}$ is the left hand side of equation (49) and represents all the Pulse echo measurements, $\mathbf{H}$ is the middle matrix of equation (49) and represents all the pulse-echo estimate measurements and $\mathbf{c}$ is the compensation vector that we are trying to find. This compensation vector $\mathbf{c}$ tries to minimise the difference between $\mathbf{p}$ and $\mathbf{H}$ therefore we can pose it as the following minimisation problem:

$$\underset{\mathbf{c}}{\text{minimize}} \quad ||\mathbf{p} - \mathbf{Hc}||_2^2 \tag{51}$$

This minimisation problem is convex but has infinite many solutions due to the large amount of degrees of freedom. These degree's of freedom stem from the fact that not all the frequencies in $\mathbf{H}$ are directly associated with the signal and due to the complex conjugate nature of frequency spectrums, contain many linear combinations. The easiest and fastest way to show the rank of $\mathbf{H}$ is by computing its singular values.

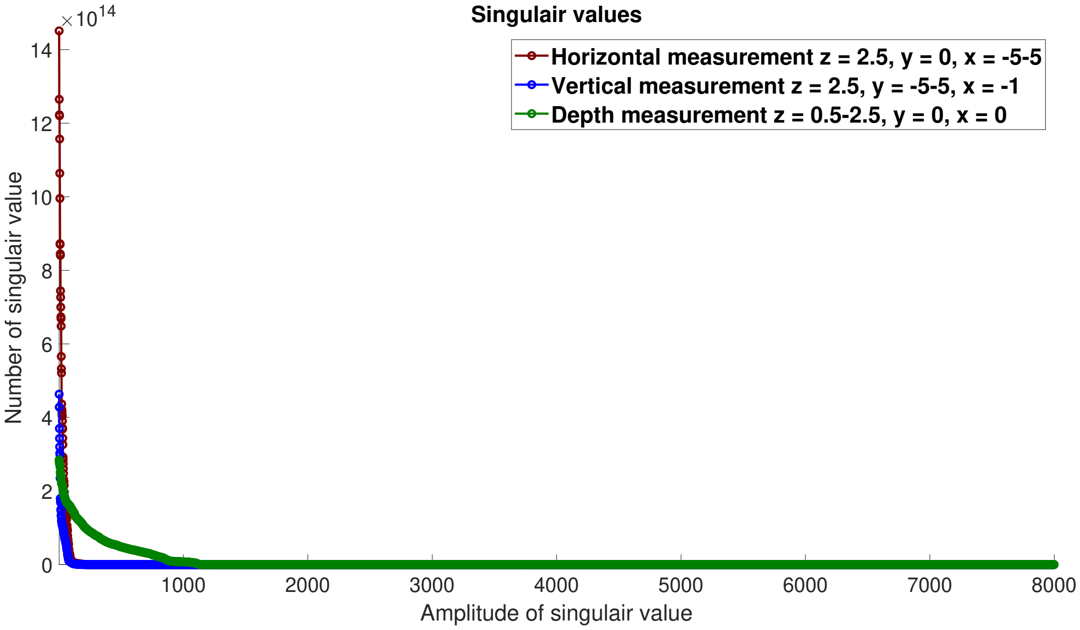

Figure 15: Singular values of the matrix **H**

The singular values that are not approximately zero show the rank of the matrix **H**.Due to the absence of any prior information regarding the correct solution from the infinitely many solutions that equation (51) offers it was decided to use the standard approach for such cases. Namely the Tikhonov regularization:

$$\underset{\mathbf{c}}{\text{minimize}} \quad ||\mathbf{p} - \mathbf{Hc}||_2^2 + \lambda||\mathbf{c}||_2^2 \tag{52}$$

The Tihonov regularized least squares selects the compensation vector **c** from the solution space with the least amount of energy. Which is equivalent to saying we want a smooth and/or a non-sparse solution. Based on observations made from the images shown in figure 14 this seems to be a good idea.

In the interest of expedience the analytical solution has been derived by first expending the squares in the minimisation:

$$\mathbf{p}^H\mathbf{p} - \mathbf{p}^H\mathbf{Hc} - \mathbf{c}^H\mathbf{H}^H\mathbf{p} + \mathbf{c}^H\mathbf{H}^H\mathbf{Hc} + \lambda\mathbf{c}^H\mathbf{c} \tag{53}$$

Then to find the minimum value for **c**, the derivative is taken with respect to $\mathbf{c}^H$ and set it to zero:

$$-\mathbf{H}^H\mathbf{p} + 2\mathbf{H}^H\mathbf{Hc} + 2\lambda\mathbf{c} = 0 \tag{54}$$

Now its just a matter of moving the terms around till **c** remains on one side:

$$\mathbf{c} = \frac{1}{2}(\mathbf{H}^H\mathbf{H} + \lambda\mathbf{I})^{-1}\mathbf{H}^H\mathbf{p} \tag{55}$$

The value of λ has been chosen by examining a large set of values for λ from 0.0001 to 1000000 and the best results where obtained with a value of 0.01. To determine the effect of the method, the compensation vector **c** was computed and the result of its application on the pulse-echo estimate measurements in the frequency spectrum is shown below:

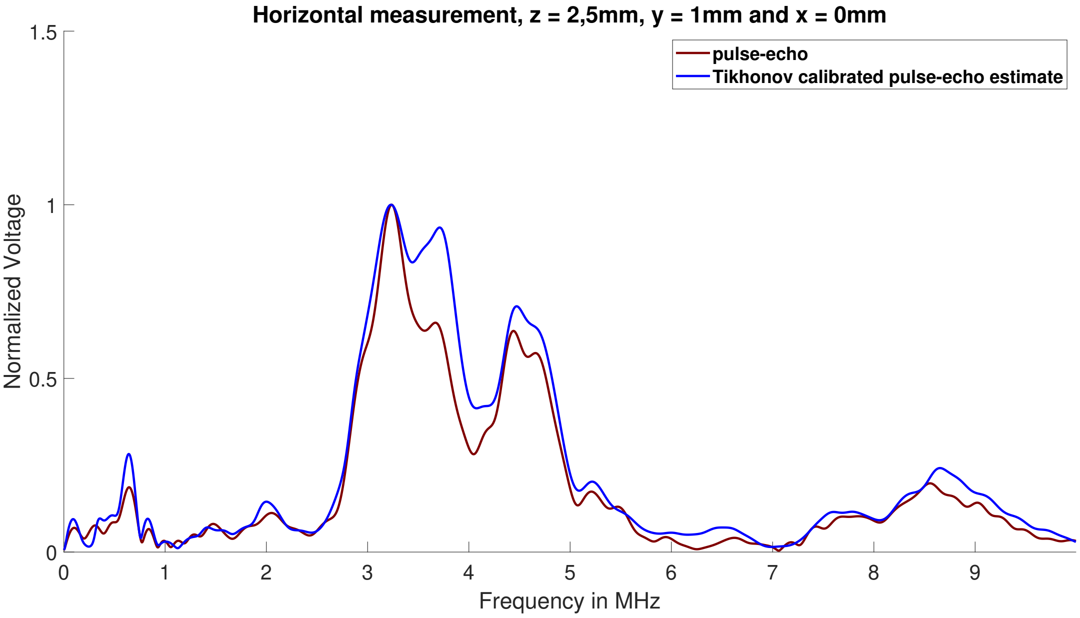
Horizontal measurement, z = 2,5mm, y = 1mm and x = 0mm
pulse-echo
Tikhonov calibrated pulse-echo estimate
Normalized Voltage
1.5
1
0.5
0
0
1
2
3
4
5
6
7
8
9
Frequency in MHz

(a)

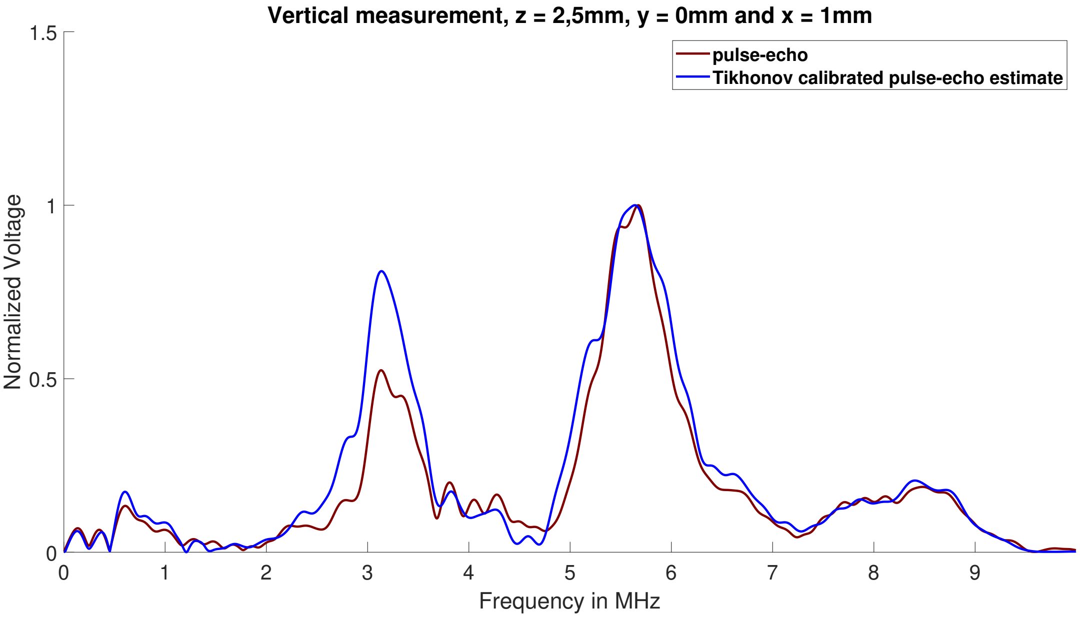
Vertical measurement, z = 2,5mm, y = 0mm and x = 1mm
pulse-echo
Tikhonov calibrated pulse-echo estimate
Normalized Voltage
1.5
1
0.5
0
0
1
2
3
4
5
6
7
8
9
Frequency in MHz

(b)

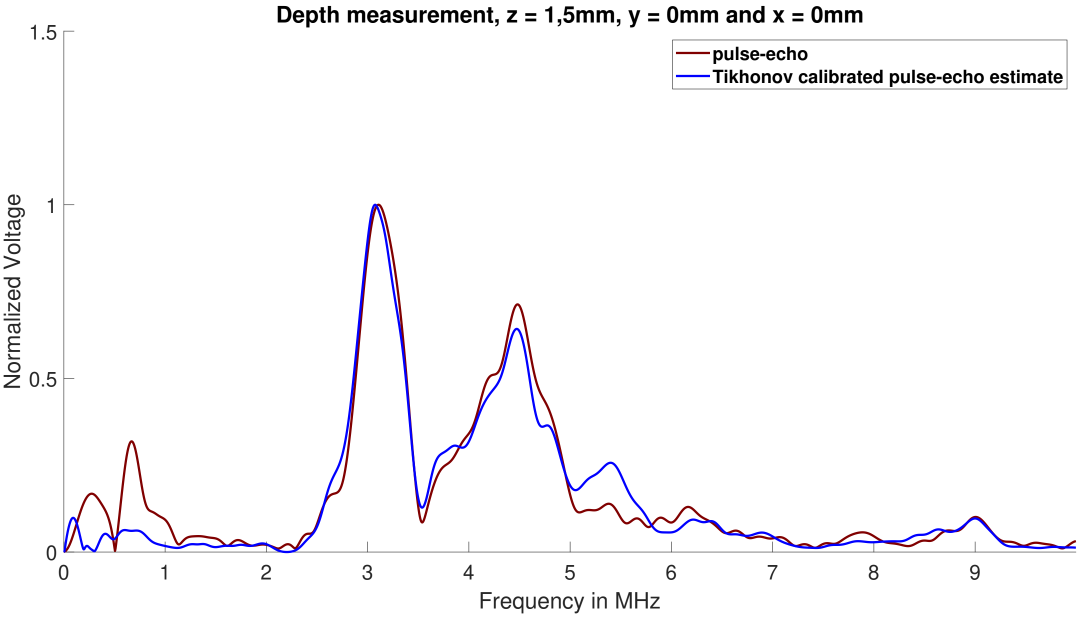

(c)

Figure 16: FFT spectrum of Tikhonov calibrated horizontal (a), vertical (b) and Depth (c) pulse-echo estimate and Pulse echo measurements

It clearly shows that the fit of these signals has improved significantly compared to the results obtained in figure 14, only at more sharp transitions and when the signal has low energy and is more dominated by its noise content does it mismatch. This mismatch is inherent to the method given the forcing of generalisation through the regularisation term. Furthermore, the mismatch in the region of 0-2MHz and 8-10MHz is due to the fact that there is no signal in these regions and therefore the method can only try and fit noise. Even though these small objections, its a significant improvement compared to just the time shifted and inverted signal that was previously used as shown below:

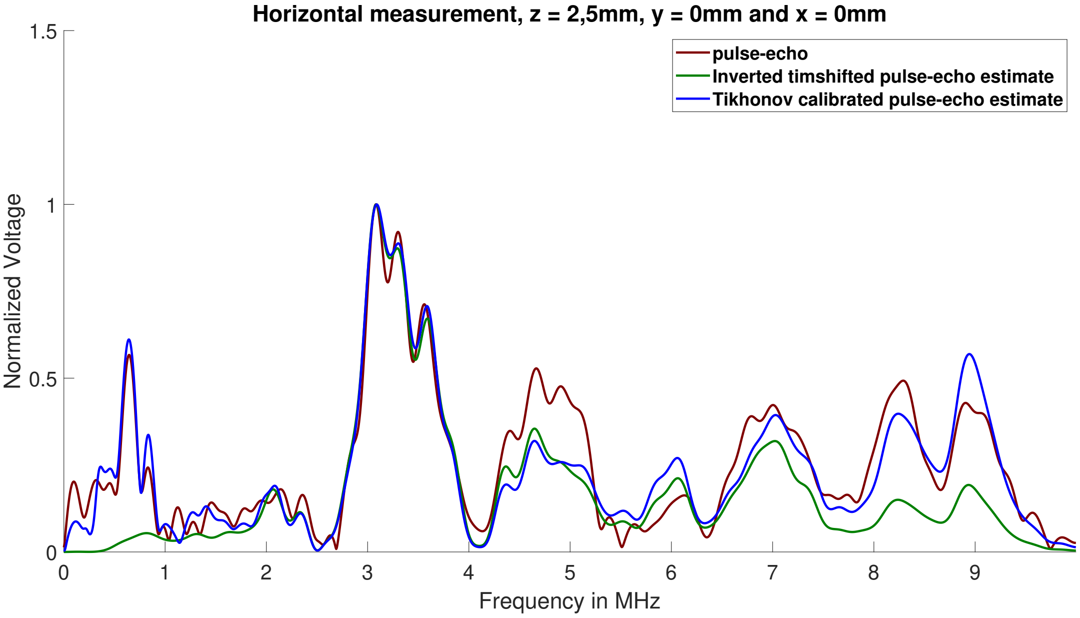

(a)

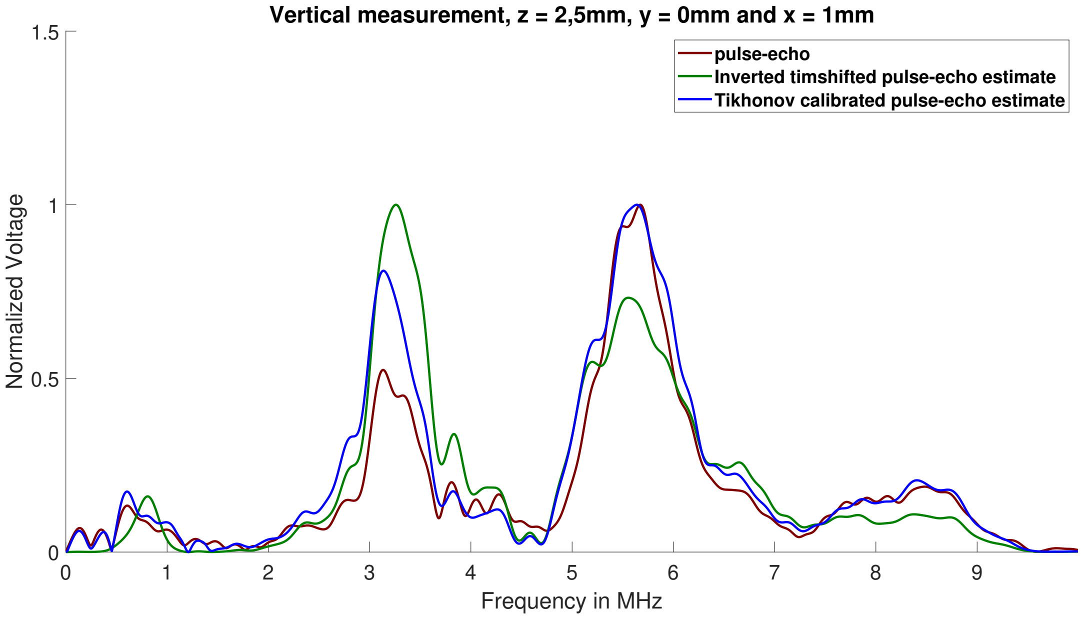

(b)

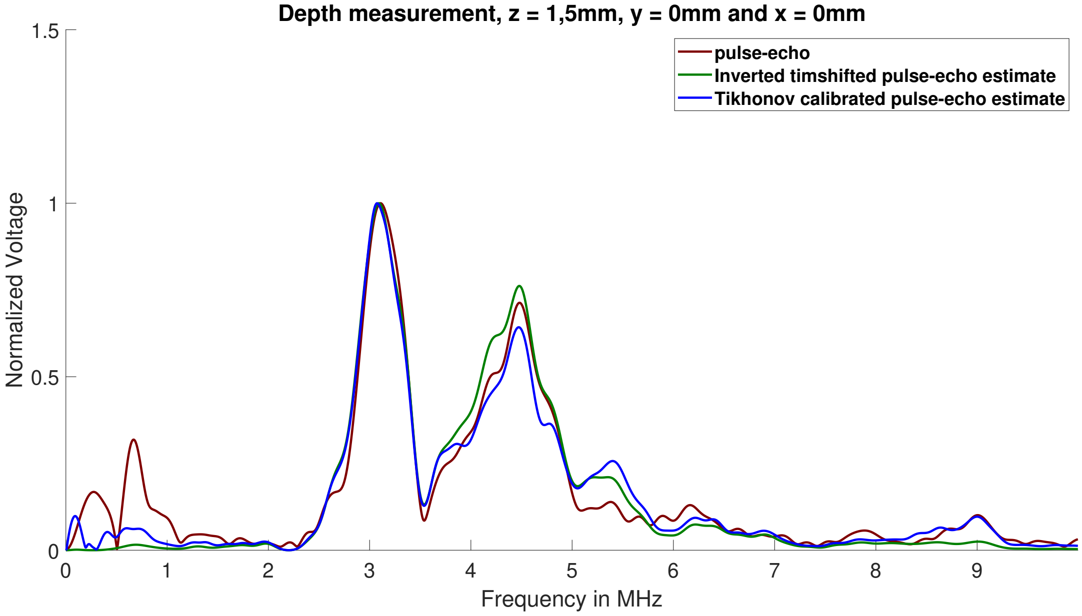

(c)

Figure 17: FFT spectrum of Tikhonov calibrated horizontal (a), vertical (b) and Depth (c) pulse-echo estimate and Pulse echo measurements

Given that the spectrum shown doesn't contain the phase information where the time shifted technique is mostly effective, the inverse Fourier transform was applied and the time signal was recovered.

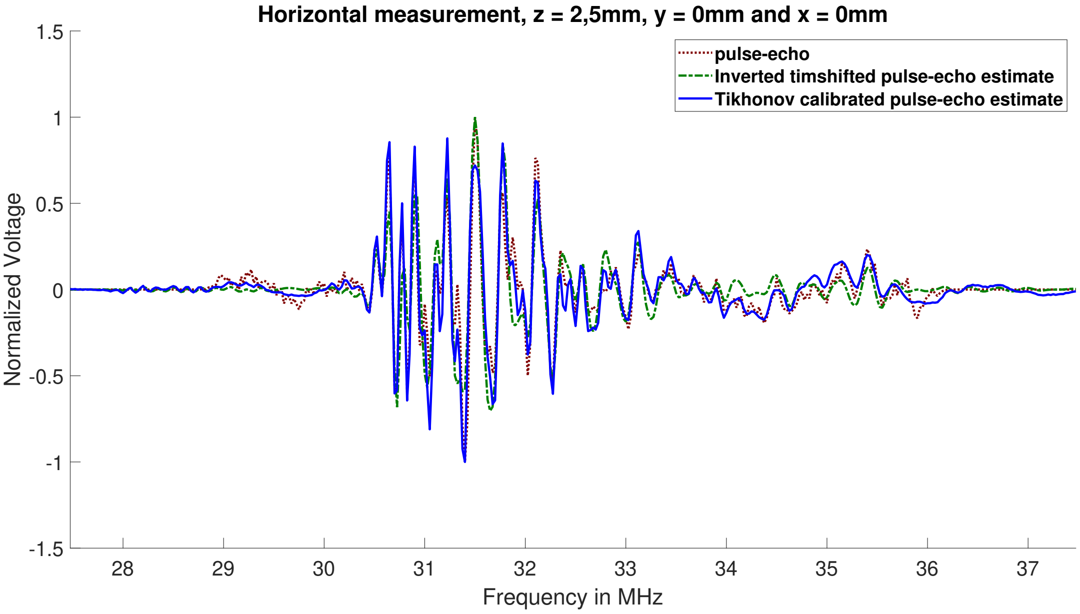
Horizontal measurement, z = 2,5mm, y = 0mm and x = 0mm
pulse-echo
Inverted timshifted pulse-echo estimate
Tikhonov calibrated pulse-echo estimate
Normalized Voltage
Frequency in MHz
1.5
1
0.5
0
-0.5
-1
-1.5
28
29
30
31
32
33
34
35
36
37

(a)

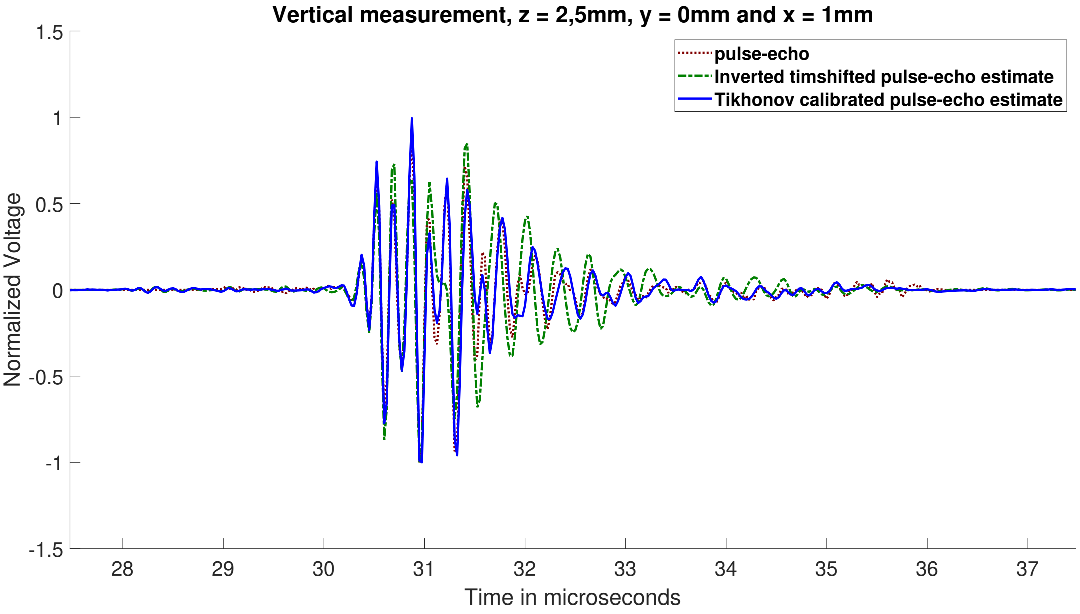
Vertical measurement, z = 2,5mm, y = 0mm and x = 1mm
pulse-echo
Inverted timshifted pulse-echo estimate
Tikhonov calibrated pulse-echo estimate
Normalized Voltage
Time in microseconds
1.5
1
0.5
0
-0.5
-1
-1.5
28
29
30
31
32
33
34
35
36
37

(b)

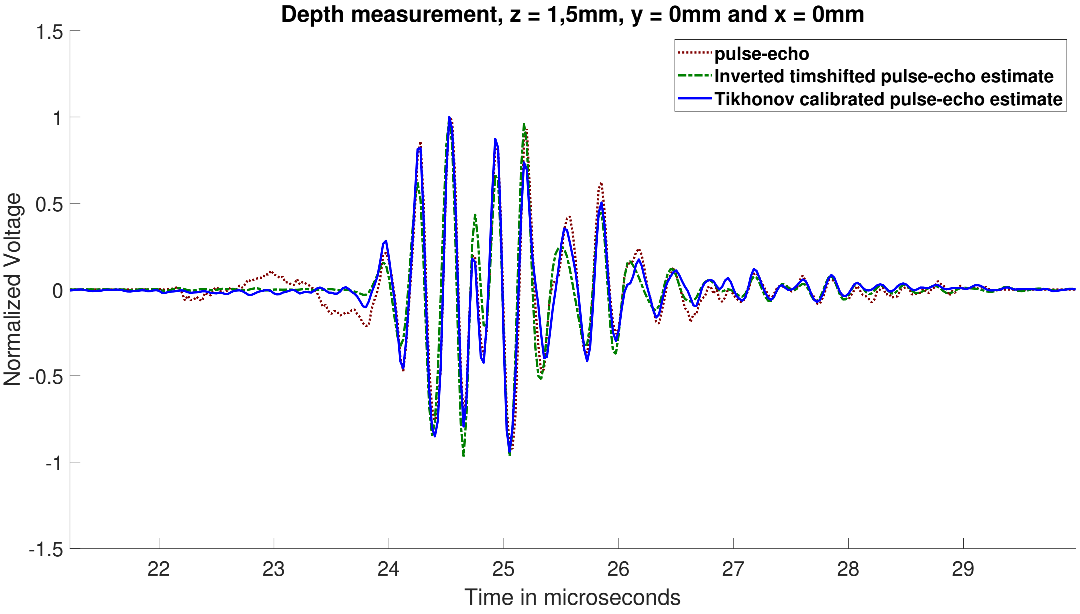

(c)

Figure 18: Time signal of horizontal (a), vertical (b) and Depth (c) Pulse echo, Inverted Time shifted pulse-echo estimate and Tikhonov Calibrated pulse-echo estimate

From this comparison the effectiveness of the Tikhonov calibration method is self evidently the best and for now a good enough solution. To determine how well it preforms across all points and the same error function as described in equation 44 has been defined for the difference in the time domain:

$$Error = \left\| \frac{\mathbf{y_i}}{\|\mathbf{y_i}\|_2} - \frac{\mathbf{x_i}}{\|\mathbf{x_i}\|_2} \right\|_2$$

$$\mathbf{y_i} = \begin{bmatrix} \mathbf{y_i}(\omega_1) \\ \mathbf{y_i}(\omega_2) \\ \vdots \\ \mathbf{y_i}(\omega_M) \end{bmatrix} \qquad \mathbf{x_i} = \begin{bmatrix} \mathbf{x_i}(\omega_1) \\ \mathbf{x_i}(\omega_2) \\ \vdots \\ \mathbf{x_i}(\omega_M) \end{bmatrix} \tag{56}$$

Where $\mathbf{y_i}$ is the ith pulse echo measurement and $\mathbf{x_i}$ is either the $i$the pulse-echo estimate measurement, inverted time shifted pulse-echo estimate measurement or the Tikhonov calibrated pulse-echo estimate measurement. The results of this error computation results in the following plot:

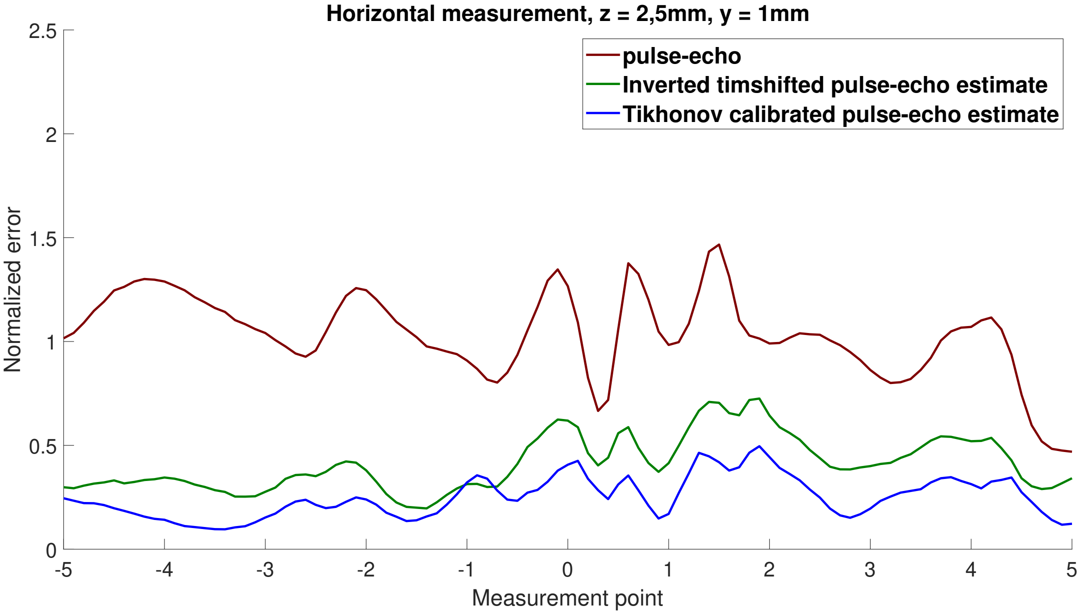

(a)

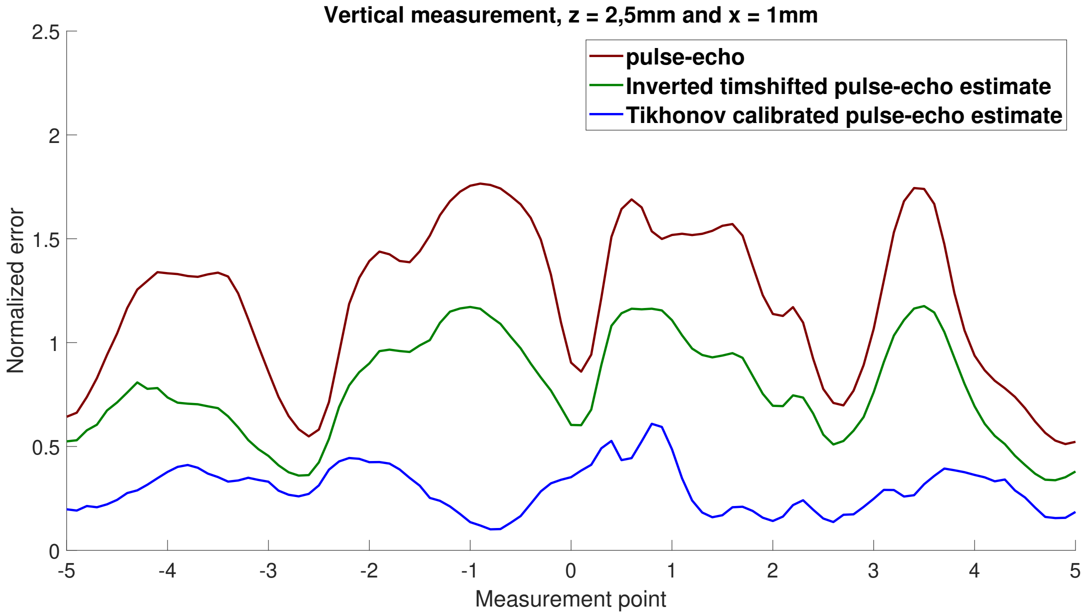

(b)

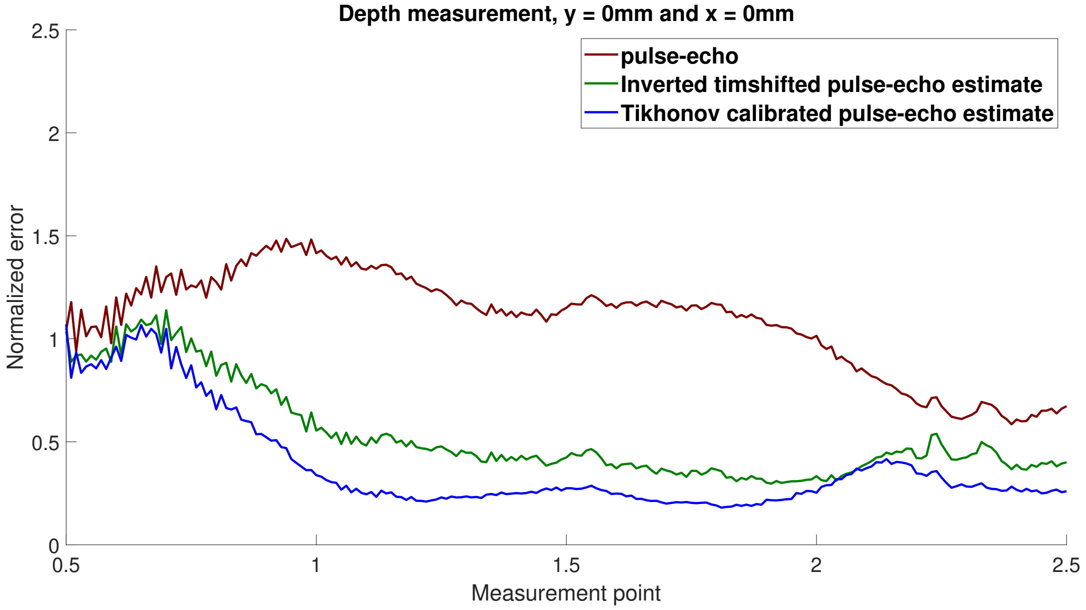

(c)

Figure 19: Waveform error of horizontal (a), vertical (b) and Depth (c) Inverted Time shifted, Tikhonov Calibrated and original pulse-echo estimate measurements

The low error shows that the waveforms are almost identical and as a added benefit the Tikhonov signal also scales the signal to the correct value.

3.5 Single point imaging

After having found an error in the measurement setup and obtained a calibration method to compensate for this error, the question is how much teh calibrated model improves the image. Therefore, using the data obtained from the measurements as described in chapter 3.2.2 a line imaging experiment is preformed and by stacking the separate line measurements, a limited 2D imaging scenario is obtained.

3.5.1 Imaging method

Before we are able to show the result, first the method of obtaining the image has to be described. In chapter 2 we derived the model for our imaging experiments, namely:

$$\mathbf{y} = \mathbf{A}\mathbf{x} + \mathbf{n} \tag{57}$$

Now as stated in the same chapter, this concerns a inverse scattering problem that is usually ill-posed. To determine if the same applies here, the singular values of $\mathbf{A}$ have been computed:

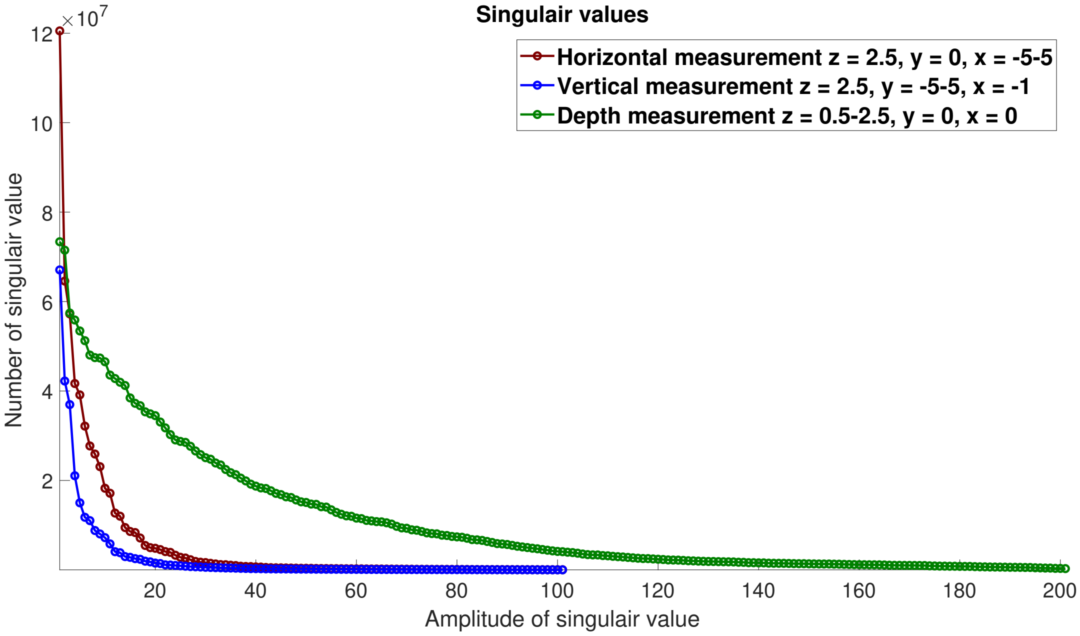

Figure 20: Singular values of the matrix $\mathbf{A}$

The number of singular values for the depth measurements (denoted dens depth) are twice as high due to the fact that more pixels where measured. Clearly we can see that a large amount of values are close to zero and therefore, we can conclude that A is rank deficient and the problem is ill-posed. Therefore, it was decided to use the same method for imaging as for calibration, namely the Tikhonov regularised least squares given by:

$$\underset{\mathbf{x}}{\text{minimize}} \quad ||\mathbf{y} - diag(\mathbf{c})\mathbf{A}\mathbf{x}||_2^2 + \lambda||\mathbf{x}||_2^2 \tag{58}$$

For the 1D case all the used data came from one single experiment (for instance 1.c) as described in chapter 3.2.2 and the various vectors and matrices are constructed as follows:

$$\mathbf{y} = \begin{bmatrix} y(\omega_1) \\ y(\omega_2) \\ \vdots \\ y(\omega_M) \end{bmatrix} \quad \mathbf{c} = \begin{bmatrix} c(\omega_1) \\ c(\omega_2) \\ \vdots \\ c(\omega_M) \end{bmatrix} \quad \mathbf{A} = \begin{bmatrix} a_1(\omega_1) & \dots & a_K(\omega_1) \\ \vdots & \ddots & \vdots \\ a_1(\omega_M) & \dots & a_K(\omega_M) \end{bmatrix} \quad \mathbf{x} = \begin{bmatrix} x_1 \\ x_2 \\ \vdots \\ x_K \end{bmatrix} \tag{59}$$

Where $\mathbf{y}$ is 1 of the pulse echo measurement taken from the pool of measurements with M frequencies, $\mathbf{A}$ is constructed by taking K measurements from the pool of pulse-echo estimate measurements(in this case all measurements are taken from the pool) and $\mathbf{x}$ is our image that will be reshapen in the 2D case to create our image.

For the 2D case, the pool of measurements is expanded by using all the experiments that are connected to the horizontal or vertical measurements (1,2). The vector $\mathbf{y}$ remains the same but the pool of measurements where it can be drawn from is expanded as previously described. The model $\mathbf{A}$ is expanded upon as follows:

$$A_{2D} = \begin{bmatrix} diag(\mathbf{c_a})\mathbf{A_a} & diag(\mathbf{c_b})\mathbf{A_b} & diag(\mathbf{c_c})\mathbf{A_c} & diag(\mathbf{c_d})\mathbf{A_d} & diag(\mathbf{c_e})\mathbf{A_e} \end{bmatrix} \tag{60}$$

Where the subscript (a,b,c,d,e) references to the measurements of a single line measurements as described in chapter 3.2.2 that are part of the pool of measurements and the vector $\mathbf{x}$ is expanded to accommodate all the possible locations that are now within the image domain.

And finally the regularisation term λ in both cases is found by scanning over a large set of possible values ranging from 10^{-20} to 10^{20} with increments of 1 order at the time. Then through visual inspection the best possible value was selected for all the measurements.

3.5.2 1D Imaging

The goal of the image experiment shown here is to image a point on a line. This experiment will give us an indication of the point spread function and show the improvement in image reconstruction. The results are shown below:

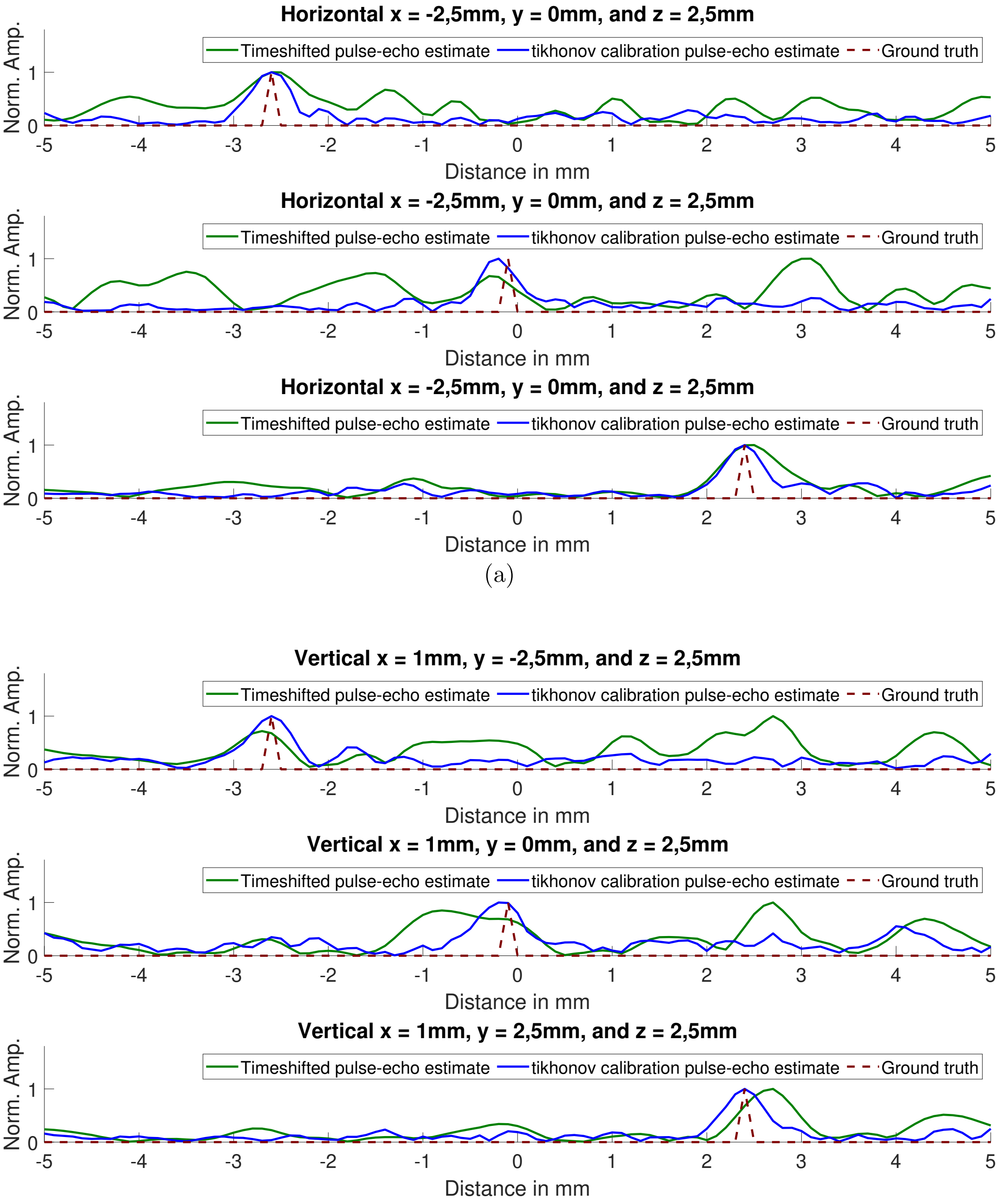

(a)

(b)

Figure 21: 1D imaging results for horizontal (a) and vertical (b) measurements

Its directly clear that using the calibrated model it was possible to determine the location of the point under image with a point spread function (PSF) of 0.8mm. The uncalibrated signal is able to successfully locate the point in some cases but not consistently due to the error that is still within the model. The results obtained in the past contained multiple translations and/or multiple rotations of the mask enabling for a better posed problem due to the added measurements, resulting a better image overall. For depth the following result was obtained:

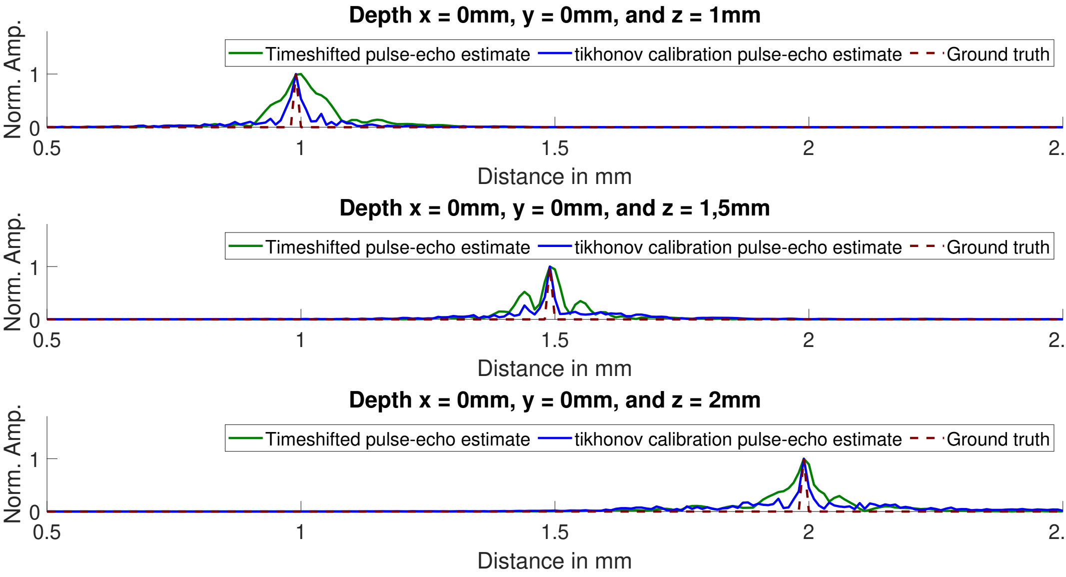

Figure 22: 1D imaging results for depth measurements

Given the fact that time of arrival is a much larger contributing factor to determining the depth it is possible to estimate the depth components significantly better then the horizontal and vertical component. When the point moves closer to the ultrasound element the estimation becomes worse due to the effect described in chapter 3.2.3.

3.5.3 2D Imaging

Given the success of the point on a line imaging in the previous section, an extension to the 2D domain was made by combining the measurements of the different lines in to a 2D matrix as previously described. For accurate comparison to the uncalibrated case, the same image experiment is preformed using the timeshifted but uncalibrated model. And finally it should be noted that the resolution in the direction of the experiment is 0.1mm but in the other direction is only 1mm. This is due to how the experiments where performed, the results:

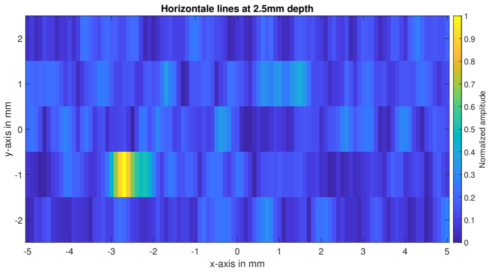

Figure 23: Limited 2D horizontal imaging after calibration, point on y =-1mm and x = -2,6mm

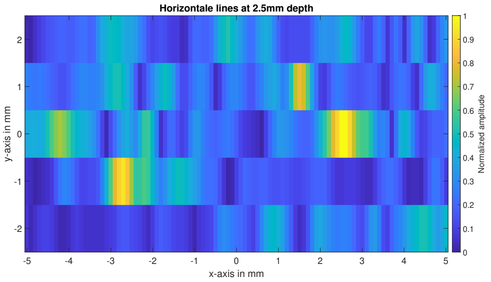

Figure 24: Limited 2D horizontal imaging without calibration, point on y =-1mm and x = -2,6mm

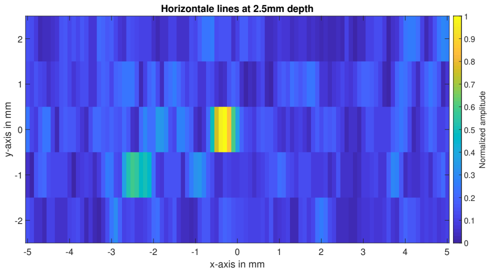

Figure 25: Limited 2D horizontal imaging after calibration, point on y = 0mm and x = -0,4mm

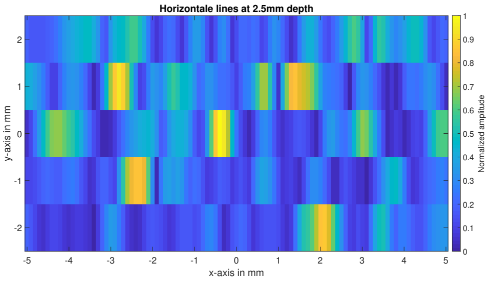

Figure 26: Limited 2D horizontal imaging without calibration, point on y = 0mm and x = -0,4mm

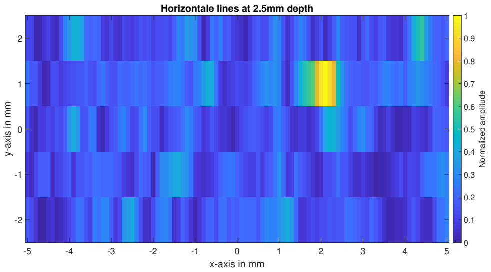

Figure 27: Limited 2D horizontal imaging after calibration, point on y = 1mm and x = 2,1mm

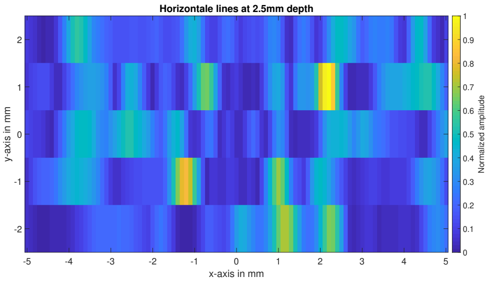

Figure 28: Limited 2D horizontal imaging without calibration, point on y = 1mm and x = 2,1mm

From the reconstruction of the 3 points in the ”horizontal 2D” image experiment it shows that its possible to obtain reliable measurements of these points with roughly the same PSF as found in the line imaging. The uncalibrated method was unable to reliably obtain the point under imaging, also in line with the results of the line imaging experiments. The PSF in case of the proper identification of the point is larger then in the calibrated case. Now for the ”vertical 2D” imaging:

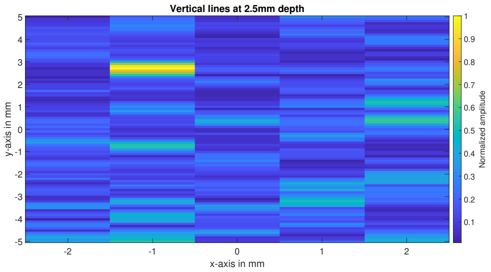

Figure 29: Limited 2D vertical imaging after calibration, point on y = 2,6mm and x =-1mm

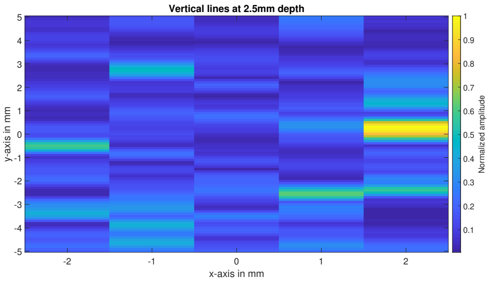

Figure 30: Limited 2D vertical imaging without calibration, point on y = 2,6mm and x =-1mm

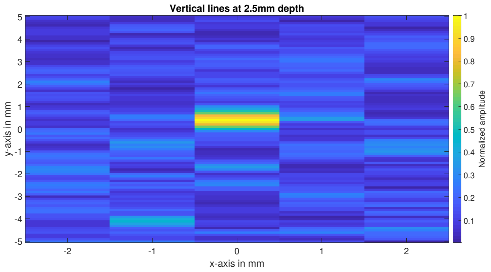

Figure 31: Limited 2D vertical imaging after calibration, point on y = 0,4mm and x = 0mm

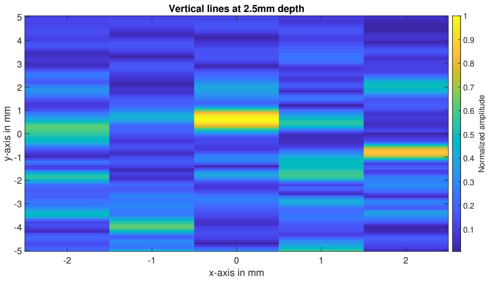

Figure 32: Limited 2D vertical imaging without calibration, point on y = 0,4mm and x = 0mm

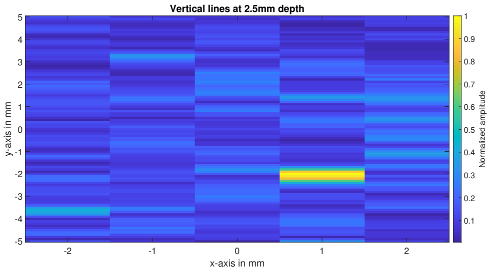

Figure 33: Limited 2D vertical imaging after calibration, point on y = -2,1mm and x =-1mm

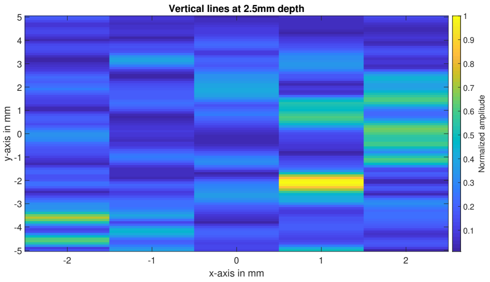

Figure 34: Limited 2D horizontal imaging without calibration, point on y = -2,1mm and x =-1mm

Its equally possible to rather accurately image a point. The depth measurements are absent here due to the fact that the prescribed set of measurements would result in either a 3D image or a 2D image with very little number of measurements. Therefore, it was decided to omit them at this time.

3.6 The compensation vector **c**

Having created the compensation vector **c**, applied it to the model and shown that it is capable of improving the image quality the question is, what does it look like? Below, the frequency spectrum and phase domain are shown:

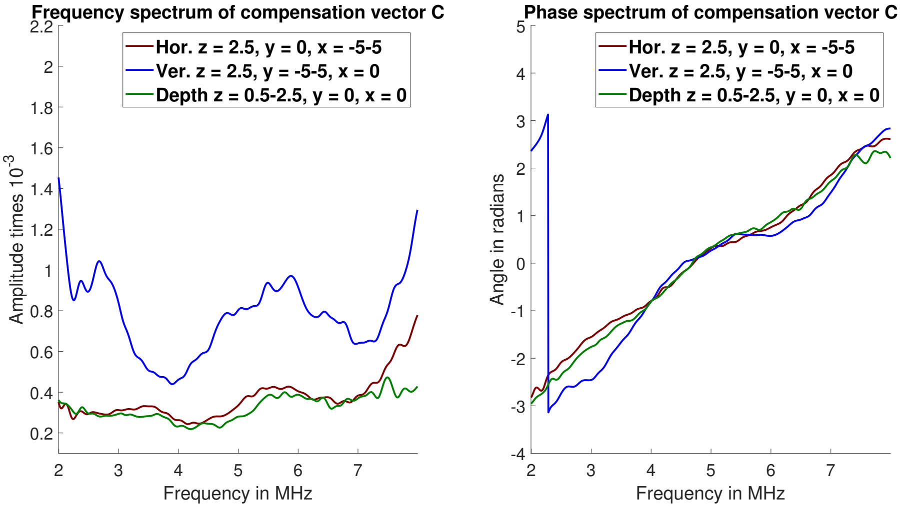

Figure 35: Left the frequency spectrum of the compensation vector **c**, right the phase spectrum of the compensation vector **c**

The frequency range is set between 2MHz and 8 MHz due to the fact that outside this domain there is no signal. The first clear observation is that the phase spectrum contains an almost linear line from $-\pi$ to π over a large band centred around the main operating frequency of 5MHz. This is consistent with the observations made in chapter 3.3 regarding the time delay and the spectrum shows a scaling difference that's more than just a scalar, clearly demonstrating why the inverted time-shifted domain solution resulted in a worse fit then the proposed calibration method. The edges of the approximately linear area of the angular spectrum coincide with the range on which the signal is strongly defined. Beyond these limits the signal is very weak and its hard to tell if its noise or signal that resides there. The large "jump" for the vertical compensation vector **c** is due to wrapping of the phase in Matlab.

4 Single measurement calibration

Having shown in the previous chapter that there exists a compensation vector $\mathbf{c}$ that is capable of improving the image quality and having seen that this vector contains a certain structure, the question is raised can we can we compute this calibration with only 1 measurement?

4.1 Analysis of single point compensation vector c

Having made plausible that the compensation done by the compensation vector is for a constant error, the first step is examining how well a single measurement point can be used to compensate for this error. To answer this question, the compensation vector $\mathbf{c}$ was computed as follows using only a single pulse echo measurement and its corresponding pulse-echo estimate measurement.

$$\mathbf{c_i} = \frac{\mathbf{y_i}}{\mathbf{x_i}} \tag{61}$$

Where $\mathbf{c}_i$, $\mathbf{y}_i$ and $\mathbf{x}_i$ denote the ith compensation vector, pulse echo measurement and pulse-echo estimate measurement respectively. They are defined as follows:

$$\mathbf{y_i} = \begin{bmatrix} y_i(\omega_1) \\ y_i(\omega_2) \\ \vdots \\ y_i(\omega_M) \end{bmatrix} \quad \mathbf{x_i} = \begin{bmatrix} x_i(\omega_1) \\ x_i(\omega_2) \\ \vdots \\ x_i(\omega_M) \end{bmatrix} \quad \mathbf{c_i} = \begin{bmatrix} c_i(\omega_1) \\ c_i(\omega_2) \\ \vdots \\ c_i(\omega_M) \end{bmatrix} \tag{62}$$

Then the computed $\mathbf{c_i}$ is applied to all the pulse-echo estimate measurements in the set of measurements and a similar error to equation (44) is computed:

$$Error = \left\| \frac{\mathbf{y_j}}{\|\mathbf{y_j}\|_2} - \frac{\mathbf{x_j c_i}}{\|\mathbf{x_j c_i}\|_2} \right\|_2 \tag{63}$$

Where $\mathbf{y_j}$ is the jth pulse echo measurement, $\mathbf{x_j}$ is the jth pulse-echo estimate measurement and $\mathbf{c_i}$ is the compensation vector computed using the ith measurement. The result of this computation is shown below:

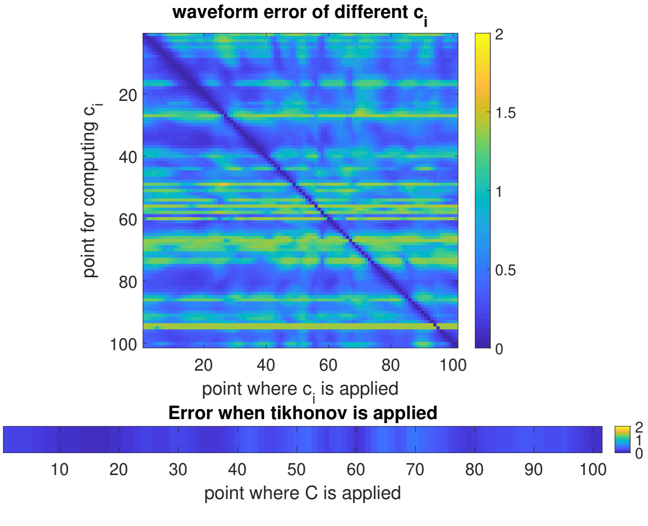

Figure 36: Top, the result of equation 63. Bottem, result of equation 63 with Tikhonov $\mathbf{c}$, as computed in Chapter 3, instead of $\mathbf{c_i}$

The right image of figure 36 contains only one error line but has been stretched to make a more visually appealing comparison to the $\mathbf{c_i}$. It is clear that some measurement points give a better compensation vector then others, the question is of course why? Below the left error plot is repeated but added to it are the frequency and phase component of the vector $\mathbf{c_i}$.

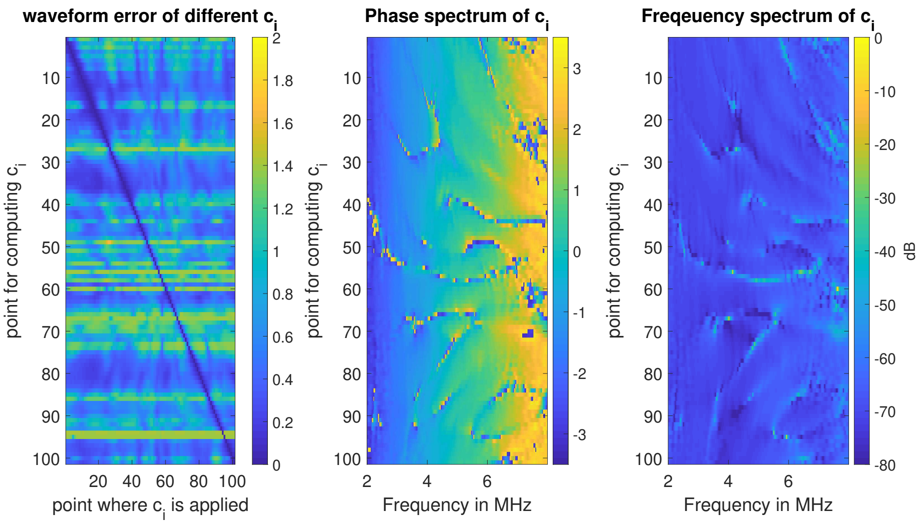

Figure 37: Error, Phase and Frequency spectrum of the $\mathbf{c_i}$'s

From this image it is clear that those single point computed compensation vectors $\mathbf{c_i}$ that have a smooth phase and spectrum result in a better compensation. Further supporting the notion that the compensation vector $\mathbf{c}$ is indeed compensating for a consistent error.

4.2 Improving single point compensation vector

In the previous section it became more likely that the error across the measurement points is a structural one and that certain points can even approximate the compensation vector $\mathbf{c}$ quite nicely. Therefor in this section it will be attempted to extract the compensation vector $\mathbf{c}$ from 1 single measurement point or at the very least obtain a good approximation.

4.2.1 Analysis of the deviation

To properly understand why certain points result in a mediocre to bad correction vector, one such point is highlighted below:

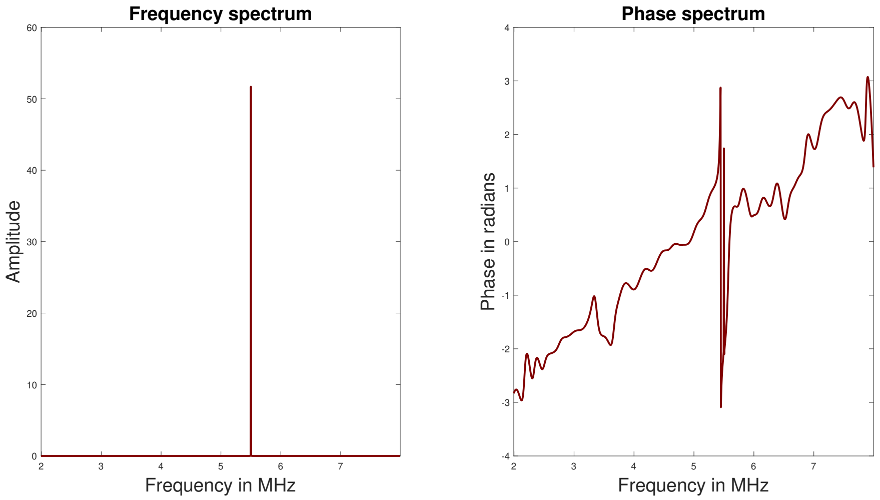

Figure 38: Example of a bad $\mathbf{c_i}$. On the left the Frequency spectrum, on the right the Phase spectrum

From the representation of the correction vector at this specific point it is evident that there is a large peak at one point in the frequency spectrum and a discontinuity in the phase spectrum. Zooming in to the frequency domain to understand the waveform better gives us:

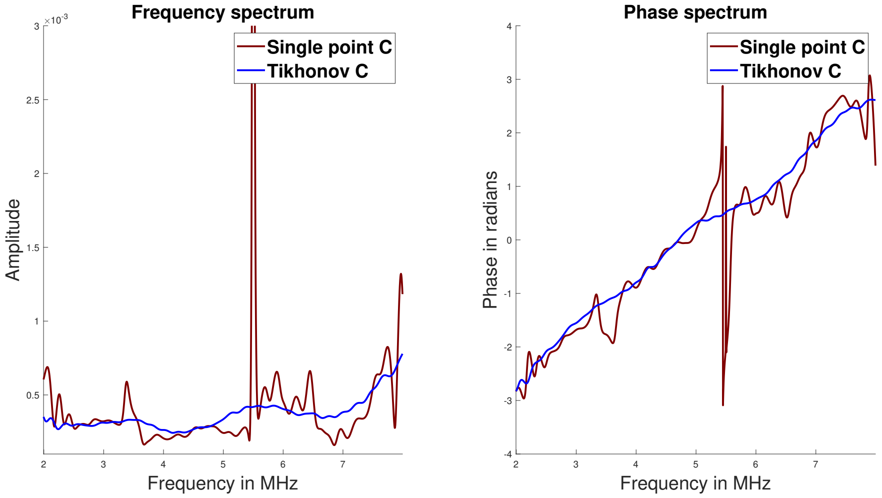

Figure 39: Comparison of a bad $\mathbf{c_i}$ and $\mathbf{c}$. On the left the Freqeuncy spectrum, on te right the Phase spectrum

It clearly shows that the $\mathbf{c_i}$ computed at one single point contains quite some more higher frequency components than the one obtained by using the proposed calibration technique on the complete set.

4.2.2 Practical solution

From the analysis it is clear that 2 problems have to be solved. First, the outliers need to be removed, and secondly the higher order components in the signal need to be suppressed. Therefore, the following method is proposed to compute a proper calibration vector from a single measurement point:

$$\underset{\mathbf{o},\mathbf{d}}{\text{minimize}} \quad ||(\frac{\mathbf{y}}{\mathbf{x}} - \mathbf{o}) - \mathbf{B}\mathbf{d}||_2^2 + \lambda_1||\mathbf{d}||_2^2 + \lambda_2||\mathbf{o}||_1 \tag{64}$$

Where $\mathbf{y}$ and $\mathbf{x}$ are respectively the pulse echo measurement and pulse-echo estimate measurement of the measurement point i, $\mathbf{o}$ is a vector of the same size as $\mathbf{y}$ and $\mathbf{x}$ that will compensate for the outliers and $\mathbf{d}$ is the selection vector of the base vectors that are in $\mathbf{B}$. $\mathbf{B}$ consist of the first 10 Fourier base vectors to ensure that the found solution is a low frequency signal and therefore, filters out the higher frequency noise effects. The λ_1 and λ_2 are found by scanning over many different values for these, ranging from 10^{-10} to 10^{20} with a set size of 1 order per step. The solution to this minimization problem was computed using CVX [8][9].The result of applying this new way of computing the calibration point is shown below:

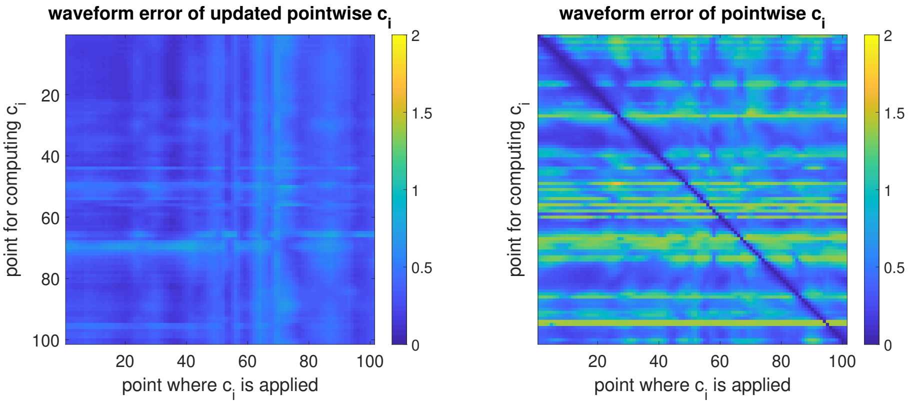

Figure 40: Left, the error of the updated single point estimate. Right, the old single point estimate as present in fig. 36

From this image is clear that the updated algorithm is able to achieve a significantly better correction vector $\mathbf{c_i}$ than the previously used algorithm. Unfortunately it is not possible to achieve as good a compensation vector as with the proposed method in chapter 3.6 on the complete data set of 101 points.

5 Simulations

Up till this point the work done has been to improve the model **A** and reduce the errors that where introduced in the model through the measurement setup. However due to the weak reflections and multiple scattering a plethora of error sources can cause significant degradation of the image quality. With the eyes towards the future an analysis of other sources of possible error are investigated using simulations. The chosen simulation toolbox is K-wave [10], a Matlab toolbox that solves the wave equation at each point to simulate the acoustic wave. THe following questions will be examined in this chapter:

- How well can we image in the ideal case?
- What is the impact of the found error on the image in a controlled environment?
- What is the is the impact of position errors?
- What is the impact of noise?
- What is the impact of mismatch in background speed?
- What is the impact of the error found in this Thesis?

5.1 Ideal case Imaging

Starting the simulation is a exploration of the best possible result that can be obtained, this will serve as a benchmark to compare all the other results to.

5.1.1 The simulation setup

To research the questions that are posted at the start of this chapter, the following simulation has be created and will be used to examine all the various questions that are posted:

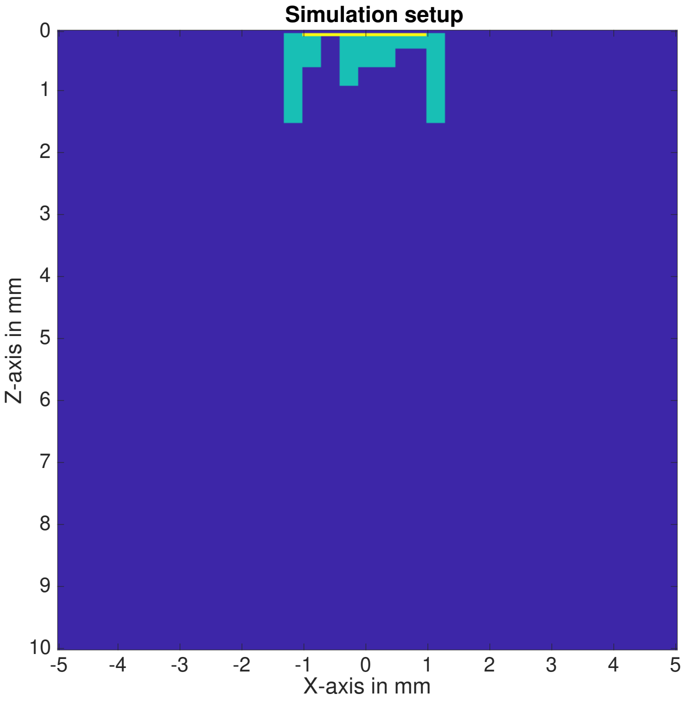

Figure 41: Simulation setup

The light green represents the mask, the bright green represents the source and the blue background is the background medium. The acoustic parameters of each part of the simulation are:

1. The mask
    (a) The speed of sound is 2730.

    (b) The density is 1180.
    (c) Max height of the mask is 1,5mm
    (d) Width of a single block is 0.3mm

2. The source
    (a) The source frequency is 5MHz.
    (b) The source pressure is 2Pa.
    (c) The source width is 2 mm.

3. The background medium
    (a) The speed of sound is 1498.
    (b) The density is 997.
    (c) The total domain is 10mm by 10mm

4. The simulation remaining parameters
    (a) Voxel size is 0.05mm.
    (b) Amount of grid points are 200x200.
    (c) Translation steps are 0.05mm.
    (d) Translation start at the most left side and move all the way to the most right side.

The simulations themselves consisted of 3 separate simulations that were used to construct the image. First a base line measurement($\mathbf{b_{ase}}$) was preformed to obtain the noise and background signal measured by the transducer without any object. Secondly the forward field of the image domain was recorded and auto-convolved to obtain the model. And finally the pulse echo($\mathbf{p_{object}}$) of the object was recorded where the object was placed within the image domain, contrary to the other measurements. These measurements where preformed for each translation which consisted of a total of 148 translations.
The measured pulse echo signal has to be processed in the following manner before imaging can be preformed:

$$\mathbf{y} = (\mathbf{p_{object}} - \mathbf{b_{ase}}) * \mathbf{S_{ignal}} \tag{65}$$

Where $\mathbf{S_{ignal}}$ is the transmitted signal itself (see Appendix A) and the imaging is preformed as described in Chapter 3.5.

5.1.2 Point Spread Function

First up we will try and ascertain the point spread function that is achievable with this imaging setup. Given the unique nature of this approach it will be compared with the results of the setup with out a mask. The result of both cases are shown below:

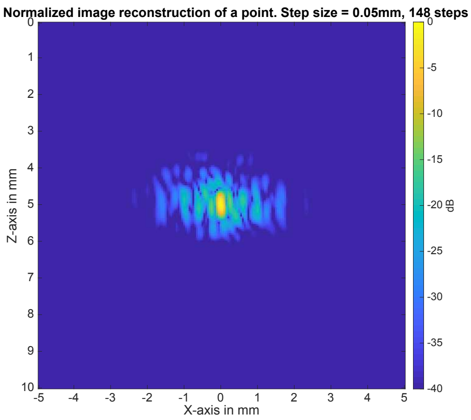

Figure 42: Point spread function with mask

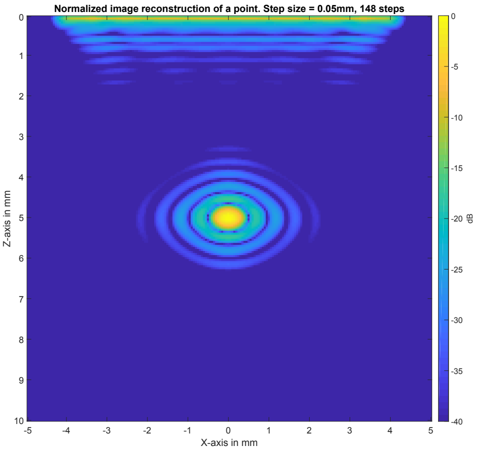

Figure 43: Point spread function without mask

From these images it is clear that the point spread function of the mask case is significantly smaller in the X direction compared to the case without a mask. At the same time it seems that there has been a slight trade-off in the Z direction. To better understand the change in point spread function the auto correlation coefficients matrix has been computed. Due to the fact that the image is in 2D and with the added time axis becomes a 3D problem, the auto correlation coefficients have been computed over one axis and averaged out as shown below:

$$\begin{gathered}\rho(X,X) = \frac{1}{N}\sum_{z=1}^{N} \frac{cov(A(z,:,:),A(z,:,:))}{2\sigma_{A(z,:,:)}} \quad \rightarrow \quad corr(x) = \begin{bmatrix} 1 & \rho(X,X) \\ \rho(X,X) & 1 \end{bmatrix} \\ \rho(Z,Z) = \frac{1}{N}\sum_{x=1}^{N} \frac{cov(A(:,x,:),A(:,x,:))}{2\sigma_{A(:,x,:)}} \quad \rightarrow \quad corr(z) = \begin{bmatrix} 1 & \rho(Z,Z) \\ \rho(Z,Z) & 1 \end{bmatrix}\end{gathered} \tag{66}$$

Where the third axis is the time axis, the index of the second spatial axis is denoted by the relevant axis variable z and x respectively. The result of these computations is shown below:

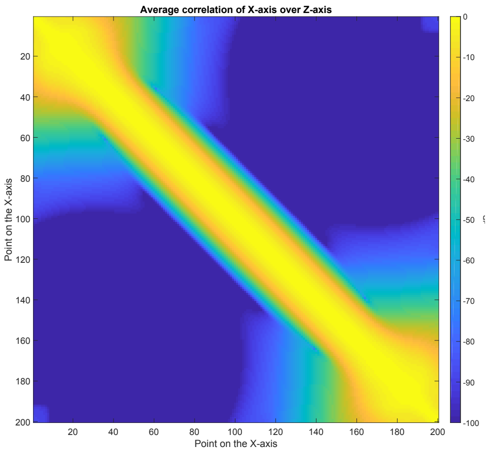

Figure 44: Correlation of the x axis for the no mask case

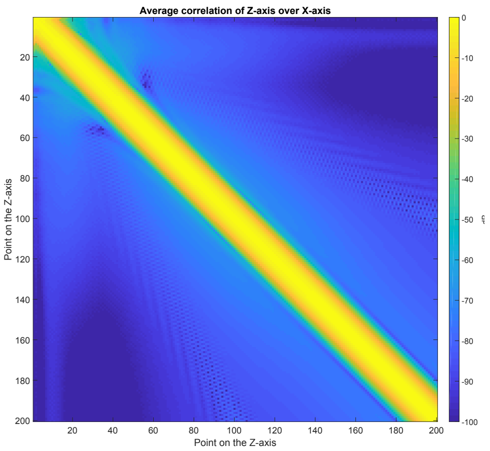

Figure 45: Correlation of the z axis for the no mask case

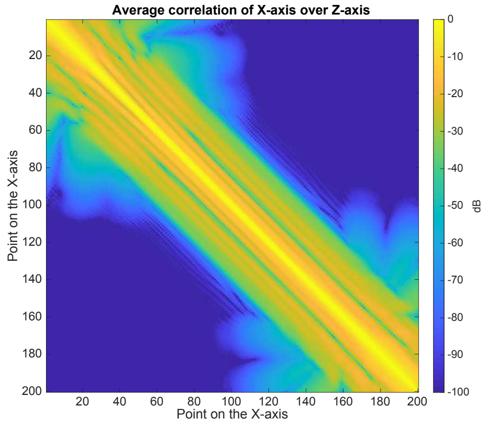

Figure 46: Correlation of the x axis for the mask case

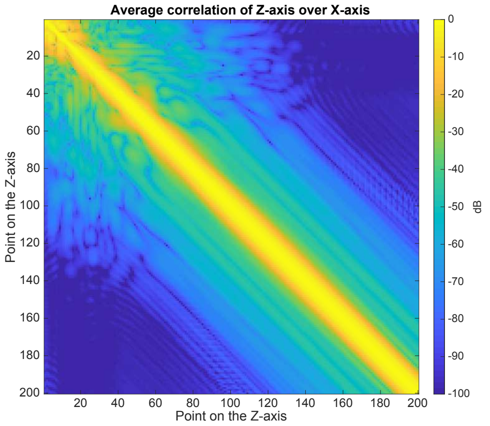

Figure 47: Correlation of the z axis for the mask case

From these results it is clear that the correlation between points is significantly smaller for the x direction and at the same time we see the occurrence of slightly more correlation in the direction of depth. Clearly showing the trade-off made by employing the mask.

5.1.3 Image Phantom

Having examined the point spread function to create an understanding of the possibilities with this mask and the resolution, a phantom is chosen to examine the imaging quality.

Given the main focus of obtaining successful imaging of biological tissue the chosen phantom is a cyst, as shown below:

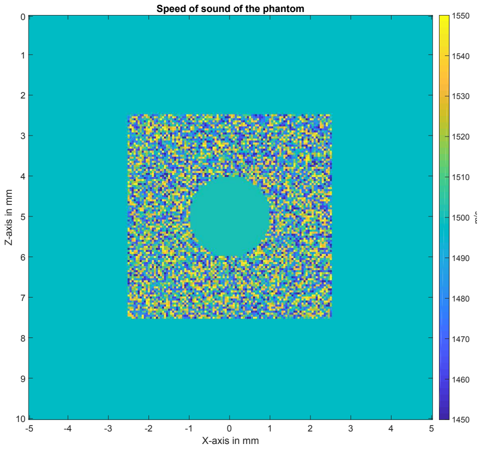

Figure 48: Sound speed distribution of the cyst

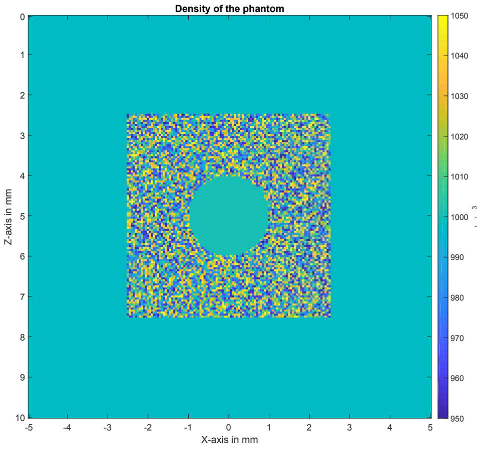

Figure 49: Density distribution of the cyst

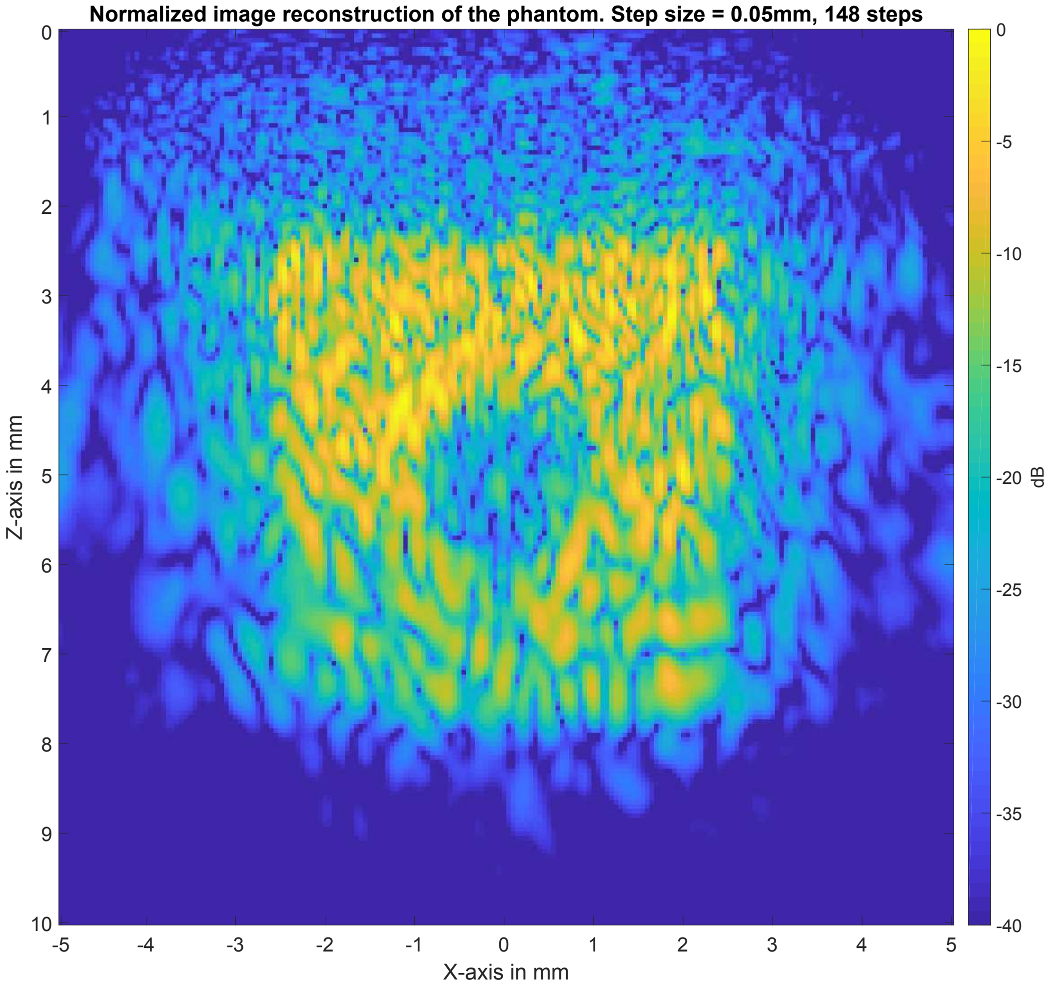

Figure 50: Error less reconstruction

The resulting reconstructed cyst clearly suffers from speckle noise. Furthermore, the edges of the cysts are very weakly defined which was expected given the point spread function obtain. To quantify this result and have a numerical way of comparing it to the errors the

the Contrast and the Contrast to Noise Ratio of the image are computed by:

$$Contrast = -20log10(\frac{\mu_L}{\mu_B}) \tag{67}$$

$$CNR = 20log10(\frac{|\mu_L - \mu_B|}{\sqrt{\sigma_L^2 + \sigma_B^2}}) \tag{68}$$

Where μ_L and σ_L^2 are the mean and variance inside the cysts respectively and μ_B and σ_B^2 are the mean and variance of the tissue surrounding the cyst. Applying this to our images results in:

Contrast	8.6774
CNR	-0.54469

Table 2: Baseline Contrast and CNR values

5.2 Systematic error

In the earlier chapters of this thesis a systematic error was found that most likely stopped the successful imaging of biological tissue. In this set of simulation we will introduce such an error into the measurement setup and examine the impact it has on the image quality and apply our calibration methodology to demonstrate the improvement that it offers. The chosen error is as follows:

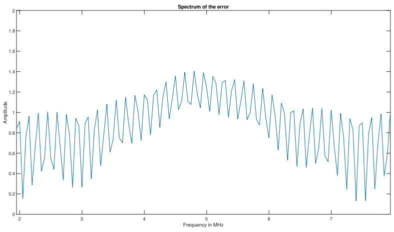

Figure 51: Frequency spectrum of the chosen error

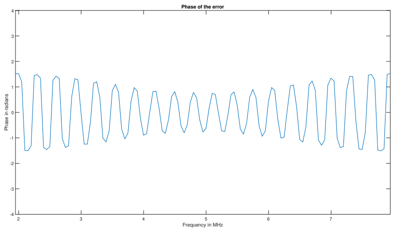

Figure 52: Phase spectrum of the chosen error

The resulting image with and withour calibration are shown below.

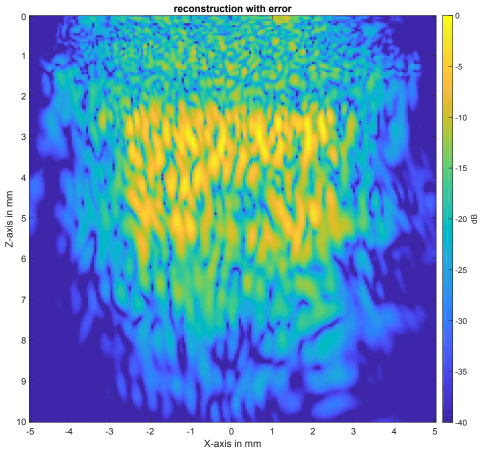

Figure 53: Imaging with error

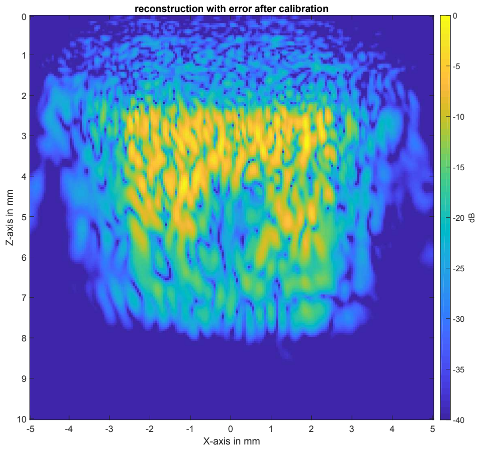

Figure 54: Imaging after applying tikhonov calibration

Clearly showing that our method is able to compensate adequately for a introduced error of the prescribed shape. The contrast and CNR are given below:

Error	With error	after calibration
Contrast	2.6385	7.1274
CNR	-9.6982	-2.9619

Table 3: ASA, Contrast and CNR values

Further sustaining the notion that the calibration works but similarly to the results of chapter 3.4, it is not a perfect reconstruction but a close approximation.

5.3 Positioning error

Given the fact that the model is constructed from practical measurements its of interest to examine the impact of the finite accuracy of the positioning system that is used in obtaining these measurements. To examine the effect the following simulation has been created.

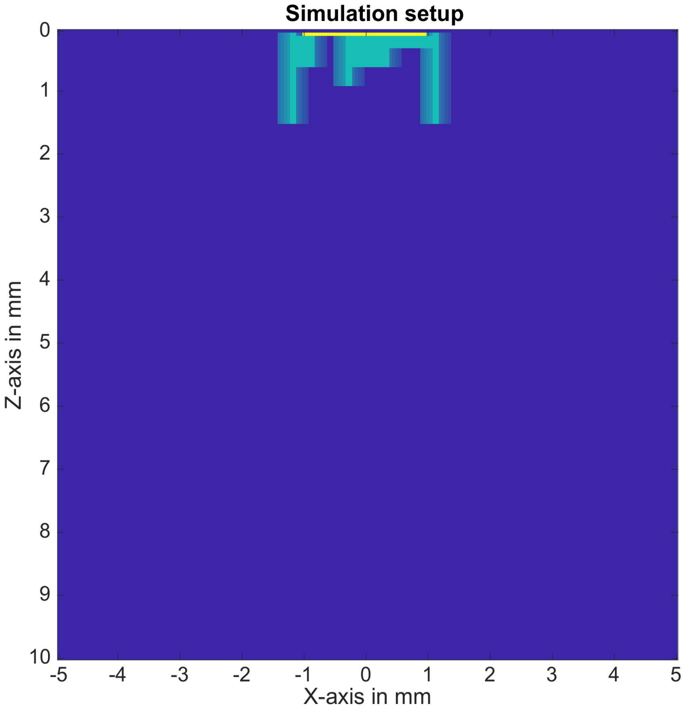

Figure 55: Positioning error

Here some of the measurements in $\mathbf{y}$ have been replaced with the ones of its neighbour to emulate a positioning error.The deviations for the positioning errors have been drawn from a uniform distributed discrete variable and the distribution is shown below:

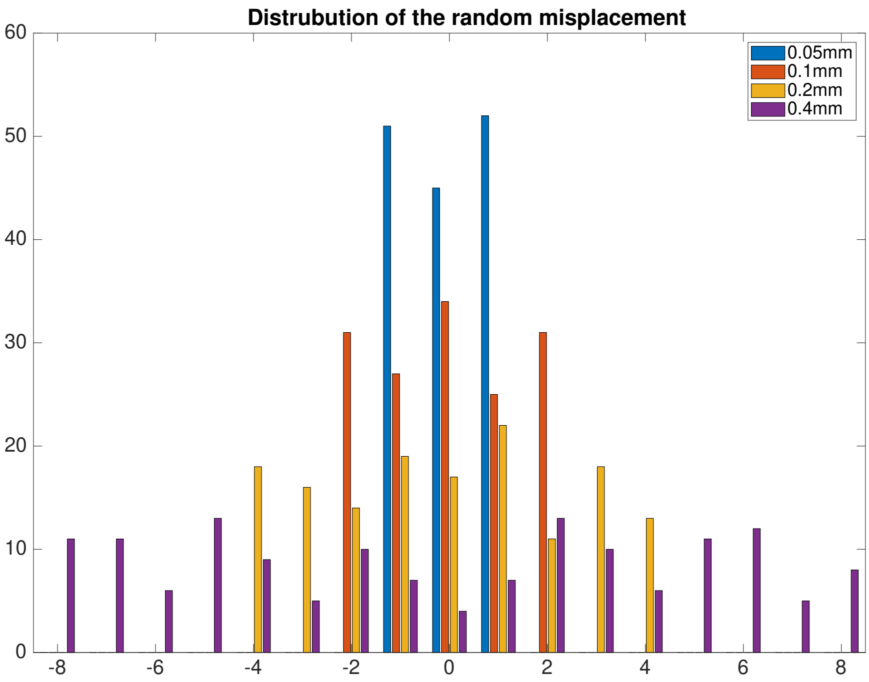

Figure 56: Distribution of the positioning error

The result of this experiment is shown below:

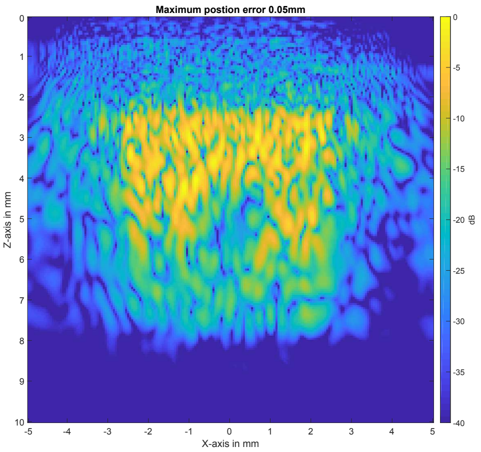

Figure 57: Reconstruction of the cyst with 0.05mm positioning error

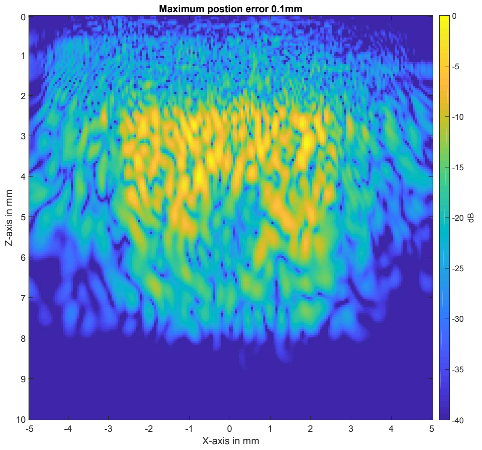

Figure 58: Reconstruction of the cyst with 0.1mm positioning error

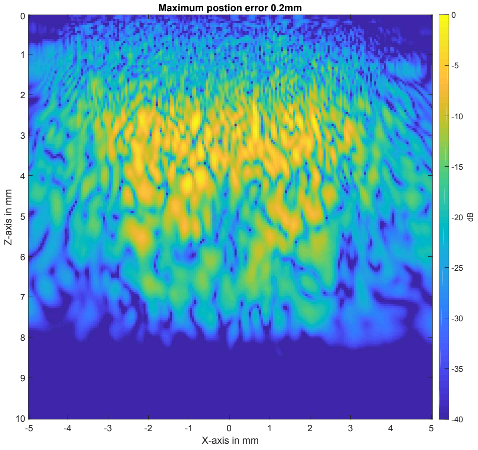

Figure 59: Reconstruction of the cyst with 0.2mm positioning error

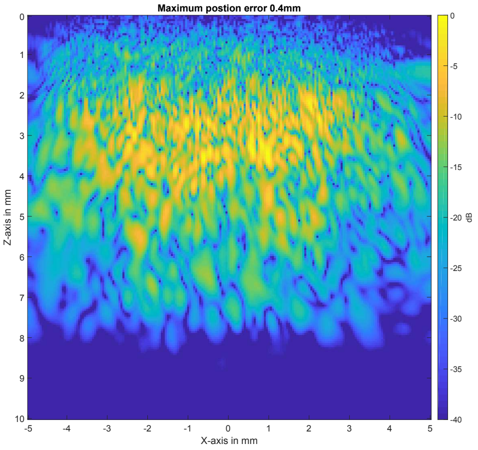

Figure 60: Reconstruction of the cyst with 0.4mm positioning error

As can be seen, a small error does not effect the results too much but when a larger error is introduced the quality of the reconstruction quickly fades. This is further evident when looking at the contrast and CNR:

Error	0.05mm	0.1mm	0.2mm	0.4mm
Contrast	6.7839	6.1505	3.4437	1.4453
CNR	-3.3042	-3.5322	-8.3814	-15.4375

Table 4: Positioning error, Contrast and CNR values

5.4 Noise

Given the weak reflections it is of paramount importance to examine the impact of noise on the resulting images. In the ideal case we have established the results for a noiseless case, now we will add white zero mean Gaussian noise to both the model and the signal itself. The added noise will represent the noise generated by the environment and the measurement equipment that is present during the creation of the model or when measuring pulse echo signals.The results of this experiment are as follows:

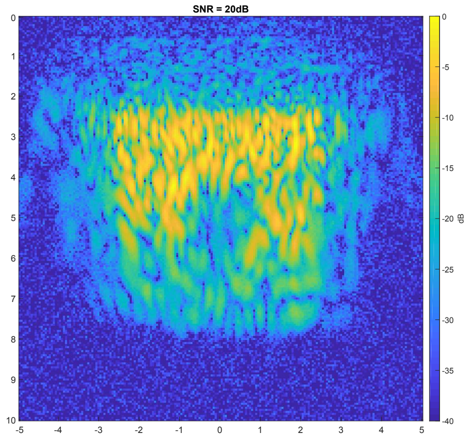

Figure 61: Reconstruction of the cyst with 20dB SNR

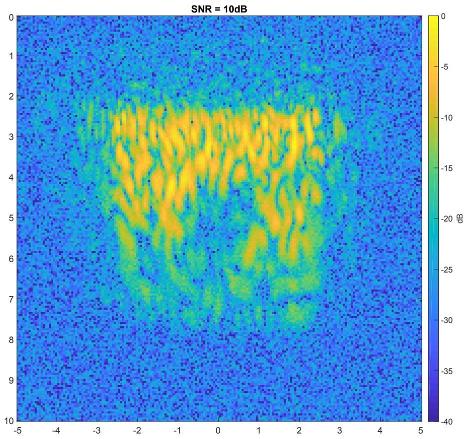

Figure 62: Reconstruction of the cyst with 10dB SNR

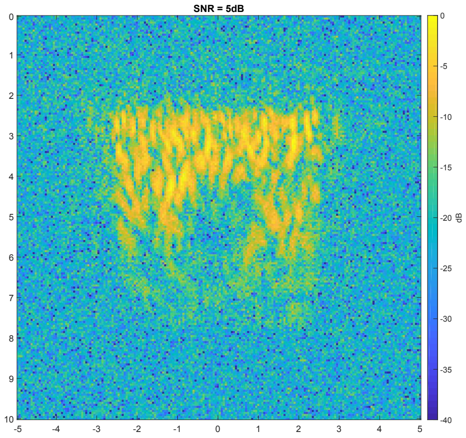

Figure 63: Reconstruction of the cyst with 5dB SNR

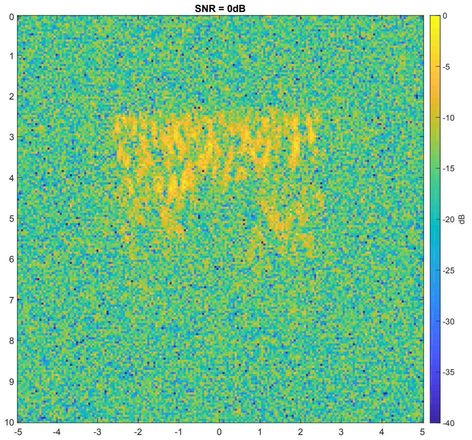

Figure 64: Reconstruction of the cyst with 0dB SNR

a decent level of SNR is required to be able to reconstruct the phantom. This was expected due to the weak reflection which generate the signal. It is advised to at least obtain a 10dB SNR or otherwise reconstruction will prove to be extreme difficult. Computing the Contrast and CNR to quantify this results in:

Error	20dB	10dB	5dB	0dB
Contrast	7.0106	6.6629	5.329	2.5808
CNR	-3.1237	-3.3321	-4.4473	-8.836

Table 5: Noise error, Contrast and CNR values

5.5 Background speed error

In these simulations and in the practical measurements the background speed has been water. The reason for this is that it is easy to fill a water tank and preform measurements which is harder with blood. Given the close proximity of both liquids with regards to speed of sound it is always assumed that water is a good substitute. Here we will examine the impact that creating a model **A** at a lower background speed of sound has on the image quality when the pulse echo is measured at a higher speed of sound. The phantom will scale with the increase of background speed to create a fair comparison due to not changing the innate contrast.

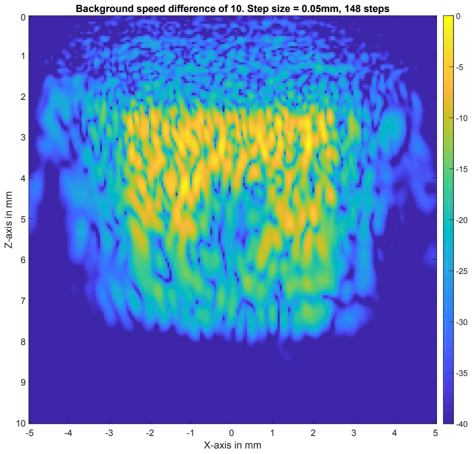

Figure 65: Reconstruction of the cyst background mismatch of 10 m/s

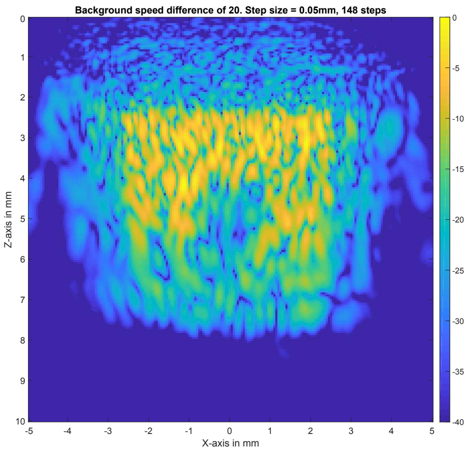

Figure 66: Reconstruction of the cyst background mismatch of 20 m/s

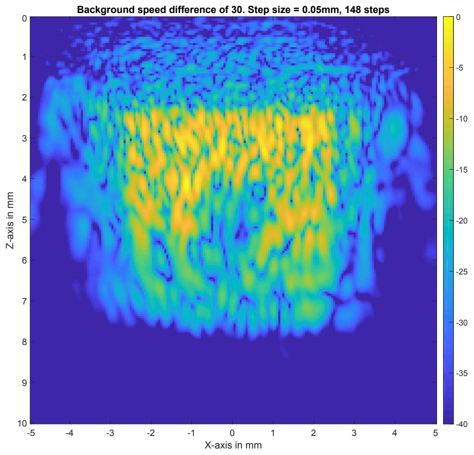

Figure 67: Reconstruction of the cyst background mismatch of 30 m/s

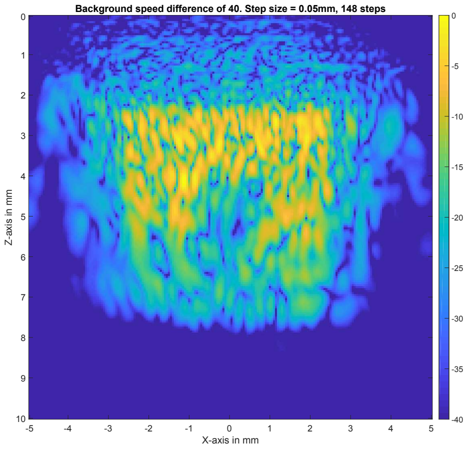

Figure 68: Reconstruction of the cyst background mismatch of 40 m/s

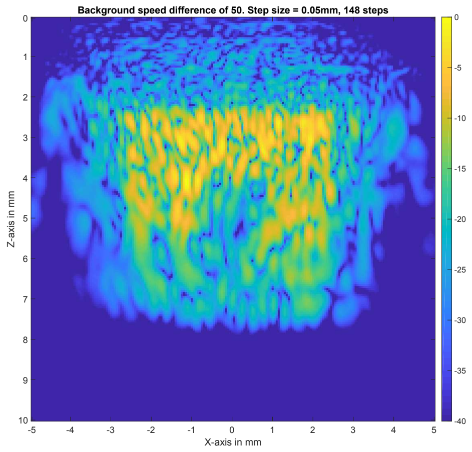

Figure 69: Reconstruction of the cyst background mismatch of 50 m/s

The largest and most interesting error we observer here is that a large part of the introduced error is focusing on the location of the mask. Furthermore we see a marginal decay of the quality of the phantom. To quantify the results the Contrast and CNR are computed.

Error	10m/s	20m/s	30m/s	40m/s	50m/s
Contrast	6.9887	6.7649	6.4933	6.2018	5.9166
CNR	-3.0383	-3.2253	-3.5051	-3.8405	-4.2029

Table 6: Background speed error, Contrast and CNR values

As expected, both the Contrast and the CNR values decay with the mismatch. But it must be stated that it is rather small compared to the other errors.

5.6 Realistic Image

Having examined the separate sources of image degradation we will now perform a realistic simulation with all the errors described above. The following values for the variety of sources were used:

1. 20dB SNR
2. 0.1 mm positioning error
3. 50 m/s speed of sound difference
4. systematic error as described in section 5.2

These values where chosen based on the authors believe that these would mimic a real simulation environment the best. The 20dB SNR is chosen because of the controlled nature of the experiments, the positioning error is chosen to be below one wavelength, the speed of sound difference is due to the know difference between water and blood and finally the systematic error is chosen to show how well the system functions with such a complex error. The imaging results are as follows:

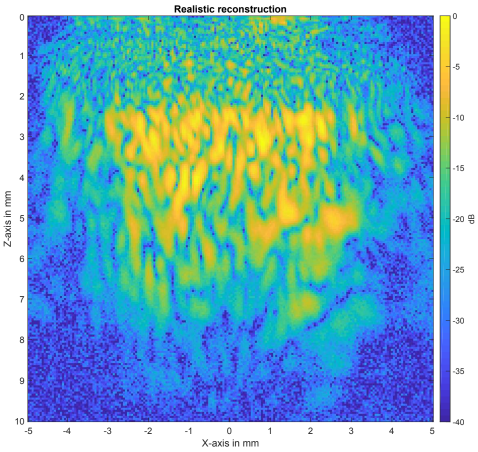

Figure 70: Realistic error of 20dB SNR, 0.05mm position error, 50 m/s speed of sound mismatch before calibration

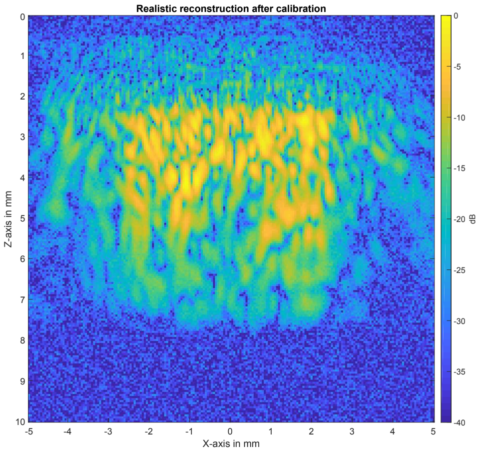

Figure 71: Realistic error of 20dB SNR, 0.1mm position error and 50 m/s speed of sound mismatch after calibration

Its clear from these images that we cannot perfectly reconstruct our old image back but the calibration is able to return to a semblance of a image that was lost in the scenario before the calibration. The resulting Contrast and SNR values confirm it:

Error	before calibration	after calibration
Contrast	2.8652	4.122
CNR	-8.9623	-6.4816

Table 7: Realistic Image experiment, Contrast and CNR values

Concluding that based on the techniques and methods presented in this thesis it should be possible to achieve imaging of biological tissue after calibration.

6 Discussion and Conclusion

This thesis started with the derivation of the theoretical model on which the proposed method of [1] is based. To solve the inverse imaging problem the first order born approximation was applied to arrive at the final model. The first order born approximation states that the total field can be replaced by the incident field when the reflected field is relatively weak compared to the incident field. Given that in the case of tissue imaging the speed of sound is around 1550 m/s and water is around 1500 m/s, which means a similar acoustic impedance, the reflection coefficient will be small and therefore the reflected field will be weak. Therefore, it is a reasonable assumption that it will have minimal to no impact on the result.

After having ascertained a model **A** based on reasonable assumptions a examination was made of the measurement setup that fill the columns of this model **A**. It was clear from the investigation that the signals that made up the columns of **A** are a representation of more then just the Green's function and the incident wave as derived in the theoretical model. Various devices necessary for the capturing of the signal contributed through their own transfer function to the signal and there possible impact was exacerbated by the use of the auto-convolution to estimate the pulse echo signal. The components that where identified to possibly have a unwanted contribution where: The hydrophone, the amplifier, the transducer excitation signal, the transmit function of the transducer, the mask and the medium. Furthermore, the pulse echo measurement contained additional components that where not present in the hydrophone measurement setup namely: the reflection of the wave, the medium after reflection, the effect of the mask after reflection, the receive function of the transducer and the effect of a different amplifier.

After comparing the measured signals it was clear that there was a difference between the 2 set of measurements, in the time domain it became evident that there was a time shift, a inversion and a scaling difference. The inversion is easily explained by the fact that the concolved forward wave didn't change its direction of propagation and therefore didn't change sign. The time delay and the scaling are, at the present, not attributable to a specific source. The delay is around 100ns which means the original delay was 50ns and got doubled by the autoconvolution and which means that it possible travelled 75 micrometers more in the water tank. The possible source of these delays can be either the amplifiers, the hydrophone or the transducer. The mask and the medium are excluded as a possible source for the delay due to the reciprocity principle of these 2 and the transducer excitation signal could account for the scaling but not the delay. The delays can possibly be due to the throughput speed difference between the 2 amplifiers, given the weak signals that are measured a relatively large set of amplification stages need to be used to obtain a signal as well as several filters to cancel out the noise. Each of these stages and/or filters can cause a delay but is typically of a lower order then 50ns and are designed to be wide banded as to not interfere with the signal that is amplified. The hydrophone is specifically designed to measure acoustic waves but the most forward part of the hydrophone sticks out before the membrane that measures the signal. To be responsible for the entire delay the point on which the wave in the pulse echo setup reflects should be 75 micrometers ahead of the measuring membrane which is not the case. For course the membrane is at the tip of the needle and the signal needs to travel to the end, which is not always through a a highly conductive material as copper which could cause a small delay. But given the high speed of electromagnetic wave propagation this seems unlikely to be the reason for the delay. The final possible source of the delay is the transducer itself which operates by transforming electric energy into motion. Each transducer has each own transfer function for the frequency and the phase, given that a time delay is equal to a linear phase shift in the frequency domain this could be the possible source of the difference when the transfer function from electrical to pressure is not the same as pressure to electrical. However it is at present unknown if this is the case the the measurement setup used in this thesis and given the other possible sources it is the assumption that each of the individual components attributed to this error in different measures.

Given the unknown nature of the source and after examination in the frequency domain that the error is more then a straightforward scaling and time delay in combination with the seemingly position independent nature of the possible sources of this systematic error, a method was proposed to estimate and compensate for the assumed constant error. The proposed calibration method is the Tikhonov regularized least squares approach that tries to find the least energetic solution that minimize the difference between the pulse echo signal and the pulse echo estimate. By finding the least energetic solution it forces generalisation in the solution which approximates a systematic error successfully if it exists. The result of this calibration method was applied on the the model **A** and then the calibrated model was used to preform a series of 1D imaging experiments. The results far out preformed the uncalibrated method even after time shifting the uncalibrated method to obtain a better image. The main reason for this seems to stem from the semi-linear nature of the phase shift that is in the calibration vector produced by the tikhonov method. When examining the original time signals after time shift and inversion it is clear that the signal matches perfectly in the middle but starts to drift in time at the edges of the signal. This seems to indicate that the time shift is not a consistent one, in line with the result of the calibration method. This small time drift means that to properly approximate the signal in the uncalibrated case more signals are necessary and given the spare nature of the experiments the usage of tikhonov regularized least squares to image would work disadvantageous.

Given the apparent systematic nature of the error it stands to reason to be able to obtain this compensation vector from a single measurement. Upon computing the results of a calibration vector from a single measurement it became clear that the result heavily dependent on the noise that was present in the measurement. Therefore, an adaptation of the Tikhonov regularized least squares was proposed that tries to estimate and suppress any outliers while simultaneously tries to find a low complexity polynomial that can approximate the single measurement calibration vector. The result of this method is a calibration vector that results in a 10% worse waveform match compared to the calibration vector found using all the measurements in the originally proposed calibration method. The main reason for this seems to stem from the fact that a smooth phase spectrum is paramount to obtaining a successful compensation vector, this in turn demands a low polynomial estimate of the single measurement calibration vector, this is however not able to properly estimate the frequency spectrum. The main reason for this unhelpful relation stems from the fact that both the frequency spectrum and the phase spectrum stem from both the real and imaginary part of the polynomal but in different ways. When presented with only one measurement its unable to find the right balance to tweak both the real and imaginary part for a ideal outcome.

Finally a extensive set of simulations where preformed to examine various sources of noise and measurement errors and there impact on the quality of the image. It showed that positioning errors don't effect the result much as long as its less then 1/2 of the wavelength, that sufficient SNR needs to be reached to produce a image, ideally above 20dB. Furthermore, it showed that the a difference in a background speed of sound comparable to the difference of water and tissue barely effect the quality of image reconstruction. The impact of a complex systematic error did indeed cause a large degradation in image quality but as shown before the proposed calibration method in this paper was clearly able to significantly improve the quality of the image. And finally realistic scenario was simulated to examine if the combined error created by these various error and noise sources would lead to successful or unsuccessful imaging. It is possible after calibration to obtain a image of a level of quality where the object can still be recognised.

In conclusion, there has been established that there is a difference between the pulse-echo estimates and the pulse-echo of a seemingly systematic nature. A calibration method was proposed that significantly improved upon the result of the uncalibrated model in regards to imaging. It has been shown that a close approximation of the calibration can be obtained from a single measurement using a adapted form of the original calibration method.

7 Future work

Successfully imaging depends mainly on two thing, the accuracy of the model and how well posed the imaging problem is. In this thesis a method was proposed to improve the former (accuracy of the model). The Tikhonov regularized least squares method is a rather straight forward method that attempts to solve the difference through a complex scaling of individual frequency bins in the frequency domain. This method does not take into account the possibility of interdependence's between different frequencies or the phase. The first avenue of future work should be to obtain a more detailed understanding of the individual components that make up the error. This will allow for a better understanding of the error that was found and might lead to structures or interdependence's that exist within the error that can be exploited for better calibration. Furthermore, the current method only works for a systematic error but falls short when the error is position dependant. The investigation done in this thesis has not resulted in finding a strong reason to suspect a position dependency in the error but a more detailed examination might shed some more definitive light on this subject.

The second proposed avenue for future work is rather straight forward, the continuation of this work into the 3D domain. Currently this calibration method has been successfully applied to the 1D domain and to a limited extend the 2D domain showing great promise. Extension to the 3D domain would allow for the possibility of imaging biological tissue and ultimately,

if successful, the application of this imaging and calibration method in a clinical setting.
The first 2 suggestions have been with respect to the accuracy of the model, the next two are with respect to how well posed the imaging problem is. The mask used in this thesis tries to create a scattered signal that ideally attributes a unique signal to each point is space as its reflection. Currently the hole distribution of the mask is randomly due to the absence of a better know structure or method to enable the desired effect. During the experiments in this thesis it became apparent that the mask mainly offers a improvement in the resolution in the x plan of a 2D imaging experiment consisting of a xz plane. Therefore, it is proposed that future work in regards to optimisation of the mask should focus on creating a distribution of the wave in such a manner that each point in the x-direction, and when extension to the 3D domain the xy-plane, is uniquely radiated to optimised the discernibly of coordinates in this plane. The z plane or depth is currently successfully ascertained from the time of arrival.
The final avenue of future work is to create a optimised imaging strategy. This thesis did not touch upon this subject because its focus was on improving the accuracy of the model and therefor only singular measurements where used in constructing the various images. However, by taking more measurements of the same object the amount of equations is increased which potentially leads to a better posed problem. The main requirement for these additional measurements is that they offer new information on the same object by having received reflections from the object in a new combination. If this requirements is not met then the additional measurements will only bloat the size of the computation and slow down the imaging.

References

[1] P. Kruizinga, P. van der Meulen, A. Fedjajevs, F. Mastik, G. Springeling, N. de Jong, J. G. Bosch, G. Leus, Compressive 3D ultrasound imaging using a single sensor. *Sci. Adv.* **3**, e1701423 (2017)

[2] Unknown. The top 10 causes of death. Internet: *https://www.who.int/news-room/fact-sheets/detail/the-top-10-causes-of-death.* 24 May 2018. [Jan. 08, 2019]

[3] Andrejs Fedjajevs, (2016), *Ultrasound Imaging Using a Single Element Transducer*, (Publised master thesis), TU Delft, Delft, The Netherlands

[4] J. Janjic, P. Kruizinga, P. van der Meulen, G. Springeling, F. Mastik, G. Leus, J. G. Bosch, A. F. W. van der Steen, and G. van Soest. Structured ultrasound microscopy. *Applied Physics Letters* 112, 251901 (2018).

[5] K.W.A. van Dongen, Medical Ultrasound-Physics of Ultrasound, 21-04-2019, Delft University of Technology, Department of Imaging Science and Technology

[6] J. Zimmerling, and R. Remis, Wavefield Imaging lecture notes, June, 2018 , Technische Universiteit Delft

[7] C.C. Paige, M. A. Saunders LSQR: An Algorithm for Sparse Linear Equations and Sparse Least quares. *https://stanford.edu/group/SOL/software/lsqr/lsqr-toms82a.pdf*

[8] M. Grant and S. Boyd, CVX: Matlab Software for Disciplined Convex Programming, version 2.1, *http://cvxr.com/cvx*,mar,2014

[9] M. Grant and S. Boyd, Graph implementations for nonsmooth convex programs, Recent Advances in Learning and Control, Lecture Notes in Control and Information Sciences, V. Blondel and S. Boyd and H. Kimura, Springer-Verlag Limited, 95-110, 2008, *http://stanford.edu/ boyd/graph_dcp.html*

[10] B. Treeby, B. Cox and J. Jaros k-Wave: open source acoustics toolbox for Matlab *http://www.k-wave.org/*

[11] P. van der Meulen, P. Kruizinga, J. G. Bosch, G Leus. Calibration techniques for single-sensor ultrasound imaging with a coding mask. *to be published*

[12] Strutt, J. (1896). The theory of Sound Volume II. 2nd ed. London: Macmillan and Co., Ltd., pp.273-295.

[13] M Fink. Time reversal of ultrasonic fields. I. Basic principles. *IEEE transactions on ultrasonics, ferroelectrics, and frequency control,* 39(5):555-566, 1992. ISSN 0885-3010. doi: 10.1109/58.156174.

[14] M. Fink, G. Montaldo, and M. Tanter, Time-Reversal Acoustics in Biomedical Engineering, *Annual Review of Biomedical Engineering* 2003 doi: 10.1146/annurev.bioeng.5.040202.121630

[15] M. Fink Time-reversed acoustics *Scientific American* November 1999

[16] J.A. Jensen, A model for the propagation and scattering of ultrasound in tissue *J. Acoust. Soc. Am.* ,Vol. 89, No. 1, January 1991

[17] J.A. Jensen, and N. B. Svendsen, *Calculation of Pressure Fields from Arbitrarily Shaped, Apodized, and Excited Ultrasound Transducers* J. Acoust. Soc. Am.,Vol. 89, No. 1, January1 991 *IEEE transactions on ultrasonics, ferroelectrics, and frequency control* VOL. 39. NO. 2, MARCH 1992

A Reciprocity of the Mask

One of the assumptions on which the work in this thesis is based on the reciprocity. It allows for the usage of the auto-convolution of the forward field to obtain the full field. In this appendix we will expand on the reciprocity theorem and show through the use of simulations that it holds.

A.1 The reciprocity theorem

The assumption is that the mask adheres to reciprocity theorem due to the linear nature of ultrasound at relative low levels of power. Simply put, it means that due to the linear nature the location of the observer and transmitter can be interchanged and thus that the transfer function from transmitter to reflector is the same as from reflector to transmitter. The theorem has been shown to hold in many different fields of study and has first been put to paper for ultrasound by Lord Rayleigh in his book Theory of Sound [12] where he denotes it as Helmholtz theorem. In the work of Fink et. al. [13] [14] [15] on time reversal this principle is used even in the face of a chaotic medium but with linear structural dynamics and acoustics. This theorem breaks in the case of non linearity propagation which arises when a relative large amount of energy is produced by the ultrasound sensor, the medium is non stationary or there are sources at the boundary. In our case one of the sides of the boundary is a source itself.

A.2 Simulation

Due to the large set of possible factors attributing to the difference in the signals in the practical experiment is difficult to attribute the behaviour to the lack of reciprocity specifically. Therefore, simulations where chosen as a way to isolate the phenomena and examine the question of reciprocity. The chosen simulation tool is k-wave [10] and the simulations will start from a simple case and progress to a closer approximation of reality by adding complexity.

A.2.1 Reciprocity with point sources

To clearly understand if or when reciprocity possibly breaks, the simulations start off simple and become more advanced with time till the entire scenario is completely simulated or reciprocity breaks. The procedure for measuring reciprocity is as follows:

- First simulation.
- Source 1 sends out a pulse.
- Source 2 records the pulse at its location.
- End of first simulation.

- Second simulation
- Source 2 sends out the recorded pulse.
- Source 1 records the pulse at its location.
- End of second simulation

- autoconvolve the recorded pulse at source 2 in the first simulation.
- divide both the autoconvolved signal as the recorded signal and Source 1 by there own maximum respectively.

Starting with the simplest situation, 2 points:

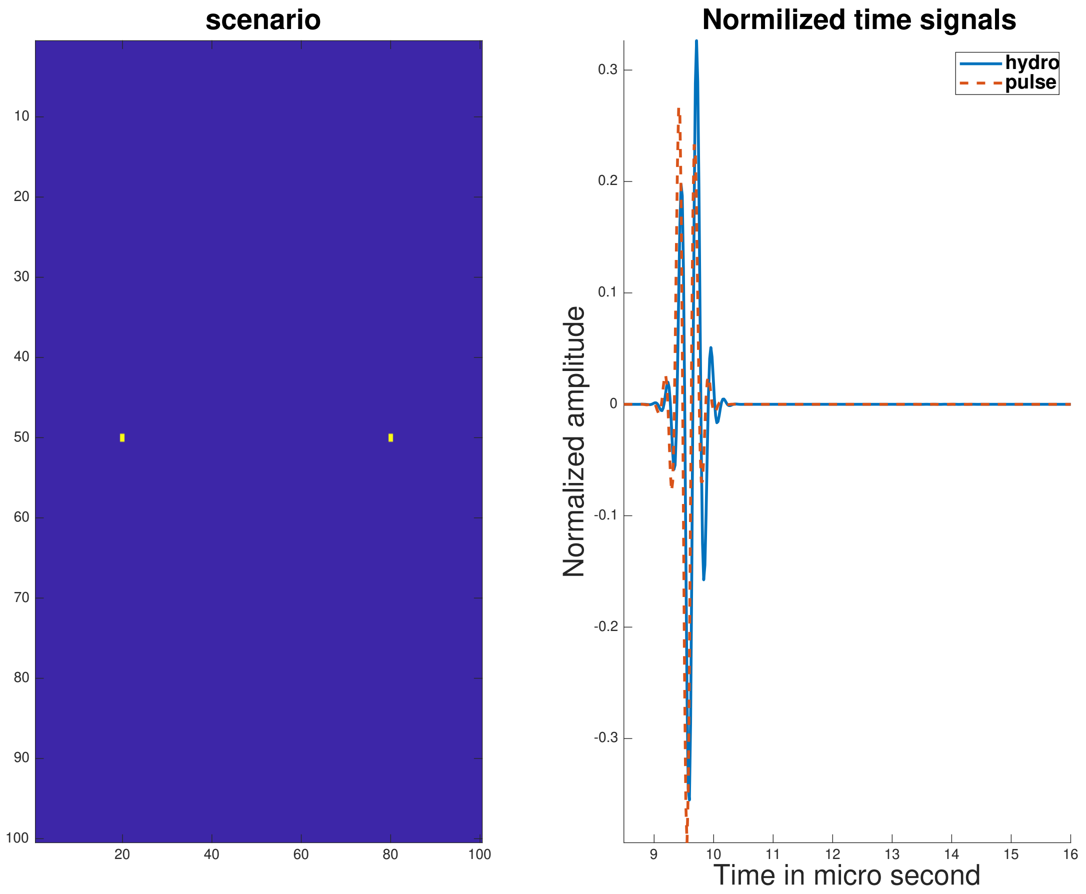

Figure 72: Reciprocity of 2 points

Directly the simulation seems to break, this is due to a oversight in our simulations. In 3.1 we identified all the different components that make up the setup, and that included the exitated pulse itself. In our simulations we are not accounting for the double contribution of the signal in the auto-convolution which is absent in the signal measured at source 1. Therefore, we need to convolve the signal at source 1 with the pulse itself to make sure if reciprocity still holds. The results of this compensation are as follows:

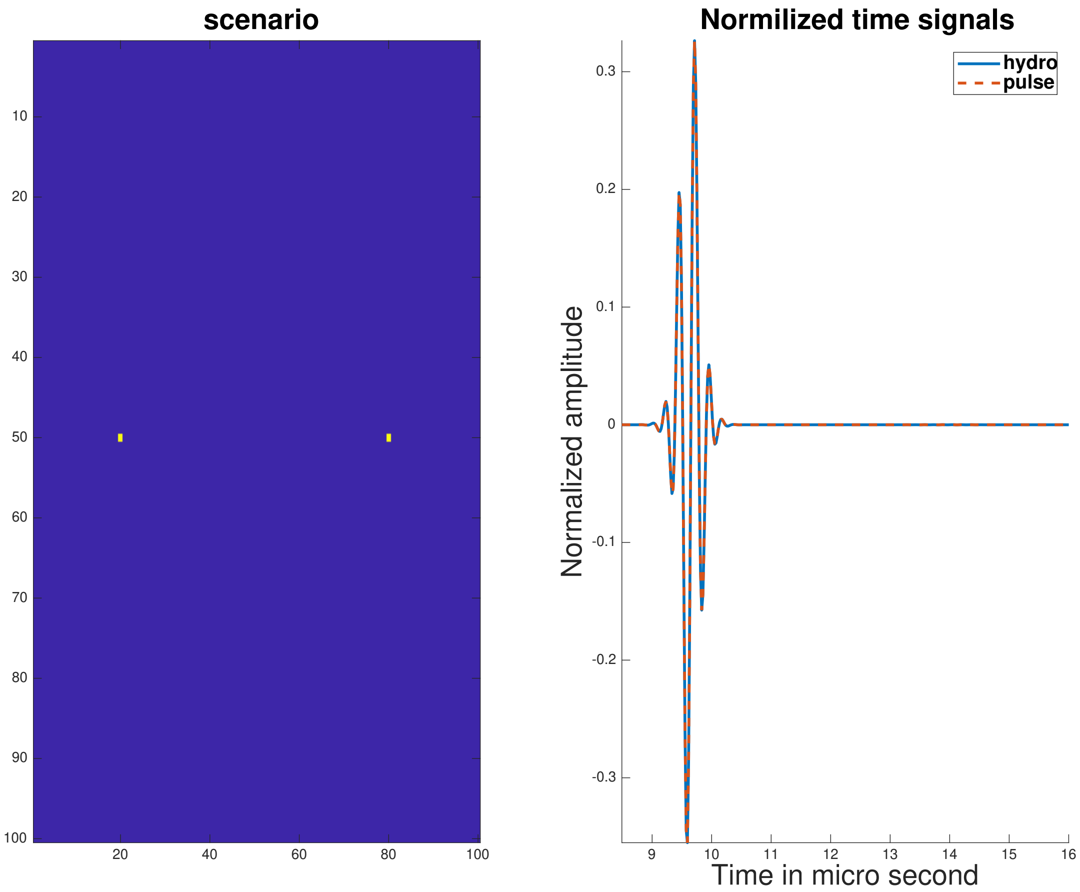

Figure 73: Updated reciprocity of 2 points

Showing that for the simple case of 2 points that the reciprocity holds. Now to further examine the effect of reciprocity a simple medium is placed between the 2 points:

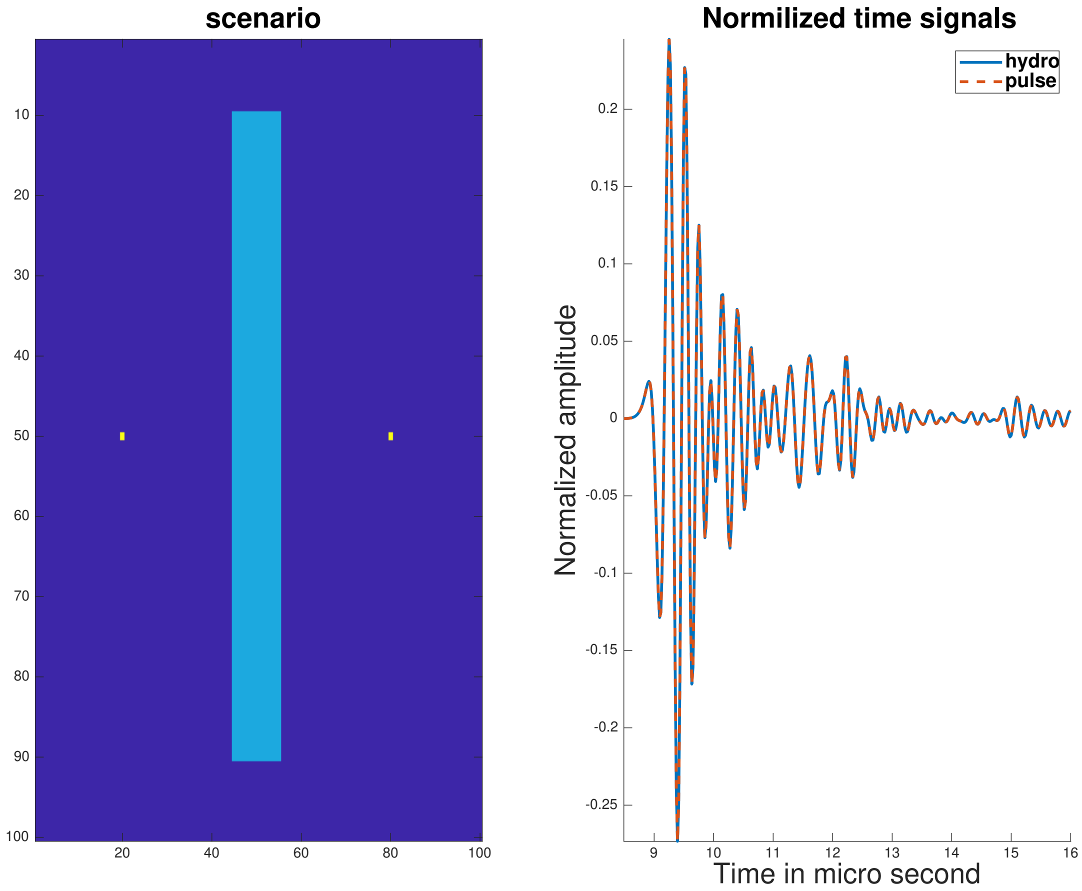

Figure 74: Reciprocity of 2 points with simple medium

Again showing that reciprocity doesn't break for such simple cases. Now to examine its effects when the medium is more complex and multiple scattering occurs the following simulation was created:

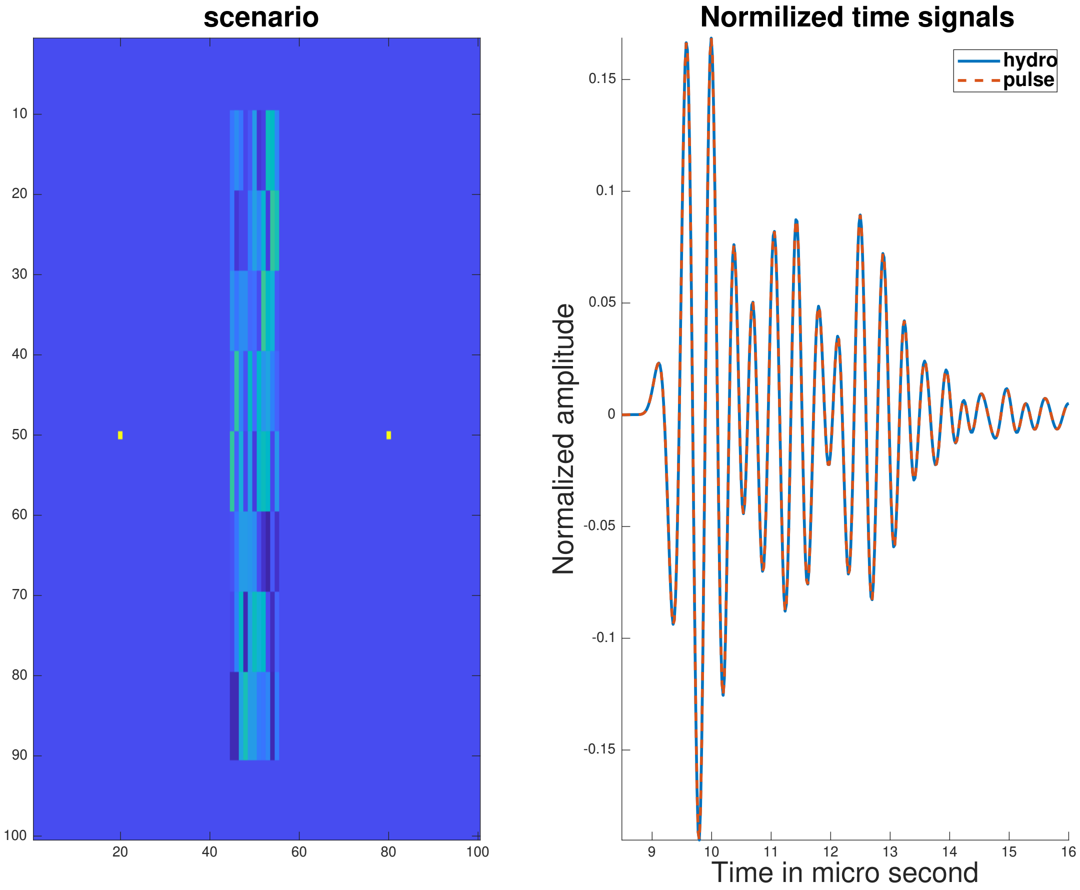

Figure 75: Reciprocity of 2 points with complex medium

Given the linear nature of ultrasound at low levels of power, reciprocity still holds even when confronted with multiple scattering.

A.2.2 Reciprocity with an element and a point source

In these simple case of 2 points it has been shown that reciprocity holds but in our case the ultrasound element is significantly larger then our point reflector. To illustrate this the previous simulation was repeated with this difference applied:

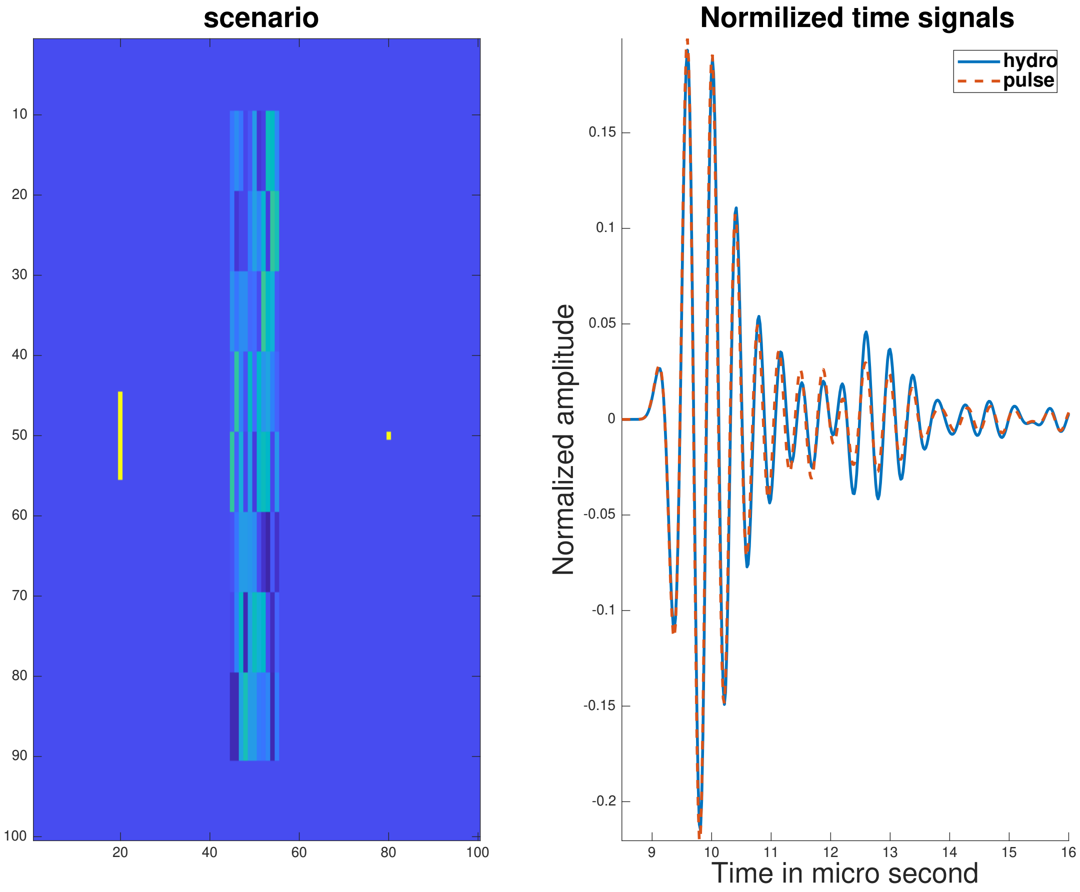

Figure 76: Reciprocity of 1 element and 1 point with a complex medium

Seemingly this is where reciprocity seems to break for the first time. However after careful examination of the simulation it was found that the grid was unable to sustain the higher frequencies that came with the multiple scattering effects as shown in the plots below:

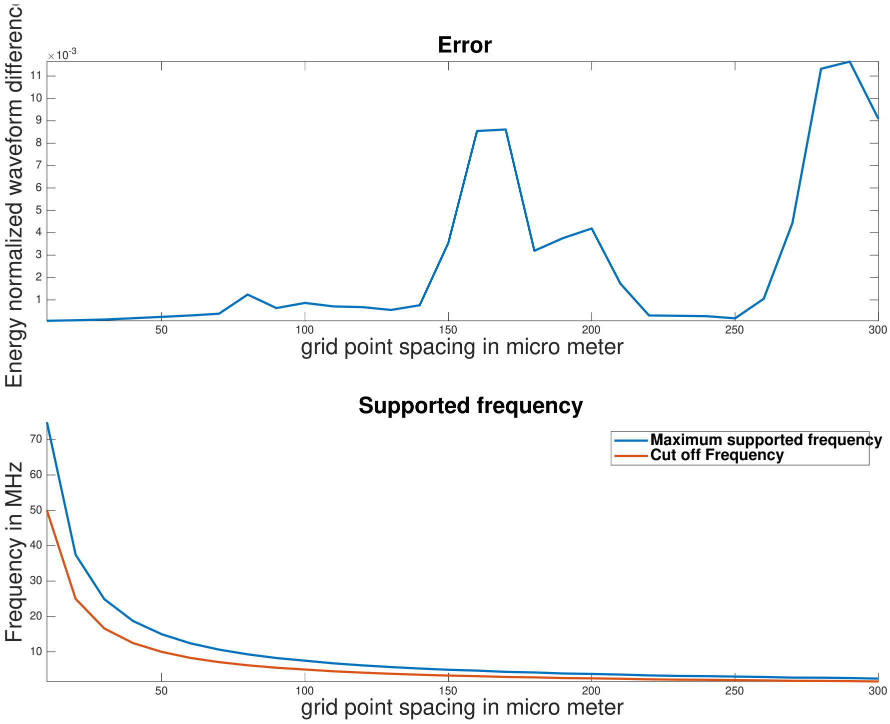

Figure 77: Relation between error and supported frequencies

The error criterion used here is the Mean Squared Error (MSE) and given by:

$$MSE = \frac{1}{n}\sum_{i=1}^{n}(Y_i - \hat{Y}_i)^2 \tag{69}$$

Where Y_i is the signal recorded at Source 1 and $\hat{Y}_i$ is the autoconvolved version of the signal that was recorded at Source 2. It shows that when the supported frequencies go up due to a finer grid the error goes down because the entire signal is now transmitted. The drop in error around 220 micrometer spacing can easily be explained by looking at the frequency spectrum of the transmitted signal.

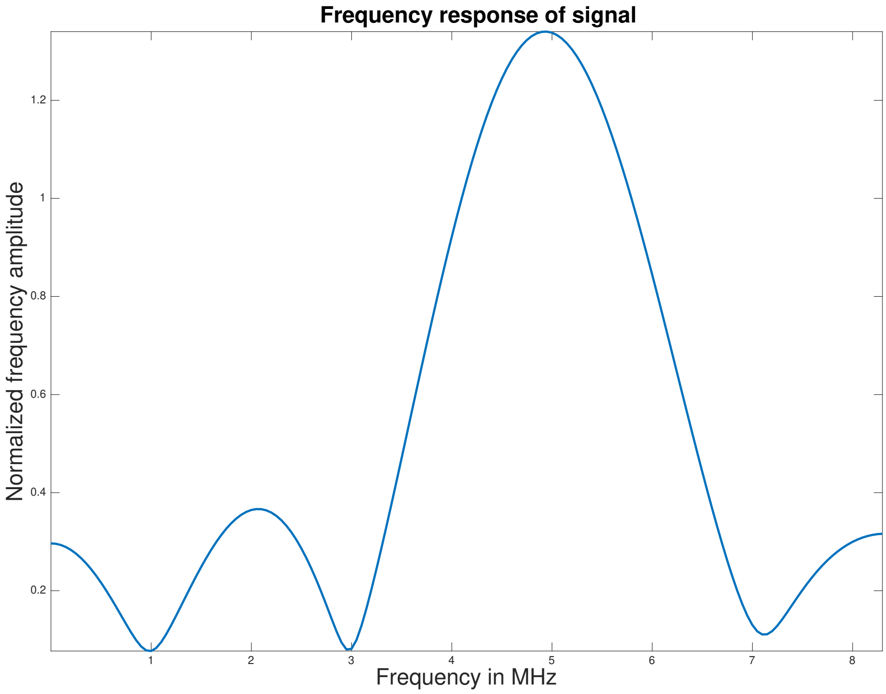

Figure 78: Freqeuency spectrum of test signal

The drop in error at the 220 micrometer mark is due to the fact that in that case the main lobe is almost completely filtered out leaving a nice symmetrical spectrum which lowers the mismatch. Equally the slight up jump of the error around the 75 micrometer mark is due to cutting off halve of the side lobe on the right side of the main lobe.
Therefore this apparent mismatch can be solved by either lowering the spacing between pixels in the simulation or allowing the signal to repeat more to create a more narrow spectrum. The former approach was used in the remainder of the simulations.

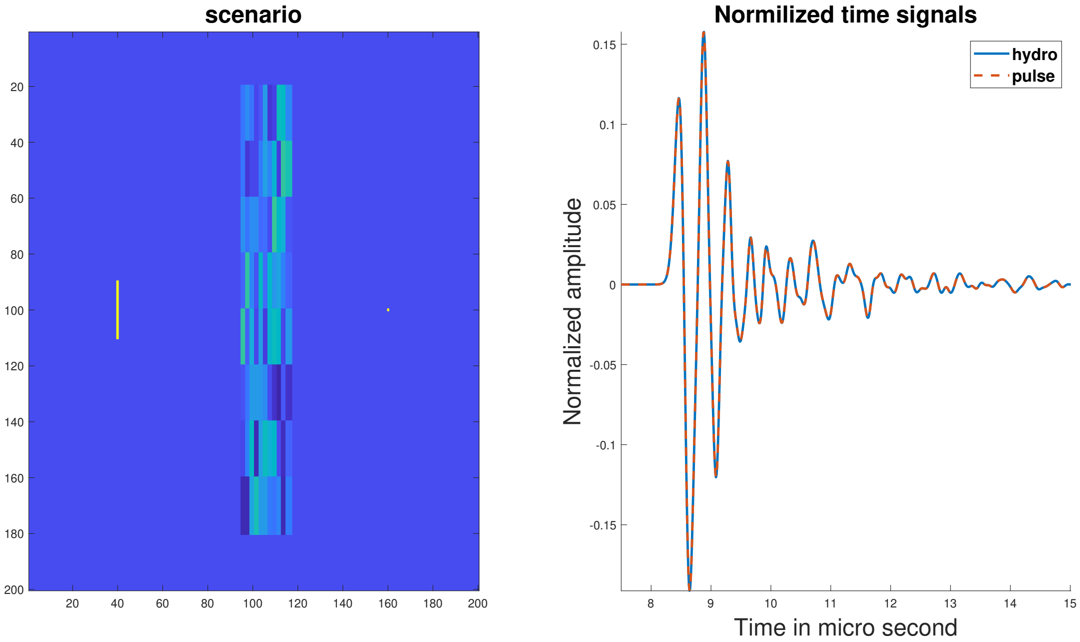

Figure 79: Updated reciprocity of 1 element and 1 point with a complex medium

Having shown that reciprocity holds in the simulations there is one possible effect that can cause the reciprocity to break. Namely when the in-homogeneous medium is placed directly against the element. Given that for reciprocity to hold there should not be any sources on the boundary. But in this case one of the sides of the boundary is a source itself, potentially creating a non linear transition. Therefore the following simulation was created.

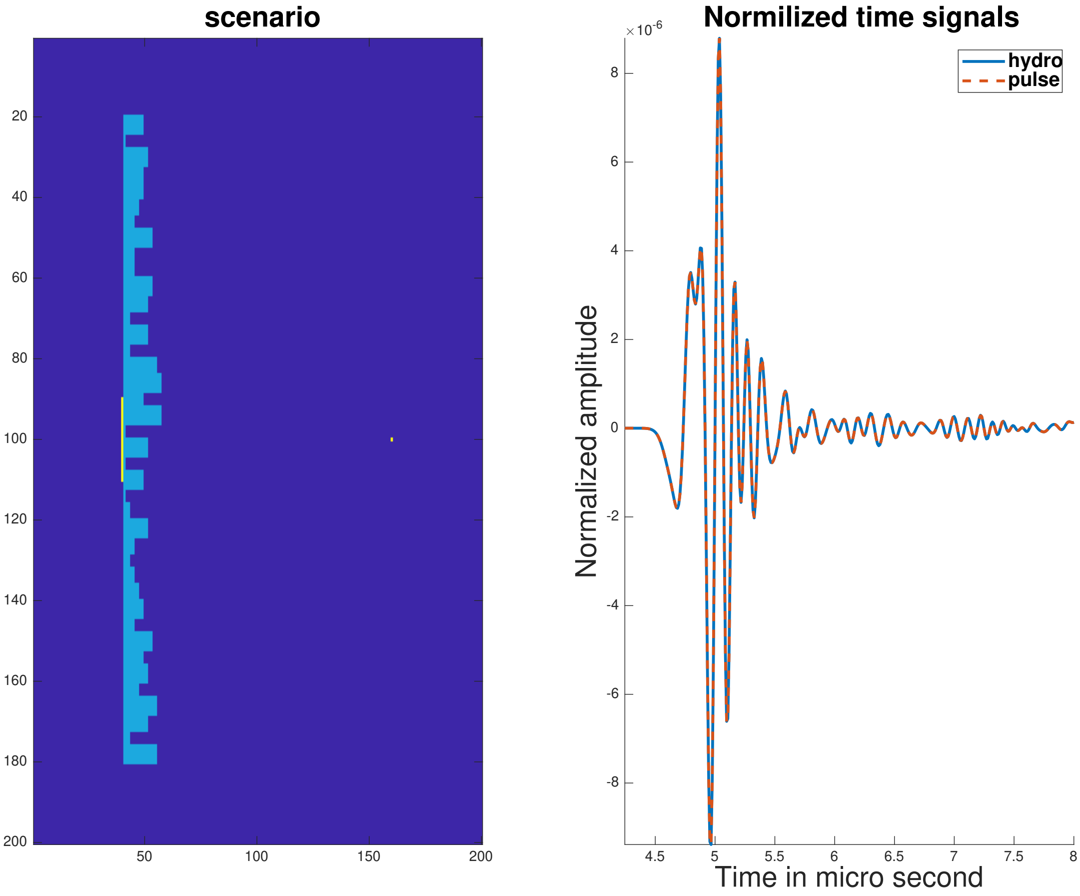

Figure 80: Reciprocity of 1 element and 1 point with a complex medium against the element

In this case a analogue to our aberration mask is placed directly against the element to examine this phenomena. The results is that reciprocity still holds in this simulation.
For completions sake this simulation was also preformed with loses even though loses don't create non-linearity's at low energy levels. The results of those are shown below:

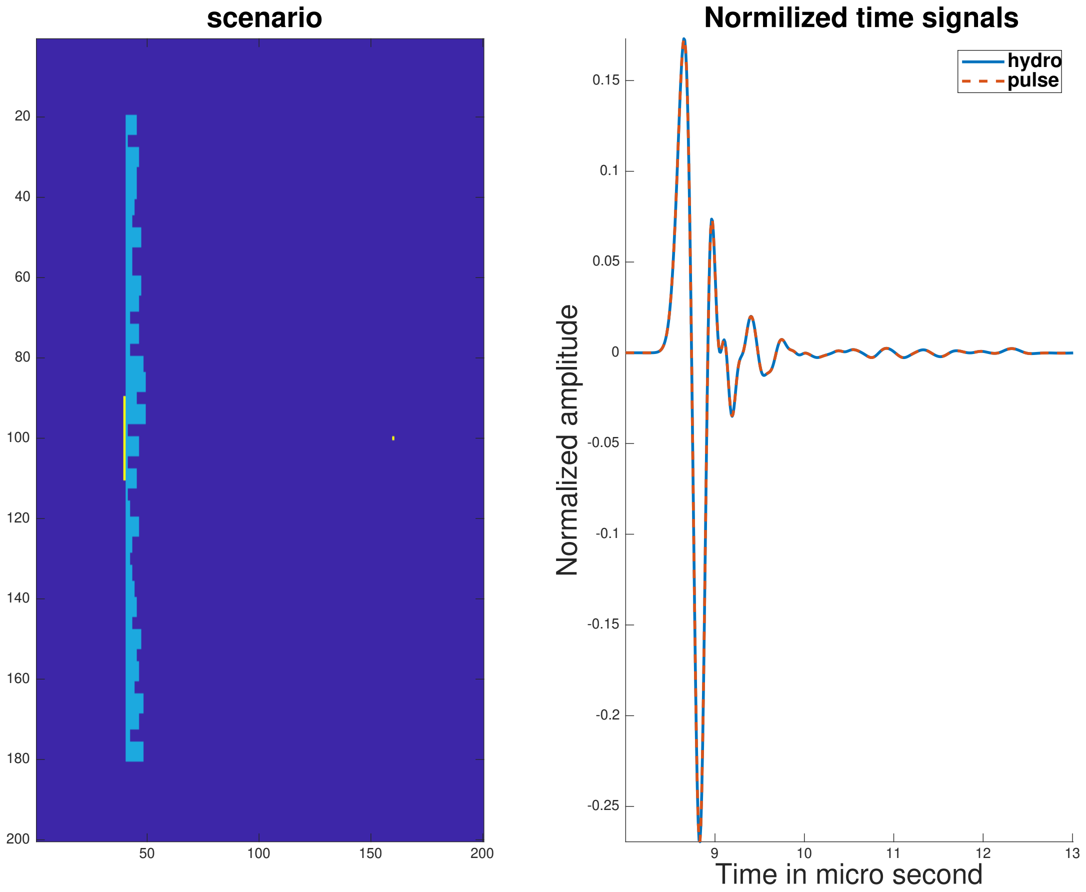

Figure 81: Reciprocity of 1 element and 1 point with a complex medium against the element and loses

As expected, reciprocity still holds. Even though we where unable to definitely state if reciprocity holds or not, after examining the theory and given the simulations results it is very likely that it indeed holds.